NONLINEAR MATERIALS FOR MID-INFRARED INTEGRATED PHOTONICS APPLICATIONS

A Dissertation

by

TIENING JIN

Submitted to the Office of Graduate and Professional Studies of
Texas A&M University
in partial fulfillment of the requirements for the degree of

DOCTOR OF PHILOSOPHY

Chair of Committee,	Pao-Tai Lin
Committee Members,	Jun Kameoka
	Jun Zou
	Svetlana A. Sukhishvili
Head of Department,	Miroslav M. Begovic

May 2019

Major Subject: Electrical Engineering

Copyright 2019 Tiening Jin

ABSTRACT

The emergence of silicon (Si) photonics over the past two decades has established silicon as a preferred substrate platform for photonic integration. While most Si-based photonic components have so far been realized in the near-infrared (near-IR) telecommunication bands, the mid-infrared (mid-IR, 2–20-μm wavelength) band presents a significant growth opportunity for integrated photonics. Mid-IR is a technologically important wave band that (a) encompasses multiple atmospheric windows (3 - 5 μm and 8 - 14 μm) essential for thermal imaging, infrared homing, and countermeasures and (b) covers the primary absorption bands of most chemical and biological molecules as well as the fingerprint region (7 - 20 μm), both of which are of prime interest to spectroscopic sensing. However, limited by narrow mid-IR transmission window, low optical nonlinear effect, and absence of electro-optical tunability, conventional Si-based platforms preclude various attempts in the longer wavelength range and active photonic functionalities. Materials of high mid-IR transparency and nonlinear optical properties, including aluminum nitride (AlN), lithium niobate (LN), and barium titanate (BTO), are proposed to extend conventional integrated photonic applications from visible-near-IR to mid-IR region. Integrated with AlN and BTO functional layers, three mid-IR waveguide sensors are designed, fabricated, and studied. Sharp fundamental modes are clearly observed within 2.5 - 3.8 μm. By scanning the spectrum within the characteristic absorption regime, the waveguide sensors are able to perform label-free monitoring of various organic solvents in real-time. In addition, three polarization modulators based on BTO and LN are introduced. Pockels effect of the integrated photonics in the mid-IR range is exploited for the first time. The measured highest effective electro-optical coefficient is as high as 278 pm/V, and a large modulation depth of 10 dB is achieved.

ACKNOWLEDGEMENTS

I would like to thank my committee chair and advisor, Dr. Pao-Tai Lin, for his superb guidance and support of my graduate study. He provided me with the utmost encouragement and diligence. I would also like to thank my other committee members, Dr. Svetlana A. Sukhishvili, Dr. Jun Kameoka, and Dr. Jun Zou, for their guidance and support throughout the course of this research. Thanks also go to my friends and colleagues and the department faculty and staff for making my time at Texas A&M University a great experience. Finally, thanks to my mother and father for their encouragement.

CONTRIBUTORS AND FUNDING SOURCES

Contributors

This work was supervised by a thesis committee consisting of Professor Pao-Tai Lin of electrical engineering and Professor Jun Zou of electrical engineering and Professor Jun Kameoka of electrical engineering and Professor Svetlana A. Sukhishvili of materials science & engineering. The device fabrication and characterization were performed at the AggieFab, Materials Characterization Facility (MCF) at Texas A&M University and the Center for Nanoscale Systems (CNS) at Harvard University. The barium titanite films and XRD data in chapter 3 were provided by Professor Haiyan Wang of Perdue University. The deposited amorphous silicon and aluminum nitride XPS data in chapter 3 were provided by Hao-Yu Greg Lin of CNS at Harvard University.

All other work conducted for the thesis (or) dissertation was completed by the student independently.

Funding Sources

Graduate study was supported the funding from Texas A&M University (TAMU), the Texas A&M Engineering Experiment Station (TEES), Crucialtec Co., Ltd, Texas A&M University Presidential X-Grant and NSF-ERC PATHSUP Program.

TABLE OF CONTENTS

	Page
ABSTRACT	ii
ACKNOWLEDGEMENTS	iii
CONTRIBUTORS AND FUNDING SOURCES	iv
TABLE OF CONTENTS	v
LIST OF FIGURES	vii
LIST OF TABLES	xi
CHAPTER I INTRODUCTION	1
1.1 Background	1
1.2 Motivation	4
1.3 Organization of Thesis	5
CHAPTER II THEORETICAL REVIEW	7
2.1 Planar Waveguide Evanescent Field	7
2.2 Electro-Optical Effect	11
2.2.1 Pockels Effect	11
2.2.2 Lithium Niobate and Barium Titanate Example	14
2.2.3 Polarization Modulation	23
CHAPTER III MID-INFRARED WAVEGUIDE SENSORS	25
3.1 Measurement System Set-up	25
3.2 Silicon on Barium Titanate Waveguide Sensor	26
3.2.1 Device Fabrication and Materials Characterization	27
3.2.2 Optical Property Simulation	31
3.2.3 Sensing Effect Characterization	35
3.3 Silicon on Aluminum Nitride Waveguide Sensor	40

3.3.1 Device Fabrication and Materials Characterization 40
3.3.2 Optical Property Simulation 45
3.3.3 Sensing Effect Characterization 46
3.4 Flexible Aluminum Nitride Waveguide Sensor 50
3.4.1 Device Fabrication and Materials Characterization 51
3.4.2 Optical Property Simulation 57
3.4.3 Sensing Effect Characterization 60

CHAPTER IV MID-INFRARED ELECTRO-OPTICAL MODULATORS 67

4.1 Measurement System Set-up 67
4.2 Titanium Dioxide on Lithium Niobate Polarization Modulator 68
4.2.1 Device Fabrication and Material Characterization 69
4.2.2 Optical Property Simulation 72
4.2.3 Electro-Optical Effect Characterization 74
4.3 Top-bonded Barium Titanate Polarization Modulator 76
4.3.1 Device Fabrication and Materials Characterization 77
4.3.2 Optical Property Simulation 80
4.3.3 Electro-Optical Effect Characterization 82
4.4 Silicon Nitride on Barium Titanate Polarization Modulator 86
4.4.1 Device Fabrication and Materials Characterization 86
4.4.2 Optical Property Simulation 88
4.4.3 Electro-Optical Effect Characterization 90

CHAPTER V CONCLUSIONS 95

REFERENCES 99

LIST OF FIGURES

Page

Figure 1.1 Characteristic absorption bands in mid-IR region for various molecules.............. 2

Figure 2.1 Plane wave of light at the interface of two dielectrics 8

Figure 2.2 The field amplitude of the evanescent wave decays exponentially further from the media interface, its direction of propagation is parallel to the interface as illustrated ... 10

Figure 2.3 Schematic of index ellipsoid. 12

Figure 2.4 The index ellipsoid rotates in the y-z plane 16

Figure 2.5 Schematic of the polarization change caused by phase retardation 23

Figure 3.1 Schematic of the sensing station. 25

Figure 3.2 The fabrication process of monolithic mid-IR microphotonics using a-Si ridge waveguides on the BTO thin film. 27

Figure 3.3 (a) The XRD θ-2θ scan of our epitaxially grown BTO thin film on LAO (001) substrate.. 28

Figure 3.4 The morphology and the composition of our mid-IR devices from SEM and EDX inspection. 30

Figure 3.5 (a) The device configuration and the refractive index profile applied in our FDTD modeling 32

Figure 3.6 (a) The calculated optical field when the thickness of the a-Si layer, Ta-Si, increases from 0.25 μ mto 1.5 μ m, but the BTO layer remains at 0.5 μ m......................... 33

Figure 3.7 The waveguide mode images capture at λ = 2.6 μ mto λ = 3.4 μm... 36

Figure 3.8 (a) Mode images and (b) Relative optical powers measured from the waveguides with different lengths. 37

Figure 3.9 The waveguide mode images were captured from λ = 2.5 μm to 3.2 μm with or without chemicals covering the waveguide 38

Figure 3.10 Real-time detection of (a) heptane and (b) methanol using mid-IR waveguide sensors at λ = 3.1 μm and 2.9 μm, respectively 39

Figure 3.11 The fabrication process of a monolithic mid-IR photonic chip that consisted of a Si ridge waveguide and AlN under-cladding 41

Figure 3.12 (a) XPS depth analysis of the AlN thin film........ 42

Figure 3.13 (a) The top and (b) the cross-sectional SEM images of the Si-on-AlN waveguide 44

Figure 3.14 (a) The TE and TM waveguide modes calculated at λ = 2.5, 2.75, and 3.0 μm.... 45

Figure 3.15 (a) The waveguide mode images captured at λ = 2.5, 2.75, and 3.0 μm........ 47

Figure 3.16 The waveguide mode images captured between λ = 2.5 and 3.0 μm........ 48

Figure 3.17 Real-time detection of (a) heptane and (b) methanol using the mid-IR waveguide sensor........ 49

Figure 3.18 The fabrication process of the device........ 51

Figure 3.19 (a) Vis-NIR and (b) ATR-FTIR spectra of the AlN films prepared by DC sputtering at different Ar : N_2 ratios. 52

Figure 3.20 The **n** and **k** plots of the AlN thin film from IR-VASE measurement........ 53

Figure 3.21 (a) The fabricated AlN-on-borosilicate flexible waveguides. The waveguide array is indicated by the yellow arrows 54

Figure 3.22 (a) The fabricated AlN-on-borosilicate flexible photonics 56

Figure 3.23 (a) The FEM calculated waveguide modes of a 1 μm tall AlN-on-borosilicate waveguide at various bending radii R........ 57

Figure 3.24 (a) The calculated mode images of an AlN-on-borosilicate waveguide when it is exposed to an analyte containing a mid-IR absorptive chemical........ 59

Figure 3.25 (a) The waveguide mode images captured at λ = 2.5, 2.6, and 2.7 μm........ 61

Figure 3.26 The waveguide mode images captured between λ = 2.50 and 2.65 μm when it was covered by different chemicals, including ethanol, methanol, and water 62

Figure 3.27 The (a) images and (b) mode intensities of the AlN waveguide modes when the waveguide exposed to ethanol/water mixtures at different concentrations 64

Figure 3.28 The (a) mode images and (b) transient response for real-time chemical detection using the AlN-on-borosilicate waveguide. 65

Figure 4.1 The experimental set-up to test the electro-optical modulation of the ToL

waveguide 67

Figure 4.2 Schematic of the TiO_2-on-LN waveguide fabrication process. 69

Figure 4.3 The transmission spectrum of deposited TiO_2 from ATR-FTIR measurement, showing a broad transmittance up to λ = 8 μ m. 70

Figure 4.4 The cross-sectional view of the ToL waveguide from (a) SEM and EDX from (b) Ti K and (c) Nb L emission lines, indicating the TiO_2 ridge, Ti electrodes, and the LN substrate, respectively. 71

Figure 4.5 (a) The calculated optical field when the thickness of the TiO_2 layer decreases from 1.0 μ m to 0.6 μ m. 72

Figure 4.6 (a) The optical waveguide mode captured by a MIR camera when the polarizer rotated at different angle ɵ. 75

Figure 4.7 (a) The transient mode intensity when pulses of the electrical field were applied to the electrodes using a power supply at various voltage **V** 76

Figure 4.8 (a) Schematic structure of the TiO_2-on-SiO_2 waveguide bonded with BTO crystal. 77

Figure 4.9 (a) The top view of the fabricated device captured by an optical microscope 79

Figure 4.10 (a) The optical fields of the TiO2-on-SiO2 waveguides calculated at λ = 2.5, 2.6, and 2.7 μ m. 80

Figure 4.11 The waveguide mode images captured from λ = 2.5 to λ = 3.7 μm, where the fundamental mode is clearly observed. 82

Figure 4.12 (a) The optical waveguide modes captured by a mid-IR camera when various drive voltages were applied. (b) The mode intensity when several pulses of the electric field were applied to the electrodes using a power supply at voltage V. 84

Figure 4.13 (a) The 1D intensity distribution of the waveguide mode recorded at various voltage. (b) The plot of the mode intensity vs the applied voltage. 85

Figure 4.14 Schematic of the SiN-on-BTO waveguide fabrication process. 87

Figure 4.15 Top view of the fabricated device captured by (a) microscope and (b) SEM. 88

Figure 4.16 (a) The device configuration and the refractive index profile applied in the FEM modeling 89

Figure 4.17 (a) The waveguide mode images captured at λ = 2.5 μm to λ = 2.7 μm, where fundamental mode is clearly observed 91

Figure 4.18 (a) The optical waveguide mode captured by a mid-IR camera when drive voltage was applied. The wavelength was set at $\lambda = 2.6\ \mu m$ 92

Figure 4.19 Real-time electro-optic modulation of SiN-on-BTO device 93

LIST OF TABLES

Page

Table 4.1 The TiO_2-on-LN waveguide confinement factors, Γ_{LN}, Γ_{TiO2}, and Γ_{Air}, at different thickness T_{TiO2}. Γ_{LN} increased from 46.0 to 80.0 as T_{TiO2} decreased from 1.0 to 0.6 μ mindicating an improvement of electro-optical modulation efficient. 74

CHAPTER I

INTRODUCTION

1.1 Background

The mid-infrared (IR) wavelength range (2.5 - 25 μm) is often referred to as the "finger-print region" since most molecules have uniquely characteristic absorption spectra within this wavelength range. Because of this, the mid-IR region is of great utility for various areas, including chemical bond spectroscopy, trivial gas detection, medical diagnostics, environmental monitoring, biochemical molecule sensing, and broadband optical communication. [1-8] For the optical network, extending the present operational spectrum from the near-IR (1550 nm) into the mid-IR region will provide additional optical channels thus improving the data transmission rates. [9] For sensor applications, mid-IR spectrum overlaps with the characteristic absorption bands (as shown in Figure 1.1) and the finger-print region of numerous chemical functional groups so it enables label-free biochemical detection of high accuracy. For human health and environment monitoring, moderate mid-IR light source does no harm on the human body or environment, enabling it an ideal method to provide real-time and sustainable monitoring without pollution or injury. Additionally, the mid-IR wavelength region is also particularly suited for thermal imaging and free-space communications, especially within the atmospheric windows of 3 - 5 μm and 8 - 11 μm. [10] Despite the wealth of applications, the on-chip mid-IR photonics platform needed to access them is relatively undeveloped. While the last 20 years have seen the development of high-power, room temperature-operational mid-IR light sources and bulky mid-IR detectors, little work has been done in developing the passive and active photonics elements such as waveguides, resonators, beam splitters, electro-optic modulators, etc.[10] for the mid-IR applications. So far, the most

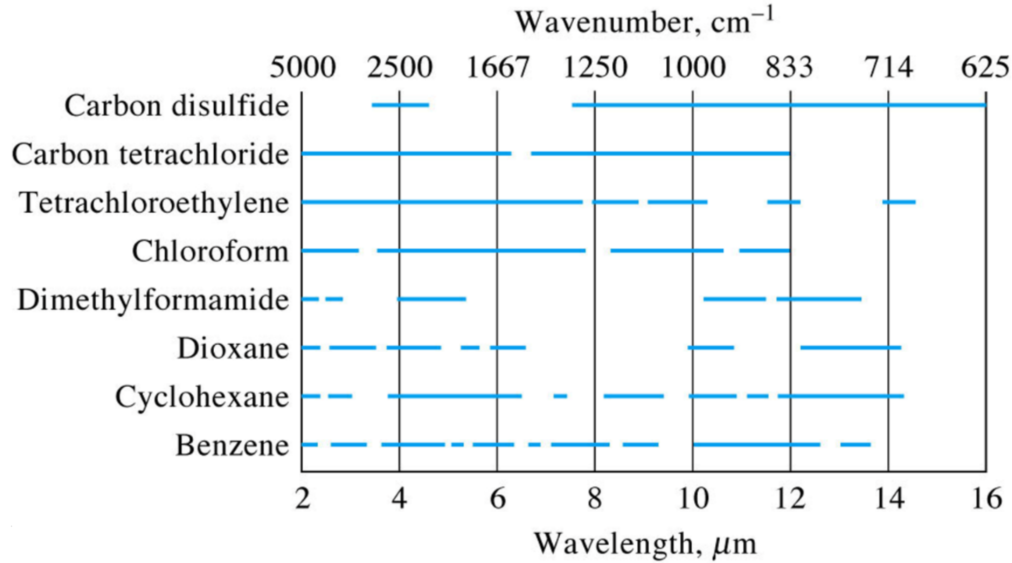

Figure 1.1 Characteristic absorption bands in mid-IR region for various molecules.

---

straightforward and conventional approach to fulfill integrated mid-IR photonics is to use silicon-on-insulator waveguide structures. such as silicon-on-insulator, pedestal silicon configuration, silicon-rich silicon nitride, etc. [11-16] Applications have also been demonstrated in various devices including chip-scale infrared spectrometers, mid-IR directional couplers, and label-free glucose sensors. [17-19] Nevertheless, due to centrosymmetric crystal structure, silicon has low optical nonlinearity (χ^3) and is absent of electro-optical tunability (Pockets and Kerr effects) that limits its applications for active photonic components such as nonlinear frequency conversion and high-speed optical signal modulation. [20,21] In addition, the conventional Si photonics platform utilizes silicon dioxide (SiO_2) or sapphire (Al_2O_3) as the optical waveguide under-cladding, while both of them are mid-IR opaque. Thus, even silicon has broad infrared transparency up to λ = 8 μm, the strong absorption caused by silicon dioxide or sapphire after λ = 4 μm excludes Si photonics from applications like label-free sensing utilizing mid-IR finger-print absorption. [22]

To overcome Si limitation in mid-IR photonics and performing active photonic functionalities, nonlinear optical materials were proposed to integrate with conventional Si photonics to extend

their applications to the mid-IR region. Nonlinear optical materials are a class of crystal of nonlinear optical properties. Due to their non-centrosymmetric crystal structure, they are able to exhibit strong non-linear optical properties, which is essential to active photonic components such as wave phase shifter, amplitude modulator, frequency mixer, and parametric oscillator. [23] One of the most widely-used non-linear photonic crystal is lithium niobate (LN). LN is transparent up to $\lambda > 5$ μm with a moderate refractive index of 2.18 at 2.5μm, which grants it versatile roles either as a waveguide cladding or a waveguide core in the mid-IR regime.[24, 25] In addition, LN has a high electro-optical coefficient and a large second-order optical nonlinearity (χ^2) so it enables efficient nonlinear light generation and electro-optical light modulation. Previous studies have shown an LN switch in near-infrared with a modulation speed exceeding 100 GHz and a low $V_\pi \cdot L$ of ~10 Vcm, where $V_\pi \cdot L$ is the product of the voltage and the device length to create a π phase difference.[26, 27] In addition, both phase and intensity LN modulators can achieve a high extinction ratio > 13 dB, which is significantly better than present Si-based photonic devices. New platforms combining crystalline silicon and LN thin film have recently been created and applied for micro-disk resonators and waveguide modulators.[28-30] Therefore, LN is an ideal platform for tunable mid-IR photonic circuits. Comparing to LN, another ferroelectric crystal barium titanate (BTO) has a much larger electro-optical coefficient as 150 pm/V, [31, 32] which is 5 times larger than LN. BTO also has a wider mid-IR transparent window up to 8 μm.[33,34] Moreover, preparation of LN thin films involve sophisticated fabrication processes including oxygen implantation, crystal ion-slicing, and wafer bonding that prevent them from practical usage in microphotonic devices. On the contrary, BTO can be epitaxially grown on a Si wafer through various thin film deposition technologies, such as PLD, molecular beam epitaxy (MBE), and chemical vapor deposition (CVD), which enables the integration between functional oxides and Si photonics. [35-39] BTO also has high

chemical stability and mechanical hardness making it capable of working in harsh environments. Another proposed material is aluminum nitride (AlN), which also has a wide transmission spectrum that covers ultraviolet (UV), visible (VIS), NIR and mid-IR up to $\lambda = 10$ μm. [40, 41] The extensive mid-IR window of AlN is attributed to its low optical phonon absorption energies, which are 113.6 meV for longitudinal mode and 82.7 meV for the transverse mode. AlN also has large optical nonlinearity so suitable for nonlinear light generation by using sum- and difference-frequency generation or optical parametric oscillator.[42,43] In addition, AlN is mechanically strong, thermally stable, and chemical resistant thus enabling it for sensor application under harsh environmental condition.[44,45] The integration between AlN thin film with other CMOS materials, such as Si, SiO_2, or sapphire, can be achieved through metal organic chemical vapor deposition (MOCVD), molecular beam epitaxy (MBE), or sputtering.[46-49]

1.2 Motivation

All non-linear materials mentioned above, including LN, BTO, and AlN, all have intrinsic transparent windows in the mid-IR region, and the ability to exhibit electro-optical modulation. Therefore, they are optimal platforms for fabricating mid-IR photonic passive and active components. Integrated with conventional Si-based materials, these platforms reveal numerous advantages from the aspects of *i.* Integration of functional materials, *ii.* Compatibility with CMOS fabrication process, and *iii.* Multifunctionality by repositioning the waveguide modes within different layers. First, (*i*) The film deposition technique is sophisticated enough to grow LN, BTO, and AlN films of high quality. The deposited films are normally of a moderate refractive index and high transparency in the mid-IR region, which makes them either ideal waveguide guiding material or cladding materials. For example, they are able to act as functional cladding layer

integrated with Si, and show efficient guiding effect integrated with insulator or silicon nitride. Second, *(ii)* The whole material deposition and device fabrication are CMOS compatible, which enables the possibility of large-scale commercial use. Third, *(iii)* The position of waveguide modes can be adjusted for both high-speed electro-optical modulation and biochemical sensing, by engineering the device structure. The monolithic mid-IR platforms are capable of serving various applications including reconfigurable photonic circuits and label-free chemical detections. The following thesis explores the possibility of LN, BTO, and AlN for mid-IR applications, and demonstrates some monolithically integrated components.

1.3 Organization of Thesis

This thesis is organized into five chapters, and on the development of six different integrated photonic devices. Three of them are mid-IR waveguide sensors, the others are mid-IR wave polarization modulators.

Chapter I is the introduction to the backgrounds and motivation to the research presented in this work.

Chapter II gives the basic theory behind the fabricated waveguide devices for the purpose of preparing the reader to chapters afterward. First, planar wave evanescent field distribution and skin depth calculation are introduced for mid-IR evanescent sensing devices. Then Pockels effect of LN and BTO are discussed for mid-IR polarization modulators, which includes how to derive their impermeability, calculate refractive index change under the external applied electric field, and the mechanism of polarization modulation.

Chapter III presents three mid-IR waveguides sensors including Si-on-BTO sensor, Si-on-AlN sensor, and flexible AlN sensor. This chapter detailly introduces the materials deposition, materials characterization, device structure design and simulation, their optical property and sensing effects.

Chapter IV presents three mid-IR polarization modulators including TiO_2-on-LN modulator, top-bonded BTO modulator, and SiN-on-BTO modulator. This chapter detailly introduces the device structure design and simulation, their optical property and electro-optical modulation effects.

Chapter V is the concluding remarks to the research presented in this thesis.

CHAPTER II

THEORETICAL REVIEW

This chapter summarizes the basic theory of planar evanescent field distribution in a waveguide structure and Pockels effect of non-linear materials. For planar waveguide structures, light wave propagating within two different low-loss media is discussed to derive the equation associated with evanescent waves and the expression of skin depth. Such evanescent wave is critical for waveguide sensing applications since it's related to the sensitivity of the waveguide sensor. Pockels effect is introduced for the electro-optical modulation applications. Two kinds of ferroelectric crystal LN and BTO are considered to discuss the electro-optical effect.

2.1 Planar Waveguide Evanescent Field

A waveguide is a structure that guides electromagnetic waves with minimal loss of energy by light confinement within one or two dimensions. Normally a waveguide consists of two parts: a wave-guiding core and a cladding. The wave-guiding core is of high refractive index, and the cladding is of low refractive index. The mechanism for the optical waveguide is total internal reflection. The simplest way to understand the concept of optical propagation through the waveguide is by considering the case of the planar waveguide structure. The planar waveguide is the simplest waveguide structure, which can be extended to analyze other more complex waveguide structures such as the rib waveguide or the slot waveguide.

As shown in Figure 2.1, when light from one medium propagates through another medium with a different refractive index, it will either be reflected or transmitted, depending on the refractive indexes of both media and the incident angle of the light. The evanescent wave phenomenon can be derived from the plane wave at the interface of two dielectrics, assuming the refractive indices

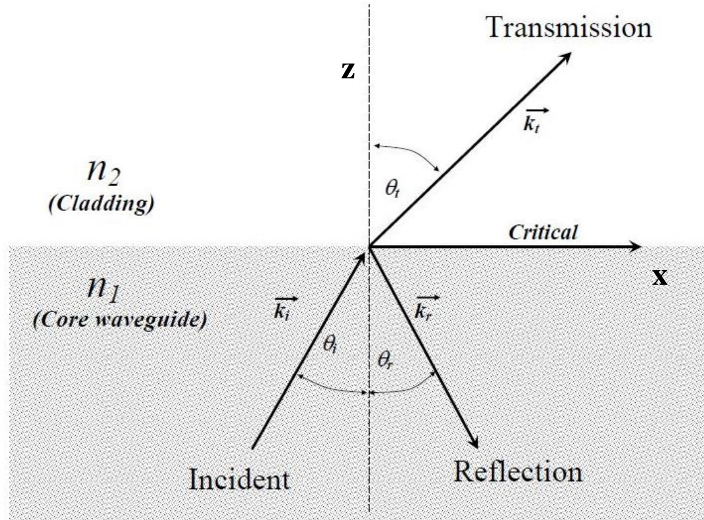

Figure 2.1 Plane wave of light at the interface of two dielectrics.

of two mediums are n_1 and n_2 respectively. For the waveguide case, n_1 should be larger than n_2 to meet the total reflection requirement. The relationship between the incident light angle and the transmission light angle can be derived by Snell's law as:

$$n_1 sin\theta_i = n_2 sin\theta_t \qquad (2.1)$$

Where θ_i and θ_t are the incident angle and the transmission angle of the light. When the incident angle becomes larger, the transmission angle will also be increased. The transmission angle θ_t could be reached at π/2 if the incident angle went large enough. In that case, the incident angle is called critical angle (θ_c), and that situation is called critical condition for the transmission light. Thus, the critical angle can be expressed as

$$\theta_i = \theta_c = \sin^{-1}\frac{n_2}{n_1} \qquad (2.2)$$

If the incident angle θ_i goes larger than critical angle θ_c, the $\sin^2\theta_t$ should be larger than 1. In that case, θ_t will have an imaginary part as

$$\theta_t = \frac{\pi}{2} + i\alpha \qquad (2.3)$$

Now we have

$$sin\theta = \frac{e^{i\theta} - e^{-i\theta}}{2i} \qquad (2.4)$$

$$sin\theta_t = \frac{e^{\frac{\pi}{2}i}e^{-\alpha} - e^{-\frac{\pi}{2}i}e^{\alpha}}{2i} = \frac{e^{-\alpha} + e^{\alpha}}{2} \qquad (2.5)$$

$$cos\theta_t = \frac{e^{\frac{\pi}{2}i}e^{-\alpha} + e^{-\frac{\pi}{2}i}e^{\alpha}}{2} = \frac{ie^{-\alpha} - ie^{\alpha}}{2} \qquad (2.6)$$

Let's take the incident plane to be x-z plane and the interface to be the x-y plane so that the normal to the plane is along the z-direction. The transmitted wave can be written as

$$\vec{E}_t = \vec{E}_{t0}e^{i(\vec{k}_t \cdot \vec{r}_t - \omega t)} \qquad (2.7)$$

where $\mathbf{k_t}$ is the wave vector of the transmitted light, and $\mathbf{r_t}$ is the position vector at which the wave is observed. The space part of the wave can be expressed as

$$i\vec{k}_t \cdot \vec{r}_t = i(k_{tx} + k_{tx}) = i(k_t x sin\theta_t + k_t z sin\theta_t) \qquad (2.8)$$

Rewriting in terms of angle of incidence θ_i

$$i\vec{k}_t \cdot \vec{r}_t = i\left(k_t x \frac{n_1}{n_2} sin\theta_i + k_t z\sqrt{1 - \frac{n_1^2}{n_2^2}\sin^2\theta_i}\right) \qquad (2.9)$$

For angles greater than the critical angle the quantity within the square root is negative and we rewrite it as

$$i\vec{k}_t \cdot \vec{r}_t = i\left(k_t \frac{n_1}{n_2} x sin\theta_i + ik_t z\sqrt{\frac{n_1^2}{n_2^2}\sin^2\theta_i - 1}\right) = i\beta x - \alpha z \qquad (2.10)$$

where the wave vector β is defined as

$$\beta = k_t \frac{n_1}{n_2} x sin\theta_i \qquad (2.11)$$

The attenuation factor α is defined as λ

$$\alpha = k_t\sqrt{\frac{n_1^2}{n_2^2}\sin^2\theta_i - 1} = \frac{\omega n_2}{c}\sqrt{\frac{\sin^2\theta_i}{n^2} - 1} = \frac{\omega}{c}\sqrt{n_1^2\sin^2\theta_i - n_2^2} \qquad (2.12)$$

This solution describes a non-propagating electric field which decays exponentially in medium 2. The wave in the transmitted medium can be expressed as

$$\vec{E}_t = \vec{E}_{t0}e^{i(\beta x - \omega t)}e^{-\alpha z} \qquad (2.13)$$

which shows that the wave in the second medium propagates along the interface. It penetrates into the medium but its amplitude attenuates exponentially. This is known as a "evanescent wave". The penetration depth of the evanescent field d_p, is defined as the distance required for the electric field amplitude to fall to e^{-1} or 37% of its value at the interface and is expressed as

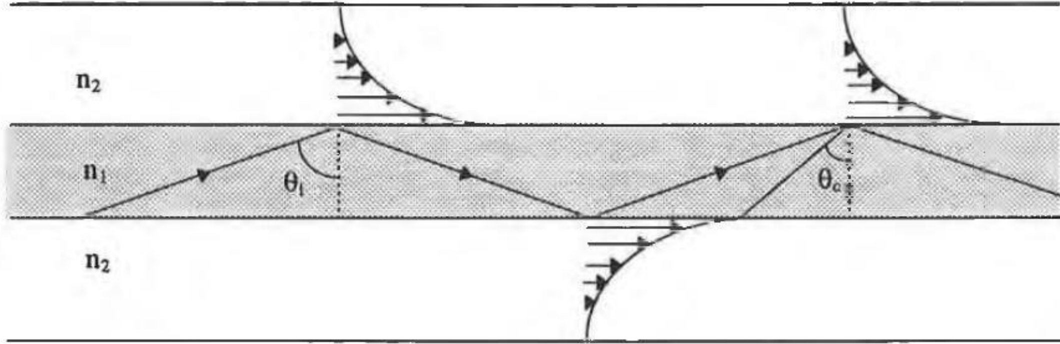

Figure 2.2. The field amplitude of the evanescent wave decays exponentially further from the media interface, its direction of propagation is parallel to the interface as illustrated.

$$d_p = \frac{1}{\alpha} = \frac{\lambda_0}{2\pi\sqrt{n_1^2\sin^2\theta_i - n_2^2}} \qquad (2.14)$$

In evanescent wave sensing, it is very important to optimize penetration depth to achieve high sensitivity. Normally the factors that influence the penetration depth are the wavelength of the incident light, the refractive index ratio and the incident angle θ_i. For the evanescent sensing, perturbations of the evanescent fields (attenuated total reflection) can result in a reduction of the

reflected optical power. If a lossless dielectric overlaps the exponentially decaying evanescent field, it reduces the intensity of the reflected wave so the reflection condition is unsatisfied.

2.2 Electro-Optical Modulation

The basic idea behind electro-optic devices is to alter the optical properties of a material with an applied voltage in a controlled way. The changes in the optical properties, particularly the permittivity tensor, translate into a modification of some parameter of a light wave carrier, such as phase, amplitude, frequency, polarization, or position, as it propagates through the device.

2.2.1 Pockels Effect

For anisotropic crystals, the propagation of optical radiation in the media can be described completely in terms of the impermeability tensor η_{ij}, defined by

$$\eta = \epsilon_0 \epsilon^{-1} \qquad (2.15)$$

where $\epsilon_0 \epsilon^{-1}$ is relative permittivity of the medium. The index ellipsoid (shown in Figure 2.3) representation is a good method for finding the two directions of polarization and the corresponding refractive indices. The general form of the index ellipsoid is given by

$$\sum_{i,j=1,2,3} \eta_{ij} x_i x_j = 1 \qquad (2.16)$$

The ellipsoid is expressed in Cartesian principal coordinates as

$$\frac{x^2}{n_x^2} + \frac{y^2}{n_y^2} + \frac{z^2}{n_z^2} = 1 \qquad (2.17)\ \eta_{ij} = (\varepsilon^{-1})_{ij} \varepsilon_0$$

Where $\frac{1}{n_x^2}$, $\frac{1}{n_y^2}$, and $\frac{1}{n_z^2}$ are the principal values of the impermeability tensor η_{ij}. That equation is the general index ellipsoid for an optically biaxial crystal. If $n_x = n_y$, the surface becomes an ellipsoid

of revolution, representing an uniaxial crystal. If $n_x = n_y = n_z$, the surface becomes a sphere indicating the medium is optically isotropic.

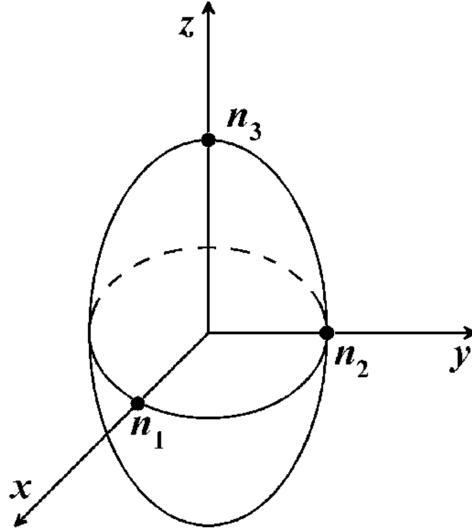

Figure 2.3 Schematic of index ellipsoid.

At an atomic level an electric field applied to certain crystals causes a redistribution of bond charges and possibly a slight deformation of the crystal lattice. In general, these alterations are not isotropic, which means the tensor components are different with direction in the crystal. Therefore, the inverse impermeability tensor changes accordingly. Each $\eta_{ij}(E)$ is a function of three variables **E** = (E_1, E_2, E_3), which can be expanded by Taylor's series about **E=0**:

$$\eta_{ij}(E) = \eta_{ij}(0) + \sum_k \gamma_{ijk} E_k + \sum_{k,l} s_{ijkl} E_k E_l + \cdots \quad (2.18)$$

Where the γ_{ijk} is linear electro-optic coefficient (Pockels effect), and s_{ijkl} is quadratic electro-optic coefficients (Kerr effect). Crystals lacking a center of symmetry are non-centrosymmetric and its Pockels effect is dominate. The changes in the impermeability tensor elements are linear in the applied electric field. The center symmetric crystal, on the other hand, exhibits strong Kerr effect. Thus, the impermeability tensor changed by the applied field is only determined by:

$$\eta_{ij}(E) = \eta_{ij}(0) + \sum_k \gamma_{ijk} E_k \quad (2.19)$$

$$\Delta\eta_{ij}(E) = \sum_k \gamma_{ijk} E_k \quad (2.20)$$

The changed tensor formation can be expressed as

$$\begin{pmatrix} \Delta\eta_{11} \\ \Delta\eta_{12} \\ \Delta\eta_{13} \\ \Delta\eta_{21} \\ \Delta\eta_{22} \\ \Delta\eta_{23} \\ \Delta\eta_{31} \\ \Delta\eta_{32} \\ \Delta\eta_{33} \end{pmatrix} = \begin{pmatrix} \gamma_{111} & \gamma_{112} & \gamma_{113} \\ \gamma_{121} & \gamma_{122} & \gamma_{123} \\ \gamma_{131} & \gamma_{132} & \gamma_{133} \\ \gamma_{211} & \gamma_{212} & \gamma_{213} \\ \gamma_{221} & \gamma_{222} & \gamma_{223} \\ \gamma_{231} & \gamma_{232} & \gamma_{233} \\ \gamma_{311} & \gamma_{312} & \gamma_{313} \\ \gamma_{321} & \gamma_{322} & \gamma_{323} \\ \gamma_{331} & \gamma_{332} & \gamma_{333} \end{pmatrix} \begin{pmatrix} E_1 \\ E_2 \\ E_3 \end{pmatrix} \quad (2.21)$$

E_1, E_2, and E_3 are the components of the applied electric field in principal coordinates. Because of the symmetry properties of the impermeability tensor $\eta_{ij}=\eta_{ji}$, the Pockels coefficient has to fulfill the condition $\gamma_{ijk}= \gamma_{jik}$. Thus, the Pockels tensor γ_{ijk} can by simplified at most 6×3 independent elements. The number of independent elements can be further decreased through symmetry properties of the crystal. It is convenient to use the following contracted notation:

$$\gamma_{hk} = \gamma_{ijk}$$

$$h = \begin{cases} 1 & for\ \ ij = 11 \\ 2 & for\ \ ij = 22 \\ 3 & for\ \ ij = 33 \\ 4 & for\ \ ij = ij = 23 \\ 5 & for\ \ ij = ij = 13 \\ 6 & for\ \ ij = ij = 12 \end{cases}$$

With new notation, the matrix can be simplified as

$$\begin{pmatrix} \Delta\eta_{1} \\ \Delta\eta_{2} \\ \Delta\eta_{3} \\ \Delta\eta_{4} \\ \Delta\eta_{5} \\ \Delta\eta_{6} \end{pmatrix} = \begin{pmatrix} \gamma_{11} & \gamma_{12} & \gamma_{13} \\ \gamma_{21} & \gamma_{22} & \gamma_{23} \\ \gamma_{31} & \gamma_{32} & \gamma_{33} \\ \gamma_{41} & \gamma_{42} & \gamma_{43} \\ \gamma_{51} & \gamma_{52} & \gamma_{53} \\ \gamma_{61} & \gamma_{62} & \gamma_{63} \end{pmatrix} \begin{pmatrix} E_1 \\ E_2 \\ E_3 \end{pmatrix} \quad (2.23)$$

2.2.2 Lithium Niobate and Barium Titanate Example

For LN, the crystal structure is negative uniaxial. The electro-optic tensor of tetragonal lithium niobate is:

$$\begin{pmatrix} 0 & -\gamma_{22} & \gamma_{13} \\ 0 & \gamma_{22} & \gamma_{13} \\ 0 & 0 & \gamma_{33} \\ 0 & \gamma_{51} & 0 \\ \gamma_{51} & 0 & 0 \\ -\gamma_{22} & 0 & 0 \end{pmatrix} \quad (2.24)$$

Then the change in the optical impermeability is derived as:

$$\begin{pmatrix} \Delta\eta_1 \\ \Delta\eta_2 \\ \Delta\eta_3 \\ \Delta\eta_4 \\ \Delta\eta_5 \\ \Delta\eta_6 \end{pmatrix} = \begin{pmatrix} 0 & -\gamma_{22} & \gamma_{13} \\ 0 & \gamma_{22} & \gamma_{23} \\ 0 & 0 & \gamma_{33} \\ 0 & \gamma_{51} & 0 \\ \gamma_{51} & 0 & 0 \\ -\gamma_{22} & 0 & 0 \end{pmatrix} \begin{pmatrix} E_1 \\ E_2 \\ E_3 \end{pmatrix} \quad (2.25)$$

$$\Delta\eta_{ij}(E) = \begin{pmatrix} \gamma_{13}E_3 - \gamma_{22}E_2 & -\gamma_{22}E_1 & \gamma_{51}E_1 \\ -\gamma_{22}E_1 & \gamma_{22}E_2 + \gamma_{13}E_3 & \gamma_{51}E_2 \\ \gamma_{51}E_1 & \gamma_{51}E_2 & \gamma_{33}E_3 \end{pmatrix} \quad (2.26)$$

Thus, the impermeability tensor modulated by the applied electric field can be expressed as

$$\eta_{ij}(E) = \eta_{ij}(0) + \sum_k \gamma_{ijk}E_k = \begin{pmatrix} \frac{1}{n_x^2} & 0 & 0 \\ 0 & \frac{1}{n_y^2} & 0 \\ 0 & 0 & \frac{1}{n_z^2} \end{pmatrix} + \begin{pmatrix} \gamma_{13}E_3 - \gamma_{22}E_2 & -\gamma_{22}E_1 & \gamma_{51}E_1 \\ -\gamma_{22}E_1 & \gamma_{22}E_2 + \gamma_{13}E_3 & \gamma_{51}E_2 \\ \gamma_{51}E_1 & \gamma_{51}E_2 & \gamma_{33}E_3 \end{pmatrix}$$

(2.27)

We substitute E_1, E_2, and E_3 as E_x, E_y, and E_z, and the lithium niobate index ellipsoid can be derived from

$$\sum_{i,j=1,2,3} \eta_{ij}x_i x_j = 1$$

as

$$\left(\frac{1}{n_o^2} + \gamma_{13}E_z - \gamma_{22}E_y\right)x^2 + \left(\frac{1}{n_o^2} + \gamma_{22}E_y + \gamma_{13}E_z\right)y^2 + \left(\frac{1}{n_e^2} + \gamma_{33}E_z\right)z^2 - 2\gamma_{22}E_x xy +$$

$$2\gamma_{51}E_x xz + 2\gamma_{51}E_y yz = 1 \qquad (2.28)$$

Where $n_x = n_y = n_o$, and $n_z = n_e$ for lithium niobate. When the external electric field is along z ($E=E_z$, $E_x= E_y =0$), the formula can be derived as:

$$\left(\frac{1}{n_o^2} + \gamma_{13}E_z\right)x^2 + \left(\frac{1}{n_o^2} + \gamma_{13}E_z\right)y^2 + \left(\frac{1}{n_e^2} + \gamma_{33}E_z\right)z^2 = 1 \qquad (2.29)$$

Since no mixed terms appear in the equation, the principal of the axes of new index ellipsoid remains unchanged. We have

$$\frac{1}{n_{x'}^2} = \frac{1}{n_o^2} + \gamma_{13}E_z \qquad (2.30)$$

$$\frac{1}{n_{y'}^2} = \frac{1}{n_o^2} + \gamma_{13}E_z \qquad (2.31)$$

$$\frac{1}{n_{z'}^2} = \frac{1}{n_e^2} + \gamma_{33}E_z \qquad (2.32)$$

Gives

$$n_{x'}^2 = n_{y'}^2 = n_o^2\left(\frac{1}{1+n_o^2\gamma_{13}E_z}\right) \qquad (2.33)$$

$$n_{z'}^2 = n_e^2\left(\frac{1}{1+n_e^2\gamma_{33}E_z}\right) \qquad (2.34)$$

Thus, the distorted index can be expressed as:

$$n_{x'} = n_o(1 + n_o^2\gamma_{13}E_z)^{-\frac{1}{2}} \qquad (2.35)$$

$$n_{y'} = n_o(1 + n_o^2\gamma_{13}E_z)^{-\frac{1}{2}} \qquad (2.36)$$

$$n_{z'} = n_e(1 + n_e^2\gamma_{33}E_z)^{-\frac{1}{2}} \qquad (2.37)$$

Using the approximation $(1 + \Delta)^{-1/2} \approx 1 - \frac{1}{2}\Delta$, when $|\Delta|$ is a small value.

$$n_{x'} = n_o(1 - \frac{1}{2}n_o^2\gamma_{13}E_z) \qquad (2.38)$$

$$n_{y'} = n_o(1 - \frac{1}{2}n_o^2\gamma_{13}E_z) \qquad (2.39)$$

$$n_{z'} = n_e(1 - \frac{1}{2}n_e^2\gamma_{33}E_z) \qquad (2.40)$$

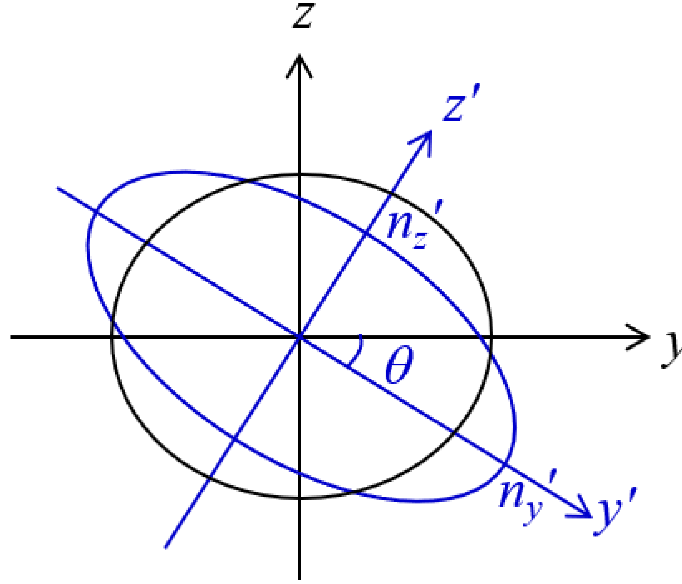

Figure 2.4 The index ellipsoid rotates in the y-z plane.

When the external electric field is along y (E_y=E, E_x = E_z =0), the formula can be derived as

$$\left(\frac{1}{n_o^2} - \gamma_{22}E_y\right)x^2 + \left(\frac{1}{n_o^2} + \gamma_{22}E_y\right)y^2 + \left(\frac{1}{n_e^2}\right)z^2 + 2\gamma_{51}E_y yz = 1 \qquad (2.41)$$

Clearly, because of the introduction of the cross term involving both variables, y and z, the original principal areas are no longer appropriate. The effect of the field has been to render the crystal biaxial and rotate the indicatrix in the y-z plane as shown in Figure 2.4. Let's assume that the indicatrix has been rotated so that its new principal axes y' and z' are at an angle θ to the original principal axes y-z. The x direction remains a principal axis with the field E_y applied, as no cross

term involving x has been introduced into the equation of the indicatrix. Suppose the index ellipsoid in the new coordinate system is

$$\frac{x'^2}{n_{x'}^2} + \frac{y'^2}{n_{y'}^2} + \frac{z'^2}{n_{z'}^2} = 1 \qquad (2.42)$$

Then the old principle axes can be expressed by new ones as:

$$x = x' \qquad (2.43)$$

$$y = y' \cos\theta - z' \sin\theta \qquad (2.44)$$

$$z = y' \sin\theta + z' \cos\theta \qquad (2.45)$$

For any given coordinate system

$$ax^2 + by^2 + cxy = Ax'^2 + Bx'^2 \qquad (2.46)$$

We have

$$\tan 2\theta = \frac{c}{a-b} \qquad (2.47)$$

$$A = \frac{(a+b) - \sqrt{(a-b)^2 + c^2}}{2} \qquad (2.48)$$

$$B = \frac{(a+b) + \sqrt{(a-b)^2 + c^2}}{2} \qquad (2.49)$$

Then we have

$$\tan 2\theta = \frac{2\gamma_{51}E_y}{\frac{1}{n_o^2} - \frac{1}{n_e^2} + \gamma_{22}E_y} = \frac{2\gamma_{51}E_y n_o^2 n_e^2}{n_e^2 - n_o^2 + n_o^2 n_e^2 \gamma_{22}E_y} \qquad (2.50)$$

$$\frac{1}{n_{x'}^2} = \frac{1}{n_o^2} - \gamma_{22}E_y \qquad (2.51)$$

$$\frac{1}{n_{y'}^2} = \frac{1}{2}\left[\left(\frac{1}{n_o^2} + \frac{1}{n_e^2} + \gamma_{22}E_y\right) - \sqrt{\left(\frac{1}{n_o^2} - \frac{1}{n_e^2} + \gamma_{22}E_y\right)^2 + 4\gamma_{51}^2 E_y^2}\right] \qquad (2.52)$$

$$\frac{1}{n_{z'}^2} = \frac{1}{2}\left[\left(\frac{1}{n_o^2} + \frac{1}{n_e^2} + \gamma_{22}E_y\right) + \sqrt{\left(\frac{1}{n_o^2} - \frac{1}{n_e^2} + \gamma_{22}E_y\right)^2 + 4\gamma_{51}^2 E_y^2}\right] \qquad (2.53)$$

Thus, the distorted index can be expressed as

$$\theta = \frac{1}{2}\tan^{-1}\frac{2\gamma_{51}E_y n_o^2 n_e^2}{n_e^2 - n_o^2 + n_o^2 n_e^2 \gamma_{22} E_y} \qquad (2.54)$$

$$n_{x'} = n_o(1 - n_o^2\gamma_{22}E_y)^{-\frac{1}{2}} \qquad (2.55)$$

$$n_{y'} = 2\left[\left(\frac{1}{n_o^2} + \frac{1}{n_e^2} + \gamma_{22}E_y\right) - \sqrt{\left(\frac{1}{n_o^2} - \frac{1}{n_e^2} + \gamma_{22}E_y\right)^2 + 4\gamma_{51}^2E_y^2}\right]^{-\frac{1}{2}} \qquad (2.56)$$

$$n_{z'} = 2\left[\left(\frac{1}{n_o^2} + \frac{1}{n_e^2} + \gamma_{22}E_y\right) + \sqrt{\left(\frac{1}{n_o^2} - \frac{1}{n_e^2} + \gamma_{22}E_y\right)^2 + 4\gamma_{51}^2E_y^2}\right]^{-\frac{1}{2}} \qquad (2.57)$$

In reality, the rotation angle θ is very small. With γ_{51} = 28 pm/V, γ_{22} = 3.4 pm/V, n_e = 2.21; n_0 = 2.3 and a voltage of 1kV applied across a 1mm thick crystal, θ is around 0.1^0. Therefore, we can actually neglect the rotation of the indicatrix, and the results can be approximated as

$$n_{x'} = n_o(1 + \frac{1}{2}n_o^2\gamma_{22}E_y) \qquad (2.58)$$

$$n_{y'} = n_o(1 - \frac{1}{2}n_o^2\gamma_{22}E_y) \qquad (2.59)$$

$$n_{z'} = n_e \qquad (2.60)$$

When the external electric field is along x (E_x=E, E_y = E_z =0), the formula can be derived as

$$\left(\frac{1}{n_o^2}\right)x^2 + \left(\frac{1}{n_o^2}\right)y^2 + \left(\frac{1}{n_e^2}\right)z^2 - 2\gamma_{22}E_x xy + 2\gamma_{51}E_x xz = 1 \qquad (2.61)$$

Introduced by the cross term both in x-y and x-z area, all x, y, and z are no longer the principal axes. The effect of the field causes the crystal to become biaxial that rotates the indicatrix in the x-y and x-z plane. However, such rotation effect is comparable to the rotation angle θ calculated under the condition of E_y applied. Therefore, we can also neglect such rotation effect, and the index can be expressed as

$$n_{x'} \approx \left[\frac{1}{n_o^2} + \frac{1}{n_e^2} + \gamma_{22}(sin2\beta + cos2\beta)\right]^{-\frac{1}{2}} \qquad (2.62)$$

$$n_{y'} \approx \left[\frac{1}{n_o^2} + \frac{1}{n_e^2} + \gamma_{22}(sin2\beta + cos2\beta)\right]^{-\frac{1}{2}} \qquad (2.63)$$

$$n_{z'} \approx \left[\frac{1}{n_o^2} + \frac{1}{n_e^2} + \gamma_{22}(sin2\beta - cos2\beta)\right]^{-\frac{1}{2}} \qquad (2.64)$$

, where β is the rotation angle off the principal axis. Under the condition of 106 V/m, β ≈ π/8.

For BTO, the crystal structure is cubic above 120^0C. Cooling below 120°C causes the cubic phase of barium titanate to transform to a tetragonal phase. The crystalline phase is reached after cooling to ~ 0°C from tetragonal is orthorhombic. Finally, a rhombohedral phase is obtained when the temperature below -90°C. Thus, barium titanate is at its tetragonal phase under room temperature. The electro-optic tensor of tetragonal barium titanate in contracted notation is given by the 3 x 6 matrix:

$$\begin{pmatrix} 0 & 0 & \gamma_{13} \\ 0 & 0 & \gamma_{23} \\ 0 & 0 & \gamma_{33} \\ 0 & \gamma_{51} & 0 \\ \gamma_{51} & 0 & 0 \\ 0 & 0 & 0 \end{pmatrix} \qquad (2.65)$$

Then the change in the optical impermeability is derived as:

$$\begin{pmatrix} \Delta\eta_1 \\ \Delta\eta_2 \\ \Delta\eta_3 \\ \Delta\eta_4 \\ \Delta\eta_5 \\ \Delta\eta_6 \end{pmatrix} = \begin{pmatrix} 0 & 0 & \gamma_{13} \\ 0 & 0 & \gamma_{13} \\ 0 & 0 & \gamma_{33} \\ 0 & \gamma_{51} & 0 \\ \gamma_{51} & 0 & 0 \\ 0 & 0 & 0 \end{pmatrix} \begin{pmatrix} E_1 \\ E_2 \\ E_3 \end{pmatrix}$$

$$\Delta\eta_{ij}(E) = \begin{pmatrix} \gamma_{13}E_3 & 0 & \gamma_{51}E_1 \\ 0 & \gamma_{13}E_3 & \gamma_{51}E_2 \\ \gamma_{51}E_1 & \gamma_{51}E_2 & \gamma_{33}E_3 \end{pmatrix} \qquad (2.66)$$

Thus, the impermeability tensor modulated by the applied electric field can be expressed as

$$\eta_{ij}(E) = \eta_{ij}(0) + \sum_k \gamma_{ijk} E_k = \begin{pmatrix} \frac{1}{n_x^2} & 0 & 0 \\ 0 & \frac{1}{n_y^2} & 0 \\ 0 & 0 & \frac{1}{n_z^2} \end{pmatrix} + \begin{pmatrix} \gamma_{13}E_3 & 0 & \gamma_{51}E_1 \\ 0 & \gamma_{13}E_3 & \gamma_{51}E_2 \\ \gamma_{51}E_1 & \gamma_{51}E_2 & \gamma_{33}E_3 \end{pmatrix} \qquad (2.67)$$

We substitute E_1, E_2, and E_3 as E_x, E_y, and E_z, and the barium titanate index ellipsoid can be derived as

$$\sum_{i,j=1,2,3} \eta_{ij} x_i x_j = 1 \qquad (2.68)$$

$$\left(\frac{1}{n_o^2} + \gamma_{13}E_z\right) x^2 + \left(\frac{1}{n_o^2} + \gamma_{13}E_z\right) y^2 + \left(\frac{1}{n_e^2} + \gamma_{33}E_z\right) z^2 + 2\gamma_{51}E_x xz + 2\gamma_{51}E_y yz = 1 \qquad (2.69)$$

Where $n_x = n_y = n_o$, and $n_z = n_e$ for BTO. When the external electric field is along z ($E=E_z$, $E_x = E_y = 0$), the equation can be derived as

$$\left(\frac{1}{n_o^2} + \gamma_{13}E_z\right) x^2 + \left(\frac{1}{n_o^2} + \gamma_{13}E_z\right) y^2 + \left(\frac{1}{n_e^2} + \gamma_{33}E_z\right) z^2 = 1 \qquad (2.70)$$

gives

$$\frac{1}{n_{x'}^2} = \frac{1}{n_o^2} + \gamma_{13}E_z \qquad (2.71)$$

$$\frac{1}{n_{y'}^2} = \frac{1}{n_o^2} + \gamma_{13}E_z \qquad (2.72)$$

$$\frac{1}{n_{z'}^2} = \frac{1}{n_e^2} + \gamma_{33}E_z \qquad (2.73)$$

Then we have

$$n_{x'}^2 = n_{y'}^2 = n_o^2\left(\frac{1}{1+n_o^2\gamma_{13}E_z}\right) \qquad (2.74)$$

$$n_{z'}^2 = n_e^2\left(\frac{1}{1+n_e^2\gamma_{33}E_z}\right) \qquad (2.75)$$

gives

$$n_{x'} = n_o(1 + n_o^2\gamma_{13}E_z)^{-\frac{1}{2}} \qquad (2.76)$$

$$n_{y'} = n_o(1 + n_o^2\gamma_{13}E_z)^{-\frac{1}{2}} \qquad (2.77)$$

$$n_{z'} = n_e(1 + n_e^2\gamma_{33}E_z)^{-\frac{1}{2}} \qquad (2.78)$$

Using the approximation $(1+\Delta)^{-1/2} \approx 1 - \frac{1}{2}\Delta$, when $|\Delta|$ is a small value.

$$n_{x'} = n_o(1 - \frac{1}{2}n_o^2\gamma_{13}E_z) \qquad (2.79)$$

$$n_{y'} = n_o(1 - \frac{1}{2}n_o^2\gamma_{13}E_z) \qquad (2.80)$$

$$n_{z'} = n_e(1 - \frac{1}{2}n_e^2\gamma_{33}E_z) \qquad (2.81)$$

When the external electric field is along y (E_y=E, E_z = E_x =0), the equation can be derived as

$$\frac{x^2}{n_o^2} + \frac{y^2}{n_o^2} + \frac{z^2}{n_e^2} + 2\gamma_{51}E_y yz = 1 \qquad (2.82)$$

The index ellipsoid is deformed and y-z are no longer the principal axes. The index ellipsoid is tilted in the y-z plane counterclockwise by angle θ, and construct the new x', y', z' system is structured. Then we obtain

$$n_{x'} = n_o \qquad (2.83)$$

$$\tan 2\theta = \frac{2n_o^2 n_e^2 \gamma_{51} E_y}{n_e^2 - n_0^2} \qquad (2.84)$$

$$\frac{1}{n_{y'}^2} = \frac{1}{2}\left[\frac{1}{n_o^2} + \frac{1}{n_e^2} - \sqrt{(\frac{1}{n_o^2} - \frac{1}{n_e^2})^2 + (2\gamma_{51}E_y)^2}\right] \qquad (2.85)$$

$$\frac{1}{n_{z'}^2} = \frac{1}{2}\left[\frac{1}{n_o^2} + \frac{1}{n_e^2} + \sqrt{(\frac{1}{n_o^2} - \frac{1}{n_e^2})^2 + (2\gamma_{51}E_y)^2}\right] \qquad (2.86)$$

Thus, the distorted index can be expressed as

$$\theta = \frac{1}{2}\tan^{-1}\frac{2n_o^2 n_e^2 \gamma_{51} E_y}{n_e^2 - n_0^2} \qquad (2.87)$$

$$n_{x'} = n_o \qquad (2.88)$$

$$n_{y'} = \left[\frac{1}{2n_o^2} + \frac{1}{2n_e^2} - \frac{1}{2}\sqrt{(\frac{1}{n_o^2} - \frac{1}{n_e^2})^2 + (2\gamma_{51}E_y)^2}\right]^{-\frac{1}{2}} \qquad (2.89)$$

$$n_{z'} = \left[\frac{1}{2n_o^2} + \frac{1}{2n_e^2} + \frac{1}{2}\sqrt{(\frac{1}{n_o^2} - \frac{1}{n_e^2})^2 + (2\gamma_{51}E_y)^2}\right]^{-\frac{1}{2}} \qquad (2.90)$$

Using the approximation $(1 + \Delta)^a \approx 1 + a\Delta$, when $|\Delta|$ is a small value

$$n_{x'} = n_o \qquad (2.91)$$

$$n_{y'} = n_o + \frac{n_o^5 n_e^2 \gamma_{51}^2 E_y^2}{2(n_o^2 - n_e^2)} = n_o + \frac{n_o^3}{2}\gamma_{51}E_y \tan\theta \qquad (2.92)$$

$$n_{z'} = n_e - \frac{n_o^2 n_e^5 \gamma_{51}^2 E_y^2}{2(n_o^2 - n_e^2)} = n_e - \frac{n_e^3}{2}\gamma_{51}E_y \tan\theta \qquad (2.93)$$

When the external electric field is along x (E_x=E, E_y = E_z =0), the equation can be derived as

$$\frac{x^2}{n_o^2} + \frac{y^2}{n_o^2} + \frac{z^2}{n_e^2} + 2\gamma_{51}E_x xz = 1 \qquad (2.94)$$

The index ellipsoid is deformed and x-z are no longer the principal axes. The index ellipsoid is tilted in the x-z plane counterclockwise by angle θ, and we have

$$n_{y'} = n_o \qquad (2.95)$$

$$\tan 2\theta = \frac{2n_o^2 n_e^2 \gamma_{51} E_x}{n_e^2 - n_0^2} \qquad (2.96)$$

$$\frac{1}{n_{x'}^2} = \frac{1}{2}\left[\frac{1}{n_o^2} + \frac{1}{n_e^2} - \sqrt{(\frac{1}{n_o^2} - \frac{1}{n_e^2})^2 + (2\gamma_{51}E_x)^2}\right] \qquad (2.97)$$

$$\frac{1}{n_{z'}^2} = \frac{1}{2}\left[\frac{1}{n_o^2} + \frac{1}{n_e^2} + \sqrt{(\frac{1}{n_o^2} - \frac{1}{n_e^2})^2 + (2\gamma_{51}E_x)^2}\right] \qquad (2.98)$$

Thus, the distorted index can be expressed as

$$\theta = \frac{1}{2}\tan^{-1}\frac{2n_o^2 n_e^2 \gamma_{51} E_x}{n_e^2 - n_0^2} \qquad (2.99)$$

$$n_{x'} = \left[\frac{1}{2n_o^2} + \frac{1}{2n_e^2} - \sqrt{(\frac{1}{n_o^2} - \frac{1}{n_e^2})^2 + (2\gamma_{51}E_x)^2}\right]^{-\frac{1}{2}} \qquad (2.100)$$

$$n_{y'} = n_o \qquad (2.101)$$

$$n_{z'} = \left[\frac{1}{2n_o^2} + \frac{1}{2n_e^2} + \sqrt{(\frac{1}{n_o^2} - \frac{1}{n_e^2})^2 + (2\gamma_{51}E_x)^2}\right]^{-\frac{1}{2}} \qquad (2.102)$$

Using the approximation $(1 + \Delta)^a \approx 1 + a\Delta$, when $|\Delta|$ is a small value

$$n_{x'} = n_o + \frac{n_o^5 n_e^2 \gamma_{51}^2 E_x^2}{2(n_o^2 - n_e^2)} = n_o + \frac{n_o^3}{2}\gamma_{51}E_x \tan\theta \qquad (2.103)$$

$$n_{y'} = n_o \qquad (2.104)$$

$$n_{z'} = n_e - \frac{n_o^2 n_e^5 \gamma_{51}^2 E_x^2}{2(n_o^2 - n_e^2)} = n_e - \frac{n_e^3}{2}\gamma_{51}E_x \tan\theta \qquad (2.105)$$

2.2.3 Polarization Modulation

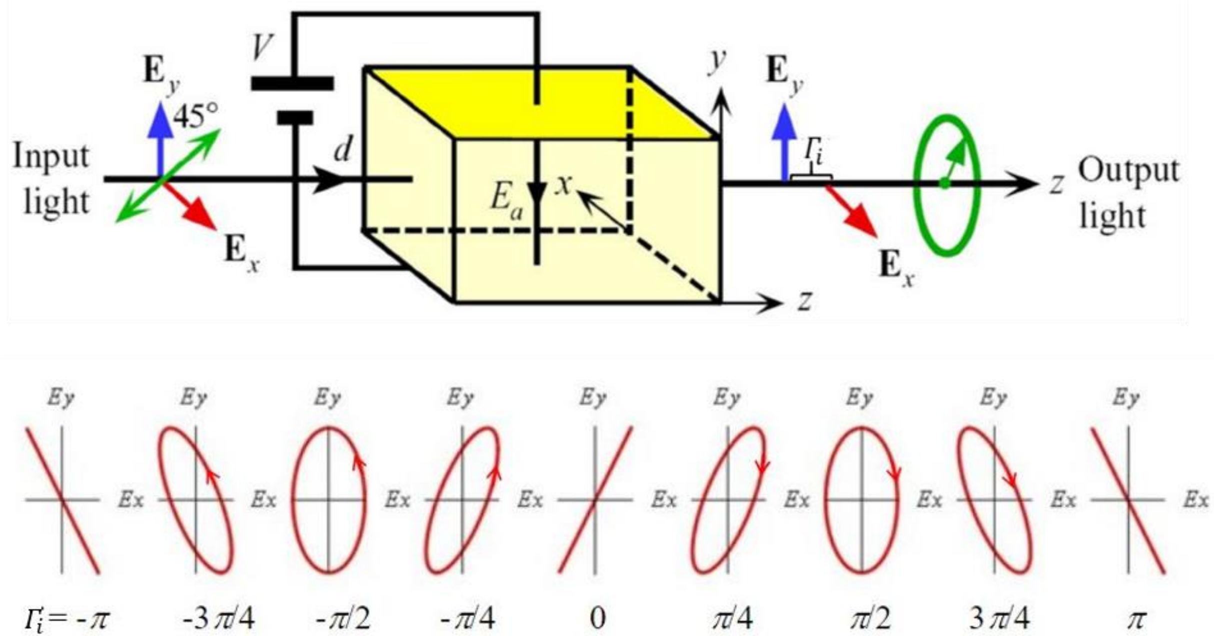

Figure 2.5 Schematic of the polarization change caused by phase retardation.

Polarization modulation involves the coherent addition of two orthogonal waves, resulting in a change of the input polarization state at the output. The crystal and applied voltage are configured to produce temporary fast and slow axes in the crystal cross-section. The polarizer is positioned

such that the input light is decomposed equally into the two orthogonal linear eigen polarizations along these axes.

Assume the propagation wave is along z-direction. After propagating a distance L, the wave components along x and y-direction undergo a phase retardation given by

$$\Gamma = k_0[n_1(E) - n_2(E)]L = k_0(n_1 - n_2)L + k_0\big(\Delta n_1(E) - \Delta n_2(E)\big)L = \Gamma_0 + \Gamma_i \qquad (2.106)$$

where Γ_0 represents the natural retardation without applied field, and Γ_i is the field-induced part of the retardation. As shown in Figure 2.5, the output wave is elliptically polarized in general. Special points are $\Gamma_i = \pi/2$, where the electrical field vector is circularly polarized, and $\Gamma_i = \pi$, where the wave is again linearly polarized, but rotated by 90^0 to its input direction of polarization.

CHAPTER III

MID-INFRARED WAVEGUIDE SENSORS

This chapter introduces mid-IR sensor applications based on BTO and AlN. Three different waveguide sensors are proposed: *i.* Si-on-BTO waveguide sensor; *ii.* Si-on-AlN waveguide sensor; *iii.* flexible AlN waveguide sensor. The detailed device design and fabrication process are introduced. Further, the device optical property and sensing effect are evaluated.

3.1 Measurement System Set-up

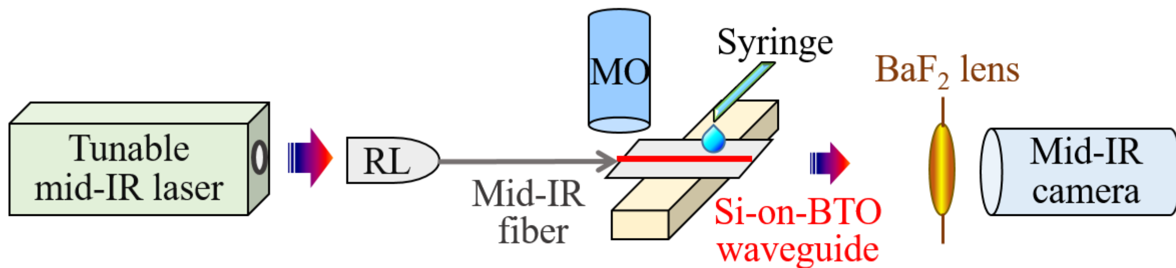

Figure 3.1 Schematic of the sensing station.

All the fabricated sensors are characterized by the designed testing station. As shown in Figure 3.1. The light source is a pulsed laser with a wavelength tunable from λ = 2.5 μm to λ = 3.7 μm and a linewidth of 3 cm^{-1}. It has a pulse repetition rate of 150 kHz, a pulse duration of 10 nano seconds, and 150 mW average power. Using a reflective lens, the probe light is first collimated into a fluoride fiber that has a 9 μm core and 125 μm cladding, and then butt coupled into the waveguide. The core of the mid-IR fiber is lined up with the smoothly cleaved front facet of waveguides. The fine alignment between the optical fiber and the waveguide is monitored by an upper microscope equipped with a long working distance 10x objective lens. The mid-IR signals

from the waveguides are focused by a calcium fluoride biconvex lens with 25 mm focal length and then imaged by a liquid nitrogen cooled 640 x 512 pixel InSb camera.

In the tests of chemical sensing, the selected target analytes solution is dropped from a syringe onto the fabricated waveguide sensor to covers the entire waveguide array. In parallel, the mid-IR camera record the light mode intensity change at the other end of the waveguide.

3.2 Silicon on Barium Titanate Waveguide Sensor*

A monolithic mid-IR micro-photonics platform consisting of a-Si with epitaxial BTO thin films was fabricated and exploited. This platform reveals numerous advantages from the aspects of *i.* Integration of functional materials, *ii.* Compatibility with CMOS fabrication process, and *iii.* Multifunctionality by repositioning the waveguide modes within different layers. First, (*i*) our developed PLD technique provides crystalline BTO films while avoiding the fabrication complexity required in LN thin film preparation.[50,51] The present LN film preparation involves crystal slicing, high-temperature annealing, and exfoliation. In addition, our BTO thin film has a broad infrared transparent spectrum up to $\lambda = 7$ μm compared to LN crystals that become opaque after $\lambda = 5$ μm.[52] Meanwhile, Si has a higher refractive index so it can efficiently guide mid-IR light in our monolithic device. Second, *(ii)* we are able to create our mid-IR waveguides on the a-Si layer using the CMOS process that prevents the difficulties in directly patterning on the chemical insert and mechanical hard BTO film. Third, *(iii)* we can position the waveguide modes in the ferroelectric BTO layer for high-speed electro-optical modulation, or alternatively, we can shift the mode to align with the a-Si layer for biochemical sensing. Hence, by engineering the

* Parts of this section are reprinted with permission from [20]

device structure our monolithic mid-IR platform is capable of serving various applications including reconfigurable photonic circuits and label-free chemical detections.

3.2.1 Device Fabrication and Materials Characterization

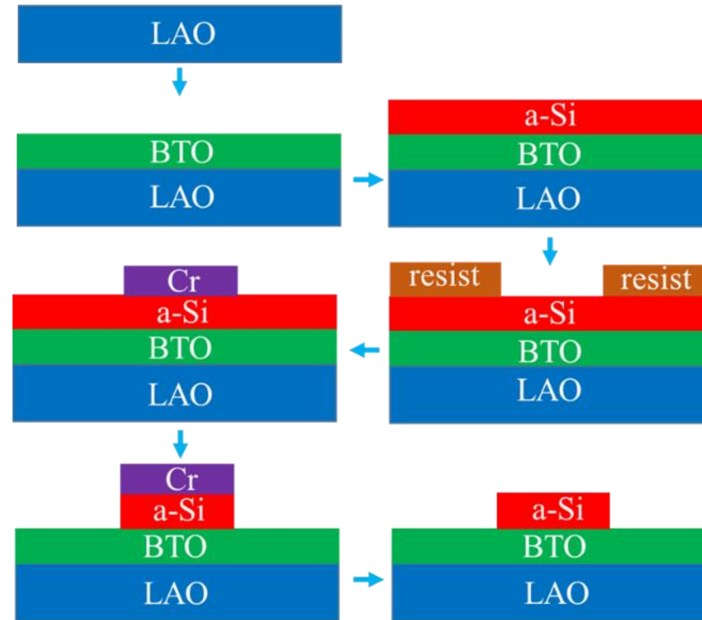

Figure 3.2 The fabrication process of monolithic mid-IR microphotonics using a-Si ridge waveguides on the BTO thin film. The epitaxial BTO film is deposited on a single-crystal $LaAlO_3$ (001) substrate by PLD technique, and a-Si thin film is then grown on the BTO/LAO substrate by PECVD method. Using photolithography and lift-off the waveguide structure is first defined by Cr mask, and then transferred to the a-Si layer by RIE. At last, the Cr mask is removed by ceric ammonium nitrate solution and followed by oxygen plasma ashing to remove the organic residue.

The detailed fabrication process is illustrated in Figure 3.2. A pure BTO target is prepared using a conventional ceramic sintering method. The BTO film is deposited on a single-crystal $LaAlO_3$ (001) substrate by a 10 Hz KrF excimer pulsed laser (Lambda Physik, $\lambda = 248$ nm). The deposition temperature is 700 ^oC and the pressure of the O_2 inside the deposition chamber is 40 mTorr. After the BTO deposition, the film is annealed at 600 ^oC with 200 Torr O_2 pressure for 1 hour and then cooled down to room temperature. The resulting microstructure and crystal orientation of the BTO film are characterized by X-ray diffraction (XRD, PANalytical Empyrean). After the film grown,

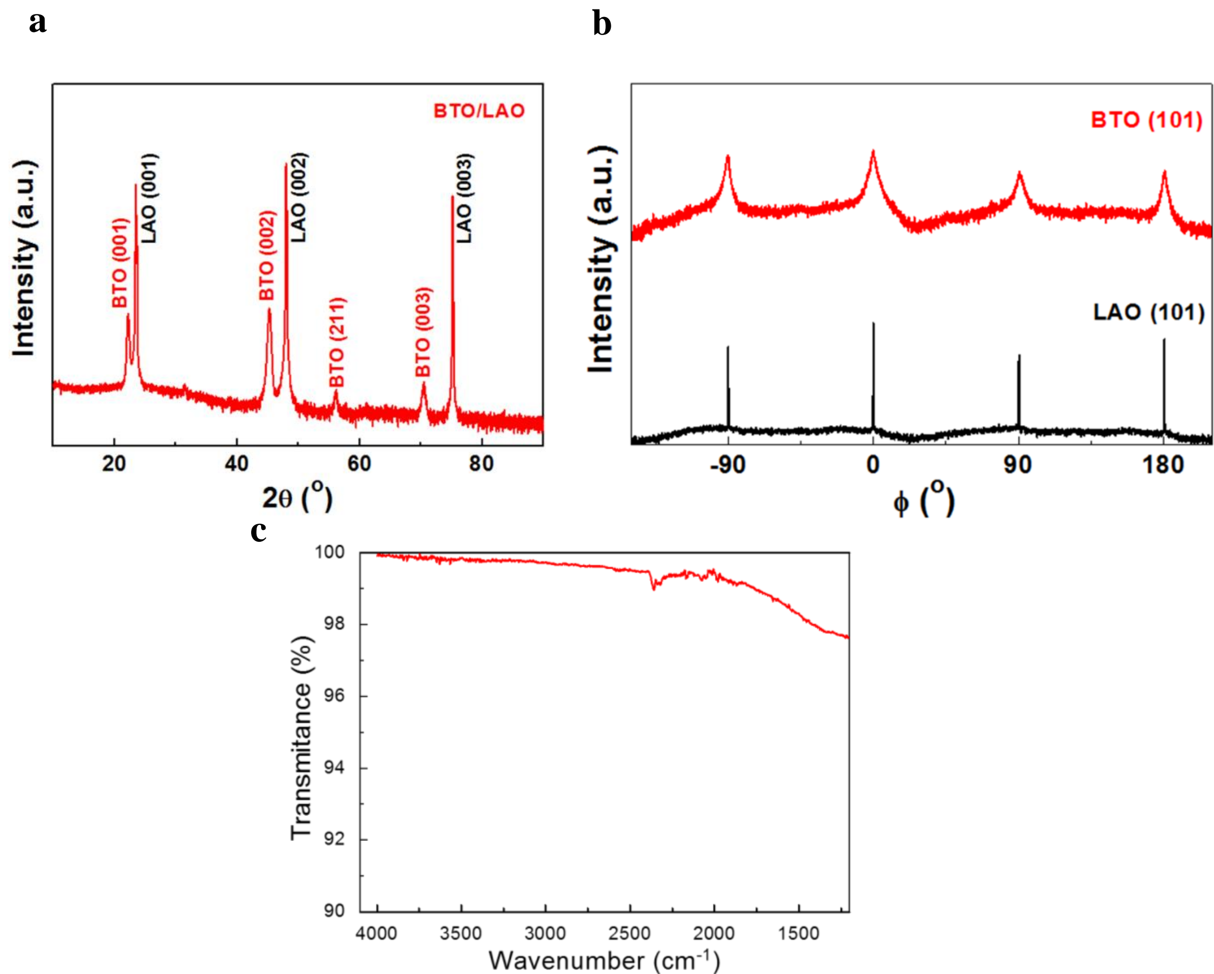

Figure 3.3 (a) The XRD θ-2θ scan of our epitaxially grown BTO thin film on LAO (001) substrate. The dominant (00l)-type diffraction peaks indicate the BTO film mainly grows along the (00l) direction. When the BTO film thickness increases, the film becomes polycrystalline from the minor BTO (211) peak at ~56.0°. (b) The phi scans of BTO (101) and LAO (101) indicate that the BTO thin film has cube-on-cube growth on the LAO substrate and has good crystallinity without in-plane rotation. (c) The infrared absorption spectrum of our deposited BTO thin film from ATR-FTIR measurement. High transmittance is found between 4000 cm^{-1} (λ = 2.5 μm) to 1430 cm^{-1} (λ = 7.0 μm). The increased absorption after 1430 cm^{-1} (λ = 7.0 μm) is due to a combination of various fundamental vibration modes existing at longer wavelengths. Reprinted with permission from [20]

1 μm thick a-Si thin film was deposited on the BTO/LAO substrate by plasma-enhanced chemical vapor deposition (PECVD). The precursor gas for the a-Si deposition is SiH_4, and the deposition temperature is 200 °C. By utilizing a-Si thin film, we are able to relieve the restraint of the crystal lattice matching condition that allows for the formation of a smooth interface between the

crystalline BTO layer and the Si device layer. The waveguide structure is defined by photolithography where a 50 nm thick Cr mask is prepared by electron beam evaporation followed by the lift-off process. The waveguide structure is then transferred to the a-Si layer by reactive ion etching (RIE). SF_6 is used for selective Si etching as it will not react with the BTO film, and therefore it prevents BTO surface roughness due to ion damage. Past studies that utilize HF solution for etching BTO have shown ununiformed surfaces and roughed waveguide edges. It is vital to have sharp Si waveguide facets as well as smooth BTO surfaces to reduce waveguide propagation loss and scattering loss. Finally, the Cr mask and the organic residue on the device surface are removed by ceric ammonium nitrate solution and followed by oxygen plasma ashing.

The crystal structure of the epitaxially grown BTO thin film on LAO (001) substrate is characterized by XRD θ-2θ scan. As shown in Figure 3.3a, the BTO thin film mainly grows along the (00*l*) direction as indicated by dominant (00*l*)-type diffraction peaks. However, with the increase of the BTO film thickness, the BTO becomes polycrystalline as shown by the minor BTO (211) peak at ~56.0°. Meanwhile, the phi scans of BTO (101) and LAO (101) displayed in Figure 3.3b indicate that the cube-on-cube growth of the BTO thin film on the LAO substrate has good crystallinity without in-plane rotation. The infrared absorption spectrum of our deposited BTO thin film is measured by attenuated total reflection - Fourier transform infrared spectroscopy (ATR-FTIR) and the result is displayed in Figure 3.3c. High transmittance is found at a broad mid-IR spectrum between 4000 cm^{-1} (λ = 2.5 μm) to 1430 cm^{-1} (λ = 7.0 μm). The minor absorption at 2400 cm^{-1} (λ = 4.2 μm) is possibly caused by the inorganic residuals from PLD growth. The increased absorption after 1430 cm^{-1} (λ = 7.0 μm) is due to combinations of various fundamental vibration modes existing at longer wavelengths, such as absorption bands at 500 - 600 cm^{-1} (16.6 - 20 μm) and at 350 - 400 cm^{-1} (25.0 - 28.5 μm) that are attributed to the Ti-O stretching and bending

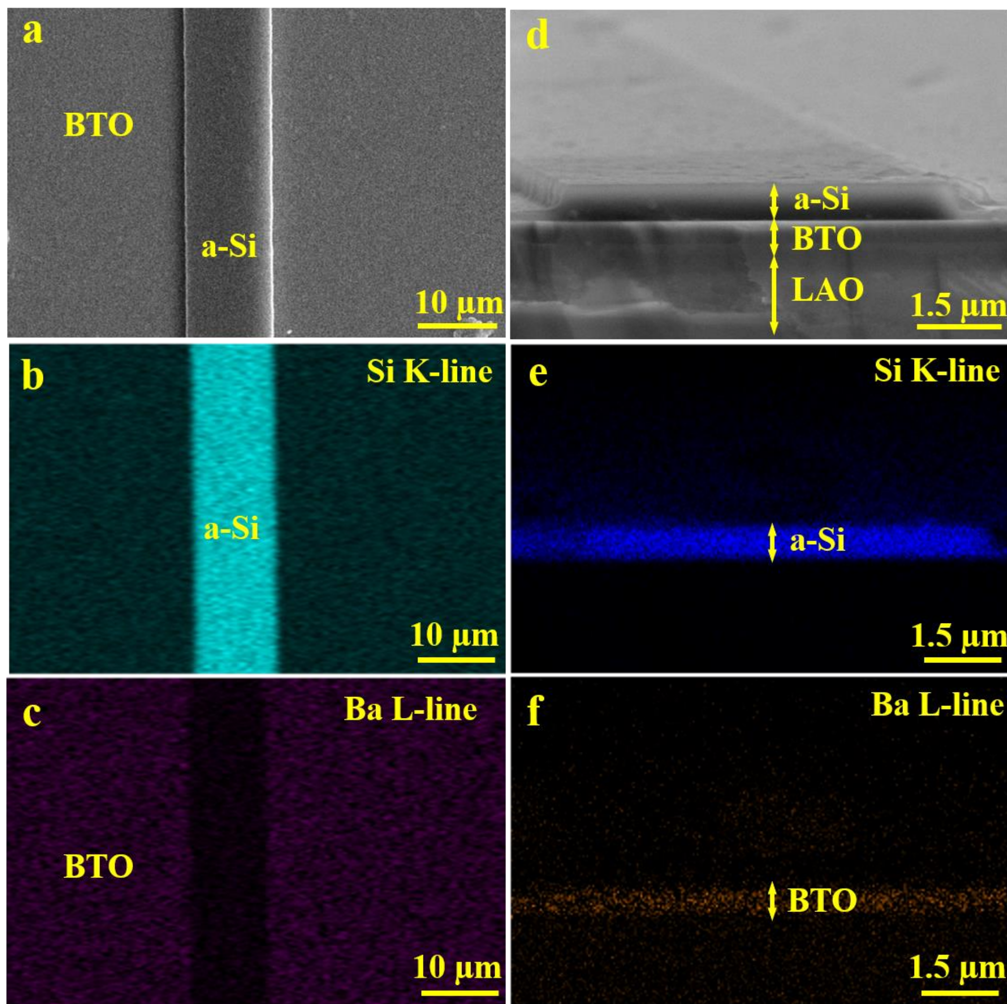

Figure 3.4 The morphology and the composition of our mid-IR devices from SEM and EDX inspection. SEM images of a 10 μm wide a-Si on BTO waveguide captured from (a) the top and (b) cross-sectional. A smooth waveguide surface and sharp waveguide edges are observed. EDX mapping from the top of the waveguide using (c) Si Kα and (d) Ba Lα emission lines. Another EDX mapping along the waveguide front facet using (e) Si Kα and (f) Ba Lα. The a-Si and BTO thin films both show homogeneous compositions across the film surface and along the film depth. Reprinted with permission from [20]

---

vibrations, respectively.[53, 54] Since Si is transparent up to 8.0 μm, our integrated a-Si on BTO platform is capable of operations up to λ = 7.0 μm, which is broader than the present Si on LN devices limited to λ = 5.0 μm as well as the Si on sapphire devices limited to λ = 4.5 μm.

The morphology of the mid-IR devices is inspected by scanning electron microscopy (SEM). To reduce the waveguide propagation loss caused by light scattering, it is critical to minimize structure defects that may possibly be created on the waveguide's edges or surfaces. Figure 3.4a shows the top images of a 10 μm wide a-Si on BTO waveguide. It has a well-defined ridge profile without any bending or distortion found on the edge, nor cracks or indents on the waveguide surfaces and the BTO film. From the cross-sectional image shown in Figure 3.4d, the facets and the side walls of the waveguide are sharp and also absent of bumps and indentations. In addition, the clearly resolved interface between the top Si waveguide and the under-cladding BTO layer indicates that no depletion damage has been introduced during the fabrication process. Meanwhile, the material composition of our monolithic a-Si on BTO platform is characterized by energy-dispersive X-ray spectroscopy (EDS) using emission lines of Si Kα at 1.74 keV and Ba Lα at 4.47 keV. The elemental spatial distributions of Si and Ba also reveal the device profiles belonging to the a-Si ridge waveguide and to the BTO layer. Figure 3.4b and c display the EDS mapping results from the top of the device, where a Si waveguide and its neighboring BTO film are clearly resolved. Likewise, from the cross-sectional EDS mapping shown in Figure 3.4e and f, the waveguide height and the BTO film thickness are determined to be 1 μm and 0.5 μm, respectively. From EDS mapping results, we are able to confirm that the grown a-Si and BTO thin films have homogeneous compositions across the film surface as well as along the film depth. The obtained uniformity of the material compositions prevents optical scattering loss caused by variation of refractive indexes.

3.2.2 Optical Property Simulation

Based on the device structure shown in Figure 3.4, we numerically calculate the propagating modes of our a-Si on BTO waveguide over the spectrum from λ = 2.4 μm to 3.8 μm. The

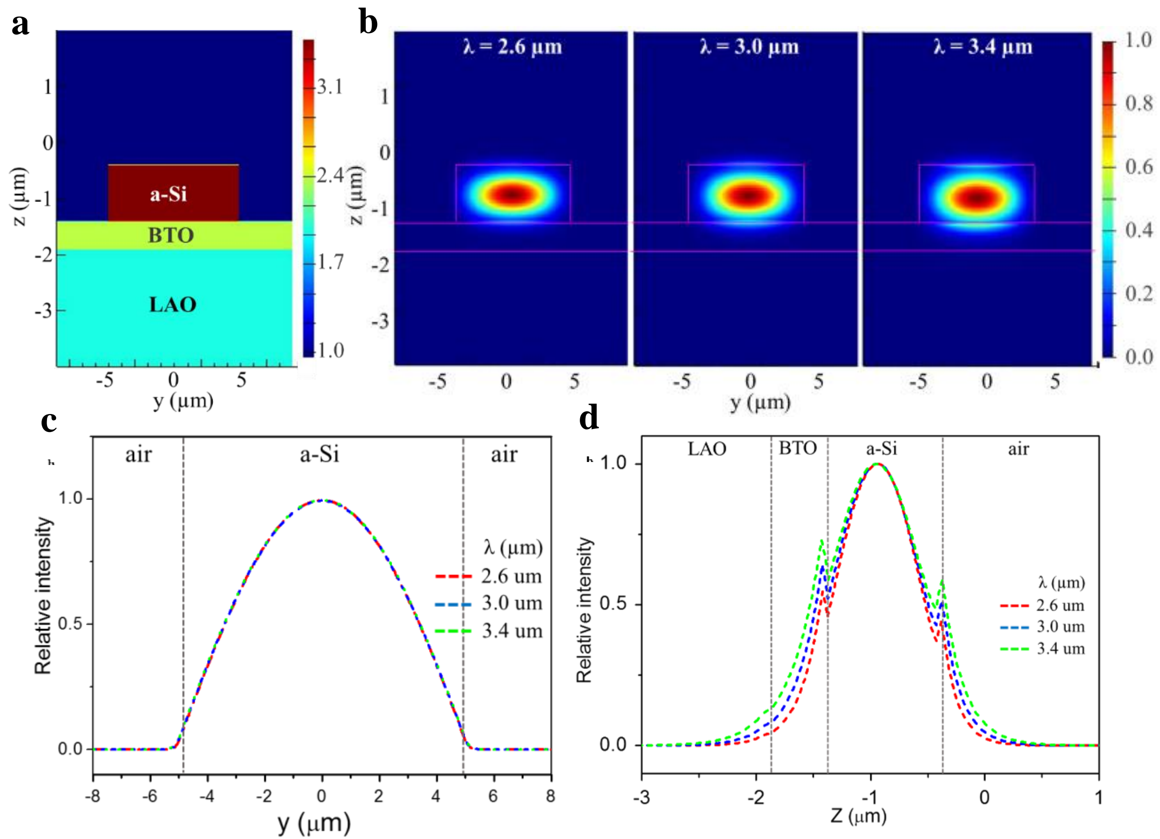

Figure 3.5 (a) The device configuration and the refractive index profile applied in our FDTD modeling. The refractive indexes, $\mathbf{n_{Si}}$, $\mathbf{n_{BTO}}$, and $\mathbf{n_{LAO}}$, are 3.4, 2.4, and 2.0, respectively. (b) The optical fields of our mid-IR waveguides calculated at λ = 2.6 μm, 3.0 μm, and 3.4 μm. Fundamental modes with similar ellipsoid intensity distributions are resolved in the Si layer in all three wavelengths. (c) and (d) are the calculated 1D intensity profiles along the y axis and z axis, respectively. In the y direction, a sharp Gaussian profile is found inside the a-Si ridge waveguide. On the other hand, the optical field expands extensively into the BTO layer along the z direction. Reprinted with permission from [20]

simulations are performed by the two-dimensional finite difference time domain (FDTD) method. Figure 3.5a illustrates the device configuration and the refractive index profile applied in our device modeling. The a-Si waveguide has 10 μm width and 1 μm thickness. Underneath the Si is a 0.5 μm thick BTO layer and an LAO substrate. The refractive indexes, $\mathbf{n_{Si}}$, $\mathbf{n_{BTO}}$, and $\mathbf{n_{LAO}}$, are 3.4, 2.4, and 2.0, respectively. A 12 μm × 6 μm light source is chosen to excite the waveguide mode since its size is comparable to the mid-IR fiber, which has a core diameter of 9 μm, used in

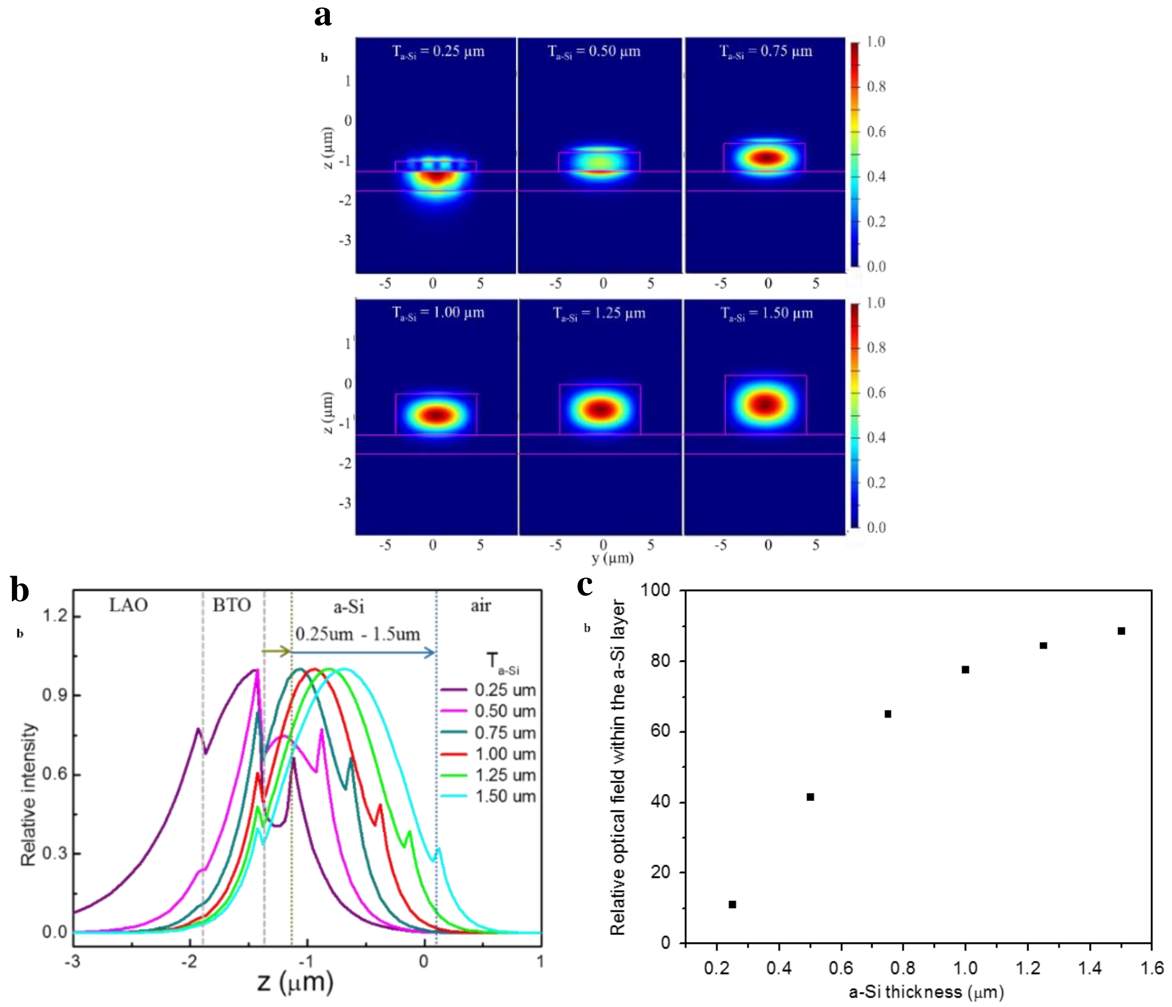

Figure 3.6 (a) The calculated optical field when the thickness of the a-Si layer, $\mathbf{T_{a\text{-}Si}}$, increases from 0.25 µm to 1.5 µm, but the BTO layer remains at 0.5 µm. (b) The calculated 1-D intensity profiles parallel to the z direction at y = 0 µm. (c) The calculated optical field confined inside the a-Si layer at different $\mathbf{T_{a\text{-}Si}}$. The optical field shifts upward from the BTO layer to the a-Si layer as the $\mathbf{T_{a\text{-}Si}}$ increases. Reprinted with permission from [20]

---

our experiments. Figure 3.5b depicts the optical field of our mid-IR waveguides calculated at λ = 2.6 µm, 3.0 µm, and 3.4 µm. Fundamental modes with similar ellipsoid intensity distribution are clearly resolved in the Si layer while the optical field inside the BTO layer (beneath z = -1.5 µm) is gradually increased as the probe light shifts to longer wavelengths. To better analyze the mode properties, the calculated 1D intensity profiles along y-axis and z-axis are plotted in Figure 3.5c and d, respectively. In the y-direction, the optical field shows a sharp single Gaussian profile well

confined by the a-Si ridge waveguide due to the high refractive index contrast between $\mathbf{n_{Si}}$ of 3.4 and $\mathbf{n_{air}}$ of 1. On the other hand, along with the z-direction, the optical field expands extensively into the BTO layer and has a notable increase as the wavelength increases from $\lambda = 2.6$ to 3.4 µm. The strong field found within the BTO layer is attributed to the relevantly high refractive index of the BTO film, $\mathbf{n_{BTO}} = 2.4$, as well as its small thickness.

Hence, for different applications, we are able to manipulate the light intensity distribution across the multilayers that consist of a-Si, BTO, and LAO layers by adjusting the height of the BTO layer. For instance, in biochemical sensing, a multilayer structure is created so the waveguide mode is located in the upper a-Si layer, while its evanescent field extends into the external medium that eventually will be absorbed by the analytes surrounding the waveguide. Then, by correlating the spectral attenuation of the mode intensity with characteristic absorption spectra from various chemicals, we are able to identify the analyte composition and concentration. On the other hand, to implement electro-optical modulation, we adjust the multilayer structure so that the waveguide mode can extensively overlap with the ferroelectric BTO layer. The images of mode profiles displayed in Figure 3.6a demonstrate our methodology for varying the positions of the waveguide mode. Here, the thickness of the a-Si layer, $\mathbf{T_{a\text{-}Si}}$, increases from 0.25 µm to 1.5 µm, but the BTO layer remains at 0.5 µm. At $\mathbf{T_{a\text{-}Si}} = 0.25$ µm, most of the optical field resides within the BTO layer since the thin a-Si layer is not able to support a waveguide mode. When $\mathbf{T_{a\text{-}Si}}$ increases to 0.5 µm, the mode shifts upward into the a-Si layer and even further into the background air while the optical field remaining in the BTO layer significantly decreases. At $\mathbf{T_{a\text{-}Si}} = 0.75$ µm, the center of the waveguide mode lines up with the middle of the a-Si ridge. As a result, the evanescent fields are then able to be observed in the top air cladding as well as in the lower BTO layer. Once $\mathbf{T_{a\text{-}Si}}$ reaches 1 µm or beyond, the optical field becomes substantially confined inside the a-Si layer.

Figure 3.6c shows the dependence of a-Si film thickness on the confinement of the optical field inside the a-Si layer. For a thin a-Si film with $\mathbf{T_{a\text{-}Si}}$ of 0.25 μm, only 11% of the optical field is observed within the a-Si layer indicating most of the optical field resides within the BTO layer. The field gradually shifts from the BTO layer to the a-Si as the $\mathbf{T_{a\text{-}Si}}$ increases. Upon $\mathbf{T_{a\text{-}Si}}$ reaching 0.75 μm, 65% of the optical field has already reallocated to the a-Si layer. Once $\mathbf{T_{a\text{-}Si}}$ increases beyond 1 μm, the majority of the optical field is now confined in the a-Si layer and only the evanescent field is found in the BTO layer.

To better visualize the variation of the optical field when the a-Si thickness changes, Fig. 5 (b) shows the calculated 1-D intensity profiles parallel to the z-direction at y = 0 μm. At $\mathbf{T_{a\text{-}Si}}$ = 0.25 μm, the peak intensity exists in the interface between the a-Si and the BTO layers, and the field gradually decays toward the LAO substrate along the z-direction. At $\mathbf{T_{a\text{-}Si}}$ = 0.50 μm, the mode center is positioned inside the a-Si layer while the two additional intensity peaks belonging to the evanescent fields are found on the top and bottom edges of the a-Si layer. On the other hand, fundamental modes are clearly found when $\mathbf{T_{a\text{-}Si}}$ is 0.75 μm or thicker. The center of the waveguide mode moves along the +z direction, and the evanescent fields beyond and underneath the a-Si film decrease sharply as the a-Si film becomes thicker.

3.2.3 Sensing Effect Characterization

The performance of our a-Si film on BTO waveguides is evaluated, and the results of the mode images and optical loss characterizations are shown in Figure 3.7 and Figure 3.8. From Figure 3.7, a fundamental mode is clearly observed over a broad spectral range from λ = 2.6 μm to λ = 3.4 μm. The mode profiles remain the same at different wavelengths, while minor scattering is observed at longer wavelengths of 3.4 μm. No distortion found in the captured mode images

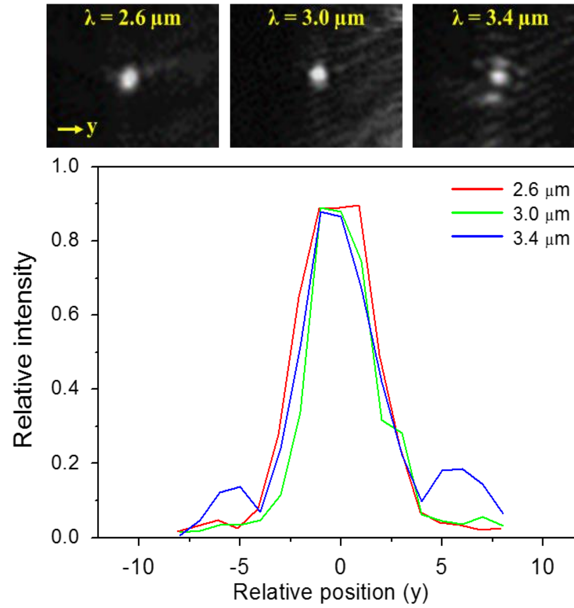

Figure 3.7 The waveguide mode images capture at λ = 2.6 µm to λ = 3.4 µm. Fundamental mode is clearly observed over a broad spectral range. The intensity profiles of the waveguide modes extrapolated along the y direction. A Gaussian profile corresponding to a fundamental mode is found over λ = 2.6 µm to 3.4 µm. Reprinted with permission from [20]

indicates that our waveguides have flat sidewalls and a smooth interface between the a-Si and BTO layer. The high refractive indexes of the a-Si and the BTO also attribute to the observed efficient guiding of the mid-IR light-wave. The intensity profiles of the waveguide modes are then extrapolated and illustrated in Figure 3.7b. A well resolved Gaussian profile corresponding to a fundamental mode is found over λ = 2.6 µm to 3.4 µm, and the result is consistent with the simulated mode profiles displayed in Figure 3.5c and d. Meanwhile, the invariant shape of the mode over a broad spectrum tells us that our waveguide has low dispersion. The optical loss, mode images, and its optical powers from waveguides with different lengths are measured and displayed in Figure 3.8a and b. By fitting the mode intensity attenuation, an optical loss of 4.2 dB/cm is obtained at λ = 3.0 µm, which is comparable to previous studies showing 3.8 dB/cm at λ = 5.2 µm, and lower than 4.5 dB/cm at λ = 1.55 µm in NIR.[55-58] The low optical loss of our a-Si on BTO waveguide can be explained by the high mid-IR transparency of our epitaxial BTO thin film as

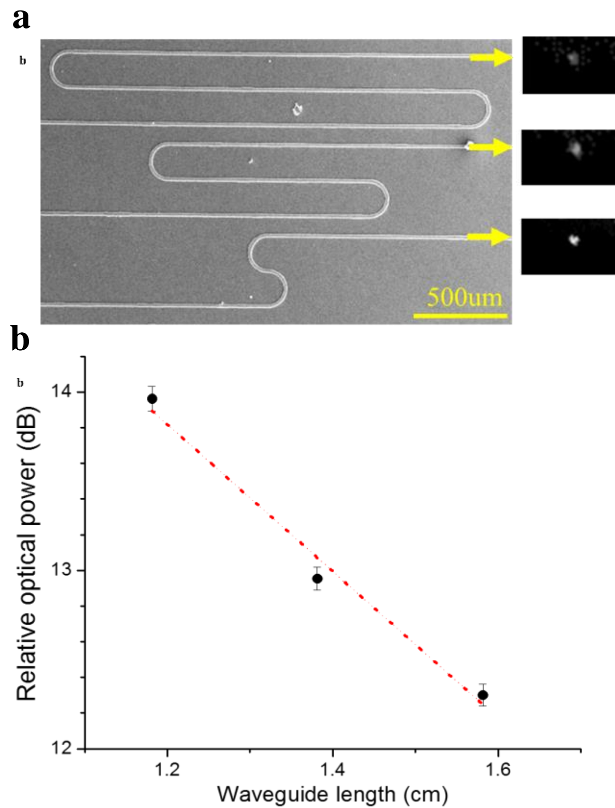

Figure 3.8 (a) Mode images and (b) Relative optical powers measured from the waveguides with different lengths. An optical loss of 4.2 dB/cm is obtained by fitting the mode intensity attenuation at λ = 3.0 µm. Reprinted with permission from [20]

well as by the smooth interface between the a-Si and the BTO layers. In addition, scattering loss caused by surface roughness significantly reduces at longer wavelength since the Rayleigh scattering coefficient is proportional to $1/\lambda^4$. Thus, we experimentally exhibit that our integrated a-Si on BTO waveguides are ideal for broadband mid-IR photonic circuits.

In our experiments, methanol and heptane were selected as the analytes to evaluate the performance of our waveguide sensors due to their strong characteristic absorptions existing in the mid-IR regime. A light source with the TM polarization was utilized since TM light reveals a stronger evanescent field that will attribute to higher sensitivity. The wavelength of the probe light was sequentially scanned between λ = 2.5 µm and 3.2 µm because this spectrum regime overlaps with the absorption bands caused by -OH and -CH functional group while Si-on-BTO is

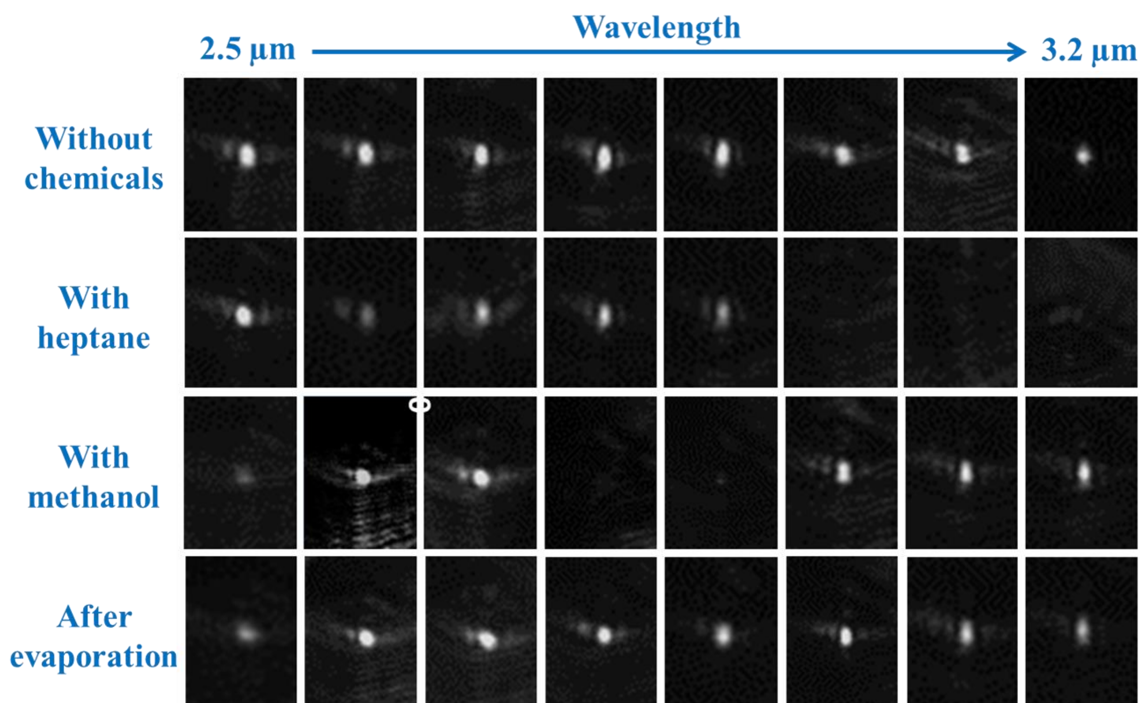

Figure 3.9 The waveguide mode images were captured from λ = 2.5 μm to 3.2 μm with or without chemicals covering the waveguide. Fundamental modes were clearly observed over a broad spectral range. When heptane was presented, the mode disappeared at λ = 3.0 μm - 3.2 μm corresponding to -CH absorption. For methanol, the mode vanished at λ = 2.8 μm - 2.9 μm associating with -OH absorption. The mode intensities recovered when the analytes evaporated from the waveguide surface. Reprinted with permission from [21]

transparent. The waveguide mode images were recorded before and after dropping the chemical analytes onto the waveguide surface. As shown in Figure 3.9, without any chemicals present, a bright and sharp fundamental mode was observed through λ = 2.5 μm to 3.2 μm as expected from the simulation results. Upon dropping the heptane on the waveguide, the mode faded at λ = 3.0 - 3.2 μm due to the absorption caused by the C-H bond stretching. On the other hand, when methanol applies, drastic absorption appeared at λ = 2.8 - 2.9 μm that corresponds to the absorption due to the O-H bond stretching. Hence, our mid-IR sensor reveals distinct spectral attenuations when exposed to different chemicals, and the measured absorption results agree well with the previous studies from FTIR characterization. After the chemicals evaporate, we found that the mode profiles

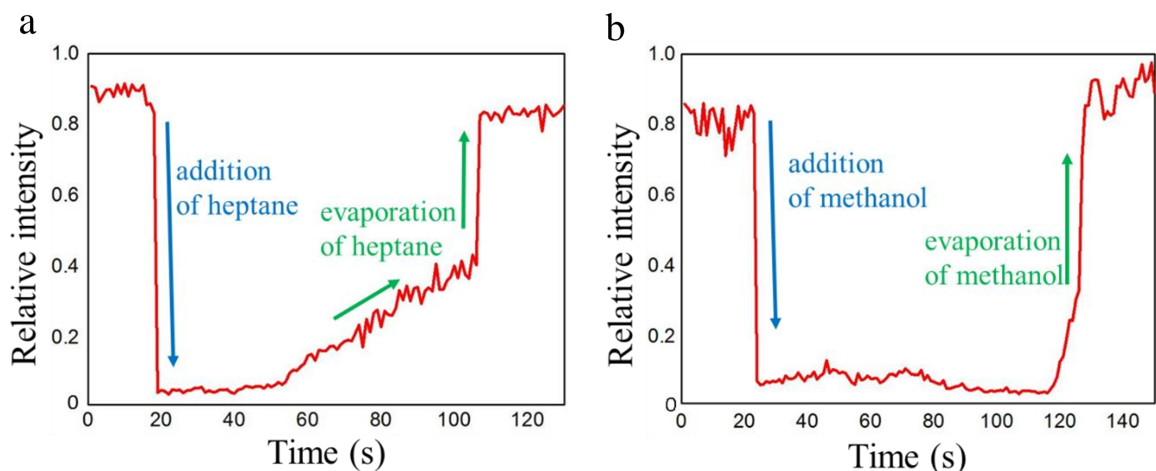

Figure 3.10 Real-time detection of (a) heptane and (b) methanol using mid-IR waveguide sensors at λ = 3.1 μm and 2.9 μm, respectively. The mode intensity decreased when the analytes were dropped on the waveguide surface and then recovered when the analyte evaporated. Reprinted with permission from [21]

recovered and their intensities arrived back at the same levels just as before chemicals were applied. Thus, our mid-IR sensor is not only capable of accurate chemical identification, but it is also reusable.

The real-time chemical detection was performed by reading the transient response of the mid-IR waveguide sensors. For heptane detection, the wavelength of the probe light was tuned to λ = 3.1 μm because it is within the C-H absorption band. The waveguide mode intensity upon adding the chemical is shown in Figure 3.10a. Before t = 20 s the intensity was strong since there was no presence of any analyte. When the heptane was dropped on the waveguide surface at t = 20 s, the intensity decreased dramatically because the analyte, heptane, fully covered the mid-IR waveguide and absorbed its evanescent light. The waveguide intensity remained low until t = 50 s and then it started to recover because the heptane gradually evaporated. Eventually, at t = 110 s, the intensity reached its original level due to the heptane being completely left from the waveguide surface. A similar transient response was observed during the methanol sensing test shown in Figure 3.10b. To track methanol, the light wavelength was shifted to 2.9 μm to match the characteristic O-H

absorption. We found that the light intensity dropped at t = 25 s, which coincided with adding methanol onto the waveguide. After a while, the intensity recovered at t = 120 s indicating the analyte evaporated from the waveguide surface. Our time-resolved characterization demonstrates that the developed mid-IR sensor is suitable for in-situ monitoring of various chemical analytes with high accuracy.

3.3 Silicon on Aluminum Nitride Waveguide Sensor *

AlN is of particular interest because it has a wide transmission spectrum from ultraviolet (UV), visible (VIS), Near Infrared (NIR), up to mid-IR at $\lambda = 10$ μm.[59, 60] AlN also has a large optical nonlinearity so it is suitable for light generation, such as using sum and difference frequency generation or optical parametric oscillation.[61, 62] In addition, AlN is mechanically strong, thermally stable, and chemical resistant, thus enabling it for sensor application under harsh environmental conditions.[63, 64] The integration between AlN thin film with other CMOS materials, like Si, SiO_2, or sapphire, has been achieved through growth techniques including metal organic chemical vapor deposition (MOCVD), molecular beam epitaxy (MBE), and sputtering.[65 - 68] Intrigued by its unique material properties, we create a hybrid platform that implements AlN within Si photonics to achieve broadband mid-IR wave guiding as well as label-free chemical sensing.[69]

3.3.1 Device Fabrication and Material Characterization

The detailed fabrication process is shown in Figure 3.11 3 μm AlN film was deposited on <100> silicon wafer by DC sputtering (Kurt J. Lesker), where the sputtering material was a 4-inch

* Parts of this section are reprinted with permission from [69]

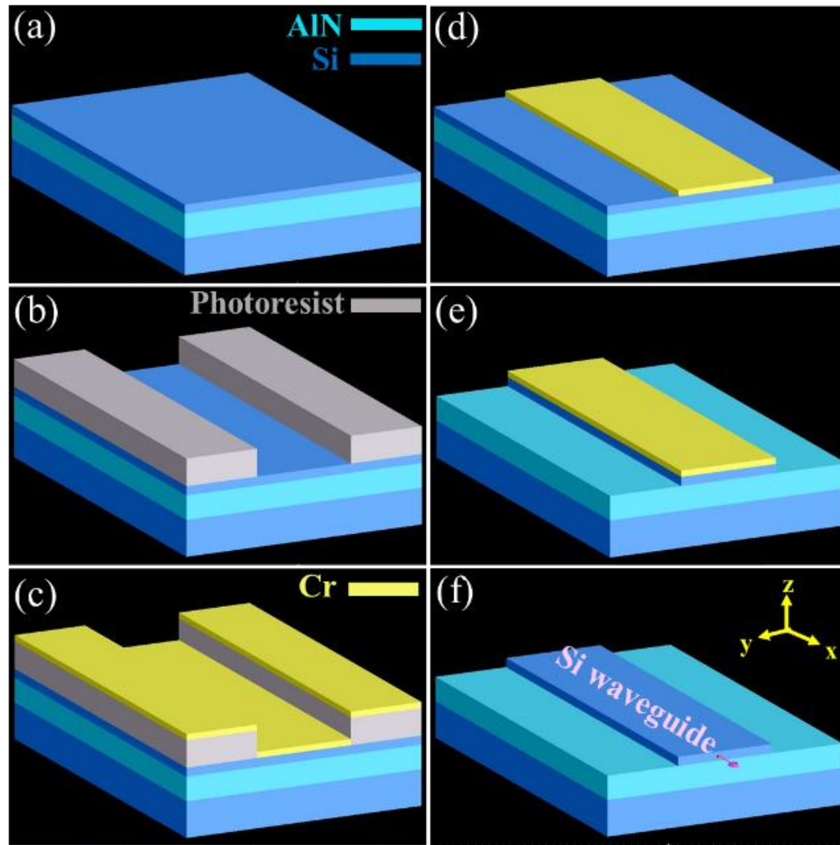

Figure 3.11 The fabrication process of a monolithic mid-IR photonic chip that consisted of a Si ridge waveguide and AlN under-cladding. (a) The AlN film was deposited on a <100> Si wafer by room temperature DC sputtering. Another a-Si thin film was then grown by PECVD. (b) - (d) Using photolithography and lift-off process, the waveguide structure was defined by Cr mask. (e) The waveguide pattern was transferred to the a-Si layer by RIE where the etching gas was SF_6. (f) The Cr mask was removed by ceric ammonium nitrate solution and followed by oxygen plasma ashing to remove the organic residue. Reprinted with permission from [69]

---

diameter Al target (99.999%). For pre-sputtering, pure argon was introduced into the chamber for 15 minutes to clean the target surface while the base pressure was set at 5×10^{-7} mTorr. Then, 10 sccm argon and 40 sccm nitrogen were injected into the chamber until the working pressure reached 10 mTorr. An optimized film deposition rate at 1 μm/hr was obtained when 1 kW DC power was applied. The distance between the Al target and the substrate was kept at 15 cm. After AlN deposition, another 1.5 μm thick a-Si film was prepared on the same substrate by the plasma-enhanced chemical vapor deposition (PECVD). The precursor gas utilized was SiH_4 and the

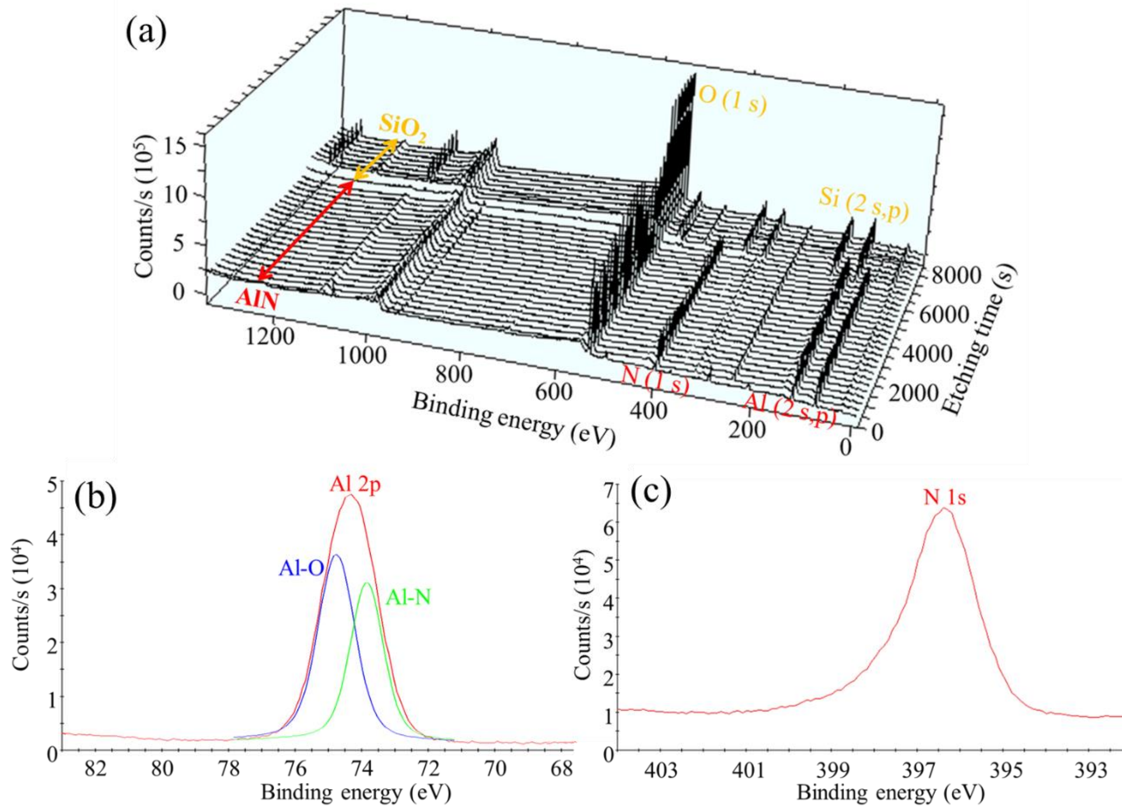

Figure 3.12 (a) XPS depth analysis of the AlN thin film. B.E. peaks at 74 eV, 119 eV, 397 eV and 532 eV were assigned to Al 2p, Al 2s, N 1s, and O 1s. The chemical composition ratio of Al:N remained constant at different layers. (b) and (c) are the high resolution XPS spectra of the Al 2p and N 1s. Al-O and Al-N signals were found after the deconvolution of Al 2p. Reprinted with permission from [69]

deposition temperature was 200 ºC. The structure of the waveguide was defined through photolithography. A 50 nm thick Cr mask was patterned on the Si-on-AlN sample by electron beam evaporation and the lift-off process followed. The waveguide structure was then transferred to the a-Si layer by the reactive ion etching (RIE). SF_6 was chosen as the etching gas because of its high etching ratio between Si and AlN. It is critical to have sharp Si waveguide facets as well as a smooth Si-AlN interface to prevent the scattering loss caused by surface roughness. In the end, the Cr mask and the organic residue on the sample surface were removed by a ceric ammonium nitrate solution and oxygen plasma ashing.

The material composition and the uniformity of the AlN thin films were characterized by XPS along the vertical direction (normal-to-plane). The spectrum of the photoelectron binding energy (B.E.) was measured at different depths when the film was etched layer-by-layer through ion sputtering. As depicted in Figure 3.12a, B.E. peaks were found at 74 eV, 119 eV, 397 eV, and 532 eV, which belonged respectively to the characteristic signals of aluminum 2p, aluminum 2s, nitrogen 1s, and oxygen 1s. High-resolution XPS spectra of the Al 2p and N 1s are drawn in Figure 3b and 3c, where Al-O and Al-N signals were revealed after the deconvolution of Al 2p peak. From Figure 3.12a, the chemical composition of the deposited AlN film was highly uniform along the vertical direction because the B.E. peak counts remained constant as the etching progressed. Meanwhile, the observed oxygen signal reveals that the deposited AlN film had Al-O bonds due to the oxygen impurity.[70, 71] Al–O formation is thermodynamically more favorable than Al–N so the alumina and the aluminum oxynitride were created even when an AlN film was grown under high vacuum or oxygen at low ppm level. A variation of XPS spectrum was observed at an etching time of 7000 s. The signals at 74V (Al 2p), 119 eV (Al 2s), and 397 eV (N 1s) dropped, while the signal at 532 eV (O 1s) increased with new B.E. peaks at 102 eV (Si 2p) and 154 eV (Si 2s) appearing. This indicates that the etching depth reached the underneath SiO_2 layer. The invariant Al : N ratio revealed the exceptional homogeneity of the microns thick AlN film that is critical to attaining low loss mid-IR devices as well as accurate waveguide sensing. A composition change will cause a deviation in the AlN refractive index that results in unwanted optical scattering.

The morphology of the fabricated devices was inspected by scanning electron microscopy (SEM). Figure 3.13a shows the top view of an 8 μm wide a-Si waveguide on AlN. It had a well-defined ridge profile without any bending or distortion found on the edge. From the cross-sectional image shown in Figure 3.13b, the waveguide facets and the side walls were sharp and absent of

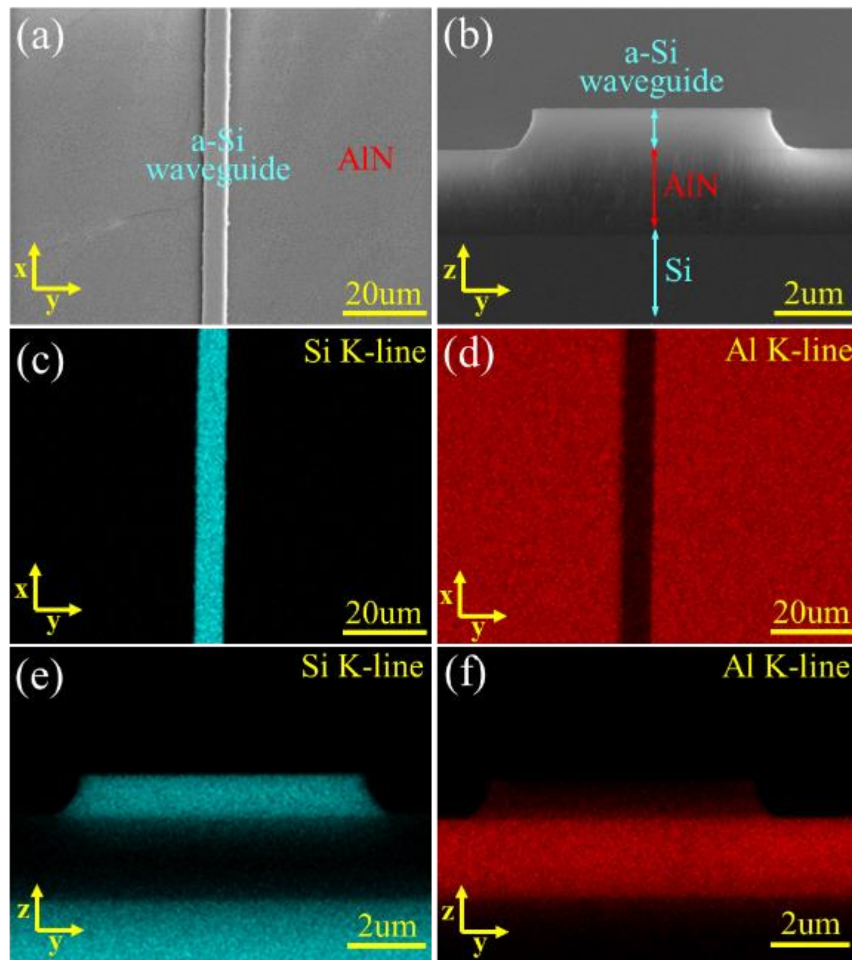

Figure 3.13 (a) The top and (b) the cross-sectional SEM images of the Si-on-AlN waveguide. (c) - (f) are the top and cross-sectional EDX images using Si Kα and Al Kα emission lines, respectively. The a-Si ridge waveguide is 1.5 µm tall and 8 µm wide, while the AlN under-cladding layer is 3 µm thick. Smooth waveguide sidewalls and a sharp interface between Si and AlN were found. Reprinted with permission from [69]

---

bumps and indentations. In addition, the clearly resolved waveguide top and the smooth interface between the Si and the under-cladding AlN layer indicated that no damage occurred during the fabrication process. The material composition of the monolithic Si-on-AlN platform was characterized by energy-dispersive X-ray spectroscopy (EDX) using the emission lines of Si Kα at 1.74 keV and Al Kα at 1.486 keV. The elemental spatial distributions of Si and Al revealed the structure profiles of the a-Si ridge waveguide and the AlN cladding layer. Figure 4c and 4d are the

EDX mapping results from the device top illustrating the a-Si waveguide and its adjacent AlN film. Meanwhile, from the cross-sectional EDX mapping shown in Figure 3.13e and f, the waveguide height and the AlN under-cladding thickness were determined to be 1.5 μm and 3 μm, respectively. The EDX images confirmed that the grown a-Si and AlN thin films have uniform compositions across the film surface as well as along the film depth.

3.3.2 Optical Property Simulation

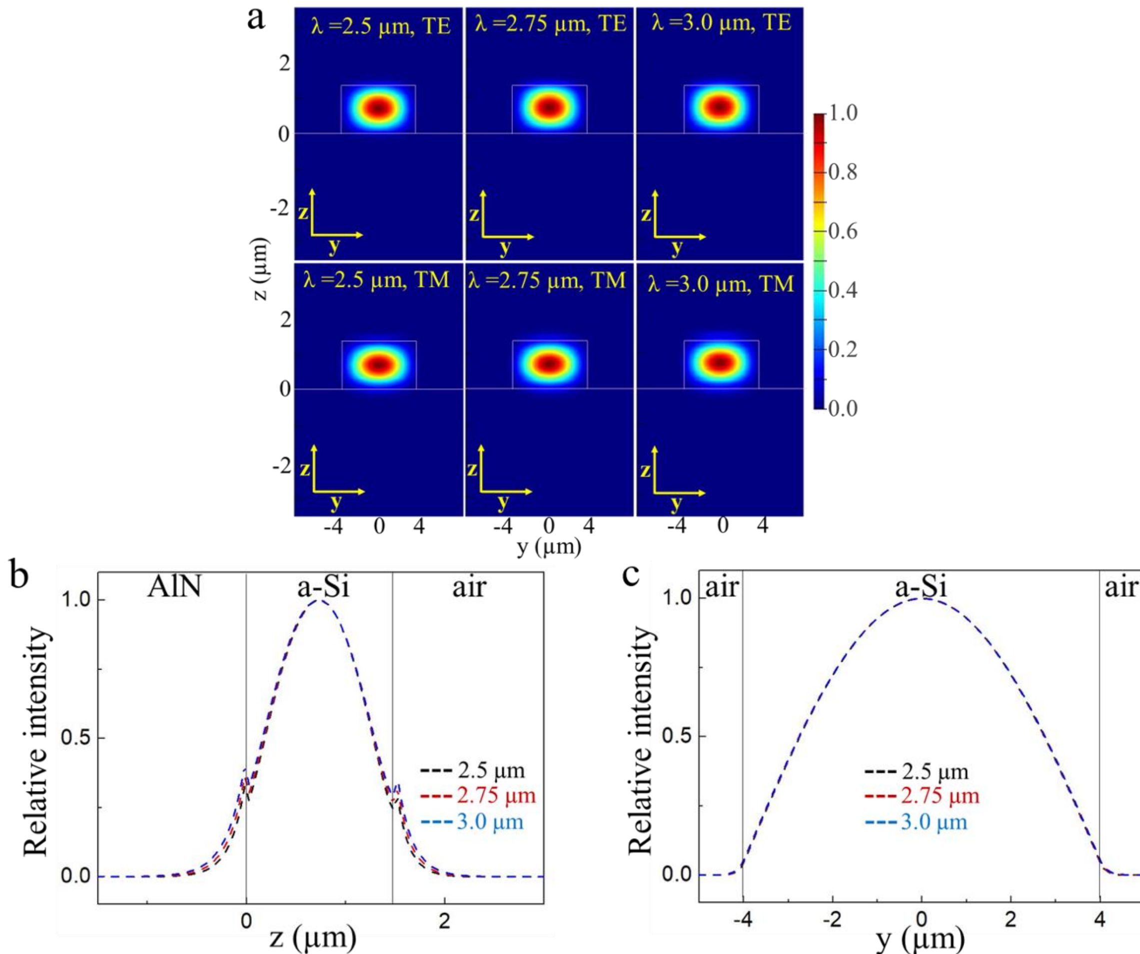

Figure 3.14 (a) The TE and TM waveguide modes calculated at λ = 2.5, 2.75, and 3.0 μm. Fundamental modes with similar ellipsoid intensity distributions were resolved in the a-Si layer in all three wavelengths. (b) and (c) are the calculated intensity profiles along the y and the z axes. Stronger evanescent fields were found along the z direction. Reprinted with permission from [69]

The waveguide modes were numerically calculated by the two-dimensional finite difference method (FDM). For waveguide sensing application, it is critical to evaluate the mode profiles since the sensitivity is determined by the interaction between the evanescent field and the molecules that approach the waveguide surface. The structure utilized in the mode simulation was obtained from the SEM characterization, where the a-Si ridge is 1.5 μm tall and 8 μm wide, and the underneath AlN layer is 3 μm thick. The refractive index of a-Si and AlN are 3.5 and 2.1. A 12 μm × 6 μm light source was chosen to excite the waveguide mode since its size is comparable to the core of the mid-IR fiber used in the experiment. Figure 3.14a draws the intensity profiles corresponding to the TE and TM waveguide modes calculated at $\lambda = 2.5$, 2.75, and 3.0 μm. Fundamental modes with similar ellipsoid intensity distribution were found in the Si layer over $\lambda = 2.5$ to $\lambda = 3.0$ μm. To better analyze the mode properties, Figure 3.14b and 3.14c display one dimensional TM polarized intensity distributions along the z- and y-axes. The TM mode expanded their optical fields extensively into the upper air ($z > 1.5$ μm) as well as the lower AlN layer ($z < 0$ μm). On the other hand, it had relatively weak evanescent fields along the y directions ($y < -4$ μm or $y > 4$ μm) since the a-Si waveguide had a high y/x aspect ratio. As the mid-IR shifted to longer wavelengths, the evanescent wave increased. Hence, the waveguide sensor will exhibit a higher sensitivity when it operates at a longer wavelength and uses TM polarization light.

3.3.3 Sensing Effect Characterization

The waveguide mode and the optical loss of the Si-on-AlN waveguides were characterized. As shown in Figure 3.15a, a fundamental mode was observed over a broad spectral range from $\lambda =$ 2.5 to $\lambda = 3.0$ μm. No scattering and distortion were observed indicating that the waveguide has flat sidewalls and a smooth interface between the a-Si and AlN under-cladding. The large

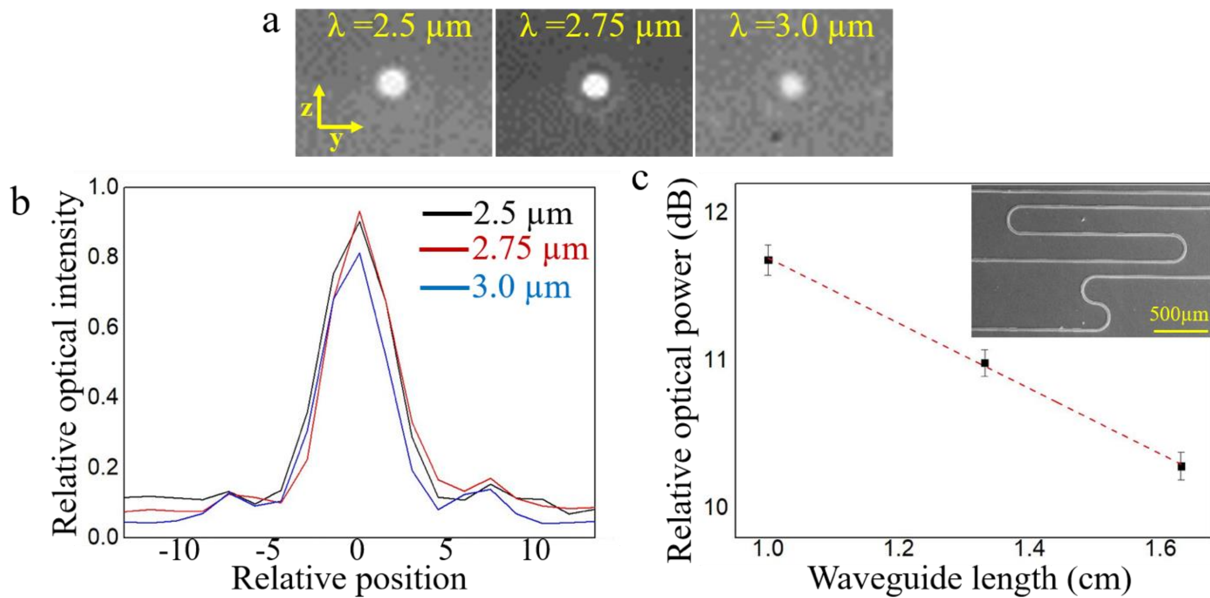

Figure 3.15 (a) The waveguide mode images captured at λ = 2.5, 2.75, and 3.0 µm. Fundamental mode is clearly observed over a broad spectral range. (b) A Gaussian profile corresponding to a fundamental mode was found at λ = 2.5 - 3.0 µm. (c) Relative optical powers measured from the waveguides with different propagation lengths. An optical loss of 2.21 dB/cm was obtained by fitting the mode intensity attenuation at λ = 2.75 µm. The inset diagram shows the paper-clip shaped waveguides that were utilized in the optical loss measurements. Reprinted with permission from [69]

refractive index difference between the a-Si and the AlN also attributed to the efficient light waveguiding. The intensity profiles of the waveguide modes were then extrapolated and illustrated in Figure 3.15b. A well resolved Gaussian profile corresponding to a fundamental mode was found between λ = 2.5 and 3.0 µm that is consistent with the calculated modes illustrated in Figure 3.14. The observed broadband fundamental mode improved the accuracy of waveguide sensing. Excitation of higher order modes will alter the mode profile and vary the intensity of the evanescent field that leads to false signals upon spectrum scanning. To evaluate the propagation loss, the optical powers measured from waveguides with different propagation lengths were recorded and displayed in Figure 3.15c. By fitting the mode intensity attenuation, an optical loss of 2.21dB/cm was obtained at λ = 2.75 µm.[72] The low optical loss mainly attributed to the high AlN transmittance,

the flat waveguide surface, and the smooth Si-AlN interface. In addition, the optical loss was effectively reduced in the mid-IR region in comparison to the NIR because the strength of Rayleigh scattering is proportional to $1/\lambda^4$.

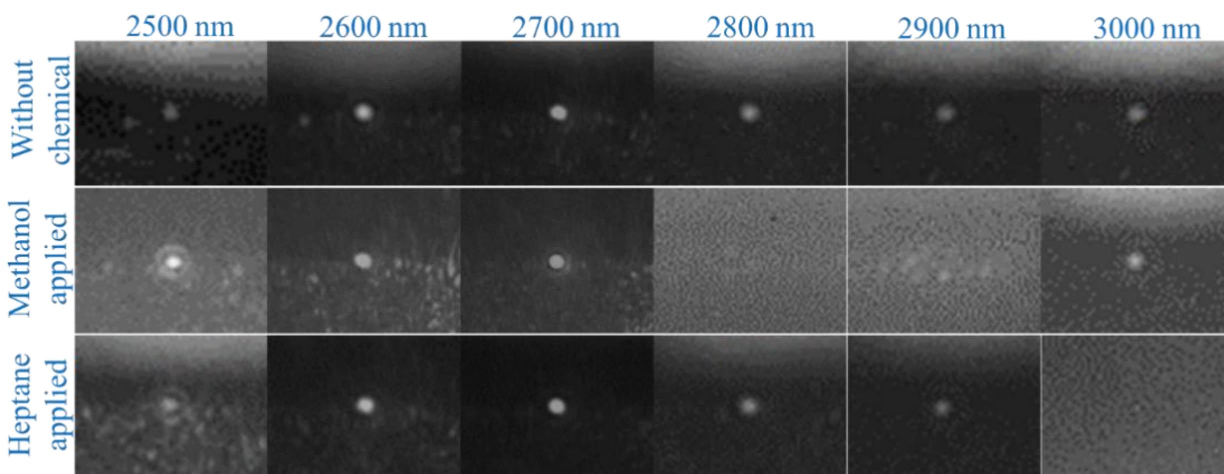

Figure 3.16 The waveguide mode images captured between $\lambda = 2.5$ and 3.0 μm. Fundamental modes were found during the spectral scanning when no chemical was on the waveguide. When heptane was applied, the mode disappeared at $\lambda = 3.0$ μm due to the -CH absorption. On the other hand, for the methanol wetted waveguide, its mode vanished at $\lambda = 2.8$ μm - 2.9 μm because of the -OH absorption. Reprinted with permission from [69]

In the waveguide sensing test, methanol and heptane were selected as the analytes to evaluate the label-free sensor performance because of their characteristic mid-IR absorptions. The probe mid-IR light was TM polarized since it carried a stronger evanescent field that attributed to a higher sensitivity. The probe light was sequentially scanned from $\lambda = 2.5$ to 3.0 μm where the spectrum regime overlapped with the -OH absorption and approached the -CH absorption. The mode images were recorded before and after dropping the chemical analytes onto the waveguide surface. As shown in Figure 3.16, without any chemicals present, a bright and sharp fundamental mode was observed from $\lambda = 2.5$ to 3.0 μm. Upon dropping the heptane on the waveguide, the mode faded at $\lambda = 3.0$ μm due to the absorption caused by the C-H stretch. On the other hand, when methanol

was applied, drastic absorption appeared at λ = 2.8 - 2.9 μm that corresponded to the absorption due to the -OH stretch. Hence, the mid-IR sensor revealed distinct spectral attenuations when exposed to different chemicals.

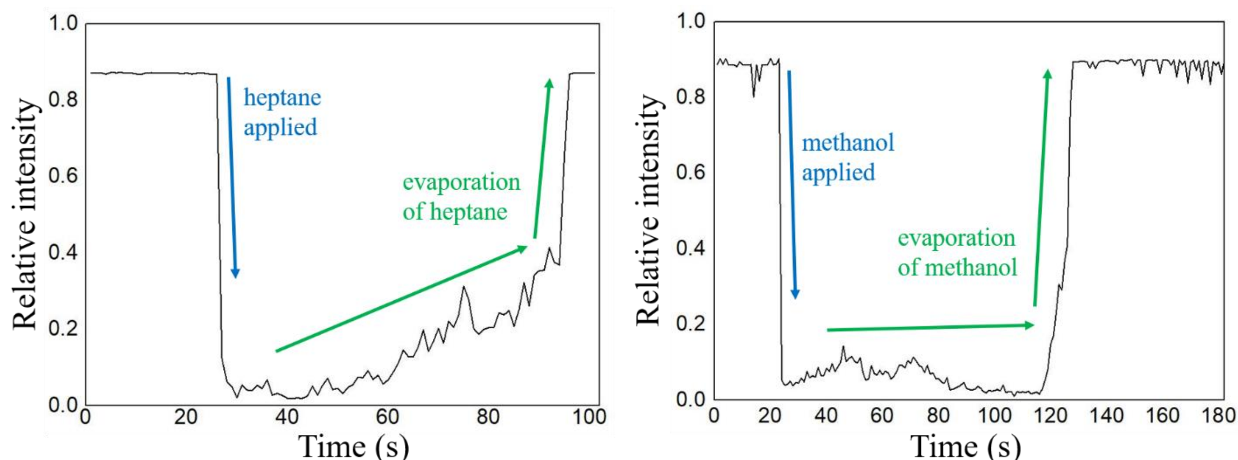

Figure 3.17 Real-time detection of (a) heptane and (b) methanol using the mid-IR waveguide sensor. The probe light wavelength was tune to λ = 3.0 and 2.8 μm to align with the -CH and -OH absorptions. The mode intensity decreased abruptly when the analytes were dropped on the waveguide surface and then recovered when the analyte evaporated. Reprinted with permission from [69]

The real-time chemical detection was carried out by monitoring the transient response of the waveguide mode. For heptane detection, the wavelength of the probe light was tuned to λ = 3.0 μm that approached C-H absorption band. As shown in Figure 3.17a, the intensity was strong before t = 27 s since no analyte was present. Upon dropping the heptane on the waveguide at t = 27 s, the mode intensity sharply decreased because the evanescent light was fully absorbed by the heptane. The optical mode intensity kept low until t = 60 s, and then gradually recovered because of the evaporation of heptane. Eventually, the intensity reached its original level at t = 92 s indicating no heptane was left on the waveguide surface. The similar transient response was observed for real-time methanol sensing shown in Figure 3.17b. In the case of tracing methanol, the light wavelength was shifted to 2.8 μm to align with the characteristic -OH absorption. At t = 20 s the mode intensity dropped that illustrated the moment methanol was added onto the

waveguide. Once it evaporated, the mode recovered to full intensity at t = 120 s. Our time-resolved characterization demonstrates that the developed mid-IR sensor is suitable for accurate in-situ monitoring of various chemicals.

3.4 Flexible Aluminum Nitride Waveguide Sensor

The study on flexible photonic devices is emerging in the past decade. Manipulation of light-wave on a flexible, conformable, or wearable substrates with functionalities of light emission, detection and signal processing is essential for frontier applications. This includes portable display and imaging, short-reach optical links, wearable photonic textiles, and strain sensing.[73 - 83] Deformable polymer substrates have initiated the development of flexible photonics due to their high mechanical flexibility. Devices like flexible displays using organic light emitting diodes (OLED)[84, 85] and organic solar cells[86] were invented. Nevertheless, micro-photonics utilizing soft materials still have challenges in thermal and chemical stabilities. In addition, organics and polymers have a strong infrared absorption that limits their application in the mid-IR regime, which is essential to implement for label-free biomedical sensing and remote health monitoring. Another technique to create flexible photonic devices is to physically transfer the layer of photonic components made of high-quality semiconductors onto the flexible substrates.[87] However, this method involves complex fabrication processes that are not practical for large-scale industrial production.

An alternate approach to achieve flexible photonics is to utilize bendable membranes, like an ultrathin borosilicate template, as the device substrate.[88, 89] It can be strongly bent without cracking or shattering since the surface strain induced by the stress is inversely proportional to the template thickness. Compared to soft materials, borosilicate is highly chemical resistant to both acid and alkaline. It also possesses strong thermal stability with a high softening point of 850 °C, as well as

a low thermal expansion coefficient of 3×10^{-6} K^{-1} at 20 °C, thus enabling its application under harsh environments. Furthermore, the borosilicate membrane has a smooth surface with an average roughness less than 1 nm. A flat surface is critical for low optical-loss photonic circuits since it prevents the energy loss caused by optical scattering.

3.4.1 Device Fabrication and Material Characterization

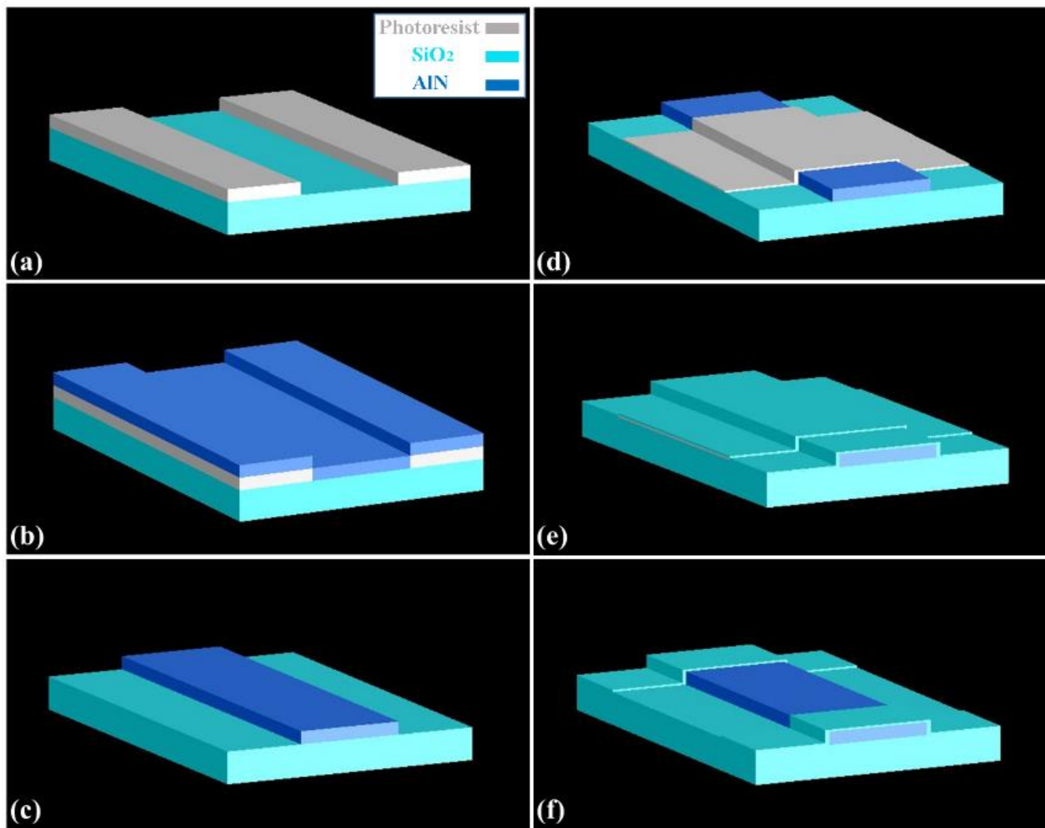

Figure 3.18. The fabrication process of the device. (a) The waveguide structure was patterned on the borosilicate template by photolithography. (b) AlN layer was deposited on the template through DC sputtering. (c) The ridge waveguide structure was developed after lift-off process. (d) Second lithography defined the sensing aperture. (e) SiO_2 was deposited as the top cladding layer. (f) Sensing aperture formed after the second lift-off process

---

The detailed fabrication process is shown in Figure 3.18. First, a negative tone photoresist was patterned on the 25 μm thick borosilicate template that defines the waveguide structure. The

developed photoresist has a negative-sloping sidewall to facilitate the later lift-off process. Next, an AlN thin film was deposited on the borosilicate template. During pre-sputtering, argon was introduced into the chamber for 30 minutes to clean the surface of the 4-inch diameter Al target (99.999%). After the pre-sputtering, 10 sccm argon and 40 sccm nitrogen were introduced into the chamber and stabilized for 5 mins. The AlN film was then deposited on the patterned borosilicate template by DC magnetron sputtering at room temperature. The DC sputtering power was 1 kW, and the working pressure was 10 mTorr. The distance between the Al target and the borosilicate template was 15 cm where an optimized deposition rate of 1 μm/hour was obtained. In the lift-off process, the remaining photoresist and the AlN on it were removed by acetone. As a result, the 2 μm high AlN ridge waveguides was left on the template. Finally, the SiO_2 was deposited by RF sputtering a 3-inch diameter Si (99.99%) target. The sputtering power and working pressure were 500W and 3 mTorr, respectively. Argon and oxygen were introduced into the chamber in a 10:1

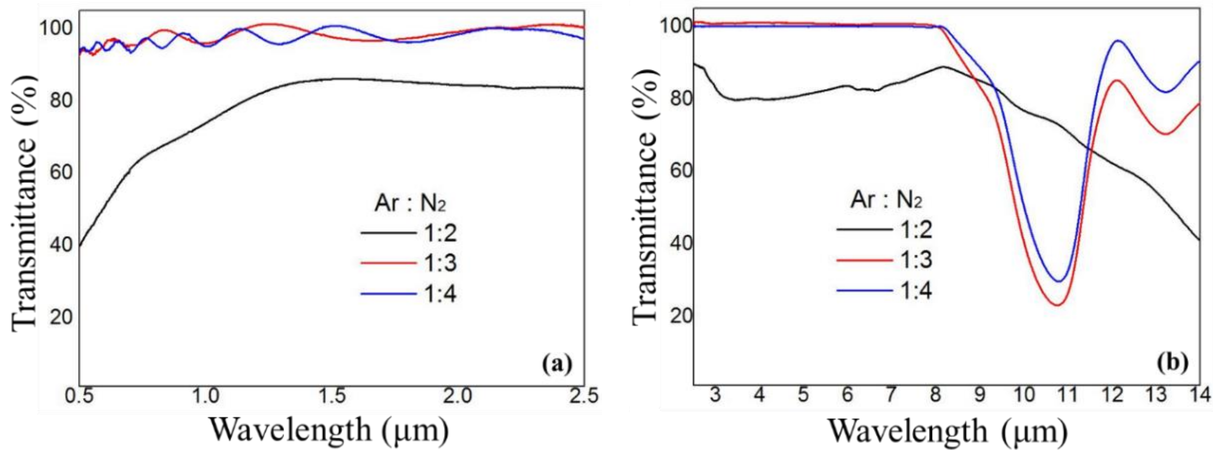

Figure 3.19 (a) Vis-NIR and (b) ATR-FTIR spectra of the AlN films prepared by DC sputtering at different Ar : N_2 ratios. The AlN film is transparent up to $\lambda = 9$ μm when the Ar:N_2 ratio reaches 1:3.

ratio, and a 250 nm thick SiO_2 film was obtained after 30 minutes deposition. Eventually, a thin SiO_2 top-cladding layer with an open aperture in the waveguide center was created.

AlN films deposited at different N_2/Ar ratios were characterized by a Vis-NIR spectrometer and ATR - FTIR. As shown in Figure 3.19a and b, the film prepared at N_2/Ar = 2:1 was not transparent in the visible or the infrared regions, which was due to the unreacted Al metal residues in the AlN film. On the other hand, two AlN films that were prepared at higher N_2/Ar ratios were fully transparent from **λ** = 0.5 to 9 µm because all the sputtered Al atoms were reacted with nitrogen molecules and no metallic Al was left in the film. After wavelength **λ** = 9 µm, a strong absorption at **λ** = 10.7 µm and a minor absorption at **λ** = 13.3 µm were observed which were due to the Al-N

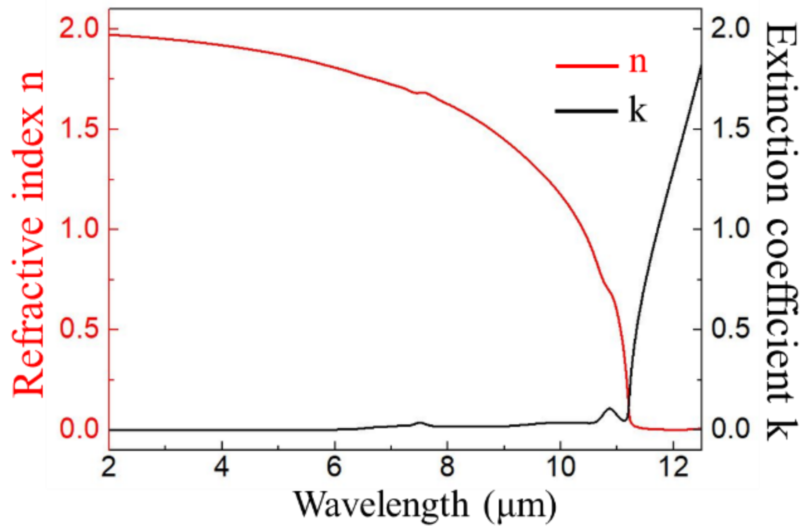

Figure 3.20 The **n** and **k** plots of the AlN thin film from IR-VASE measurement. The refractive index **n** has low dispersion up to λ = 9 µm, and negligible absorption is found before λ = 10 µm. The increase of **k** after λ = 9 µm is due to the absorption of the Al-N bond.

bond. The **λ** = 10.7 µm absorption corresponded to the longitudinal optical mode while the other at **λ** = 13.3 µm was due to the transverse optical (T_0) E1 mode.[9091] The optical quality including transparency of our AlN film is comparable to others prepared by high temperature sputtering.[92] In addition, the membran e cladding is transparent up to 6.5 um from ATR-FTIR measurement. Thus, both the AlN waveguide core and the membrane cladding are widely transparent to form the low-loss waveguide. Meanwhile, the AlN film prepared at N_2/Ar = 1:3 has fewer interference fringes than the film with a ratio of 1:4. This revealed that lower N_2/Ar sputtering leads to a higher

AlN growth rate since the interference pattern from a thinner film has a faster spectral intensity variation.[93] Hence, our waveguide sensor utilized the AlN film prepared at N_2/Ar = 1:3 due to its

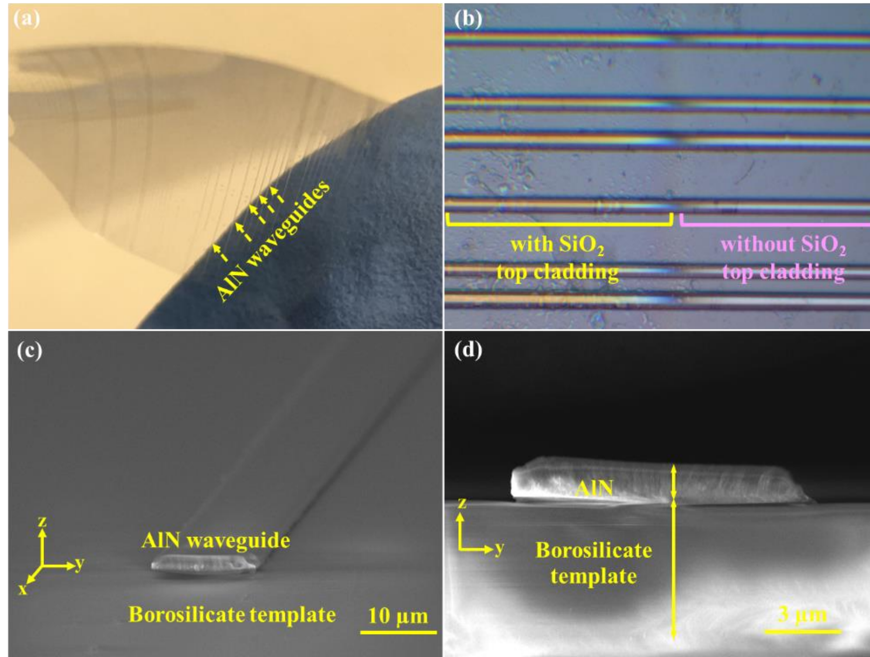

Figure 3.21. (a) The fabricated AlN-on-borosilicate flexible waveguides. The waveguide array is indicated by the yellow arrows. (b) The magnified optical image of the AlN waveguide array. Only the left portion of the waveguides is covered by SiO_2 top cladding. The right portion remains open to the surrounding for sensing application. The (c) top and (d) cross-sectional SEM images of a 2 μm x 10 μm AlN-on-borosilicate waveguide. Smooth waveguide surfaces and a sharp interface between the waveguide and the borosilicate template are clearly resolved.

---

high mid-IR transparency and sufficient thickness to effectively confine the long wavelength mid-IR light.

The optical constants of the deposited AlN, including its index of refraction **n** and extinction coefficient (imaginary refractive index) **k**, was further characterized by IR-VASE, a technique that measures and analyzes the polarization change from the reflected mid-IR light. The **n** and **k** characterization was carried out between λ = 2 μm and 13 μm. As shown in Figure 3.20, the **n** decreases slowly from 1.9 at λ = 2 μm to 1.6 at λ = 9 μm until a strong dispersion found after λ = 10 μm. The small variation of **n** over a broad mid-IR spectral range offers the advantage of low

optical dispersion required for many mid-IR devices, including efficient nonlinear light generation and accurate chip-scale chemical sensing. Another merit is the relatively low extinction coefficient **k** observed before λ = 10 μm showing its potential for broadband mid-IR photonic circuits. The increase of **k** after λ = 10 μm is due to the Al-N stretching absorption and the result agrees well with the ATR-FTIR characterization shown in Figure 3.19a.

The fabricated AlN-on-borosilicate flexible waveguides are shown in Figure 3.21. No delamination or broken segments were found while bending the device, indicating the deposited AlN waveguides firmly adhered to the borosilicate template and able to tolerate high mechanical stress. Figure 3.21b is the magnified optical image of the AlN waveguide array. The left side of the device is covered by a thin SiO_2 cladding layer that anchors the AlN waveguides onto the borosilicate template, and consequently prevents the waveguides from peeling off upon mechanical bending or stretching. In contrast, the right side of the device remains open to its surroundings for sensing application. The structure detail of the waveguides was further inspected by SEM. Figure 3.21c and d display the top and the cross-sectional SEM image of a 10 μm wide and 2 μm high AlN waveguide. It has a well-defined ridge structure without bends or distortions found on the edge, nor cracks or indents on the surface. The sharp waveguide edges reduce the waveguide propagation loss caused by light scattering, which is critical to perform accurate waveguide sensing. In addition, the interface between the top AlN waveguide and the under-cladding borosilicate template is well-resolved. No depletion damage was found on the device surfaces or the interface since the AlN waveguides were prepared by the lift-off process instead of applying an aggressive etching process.

The structural detail and the material composition of the waveguides were then characterized by the EDX using the emission lines of Al Kα at 1.49 keV, N Kα at 0.392 keV, Si Kα at 1.74 keV,

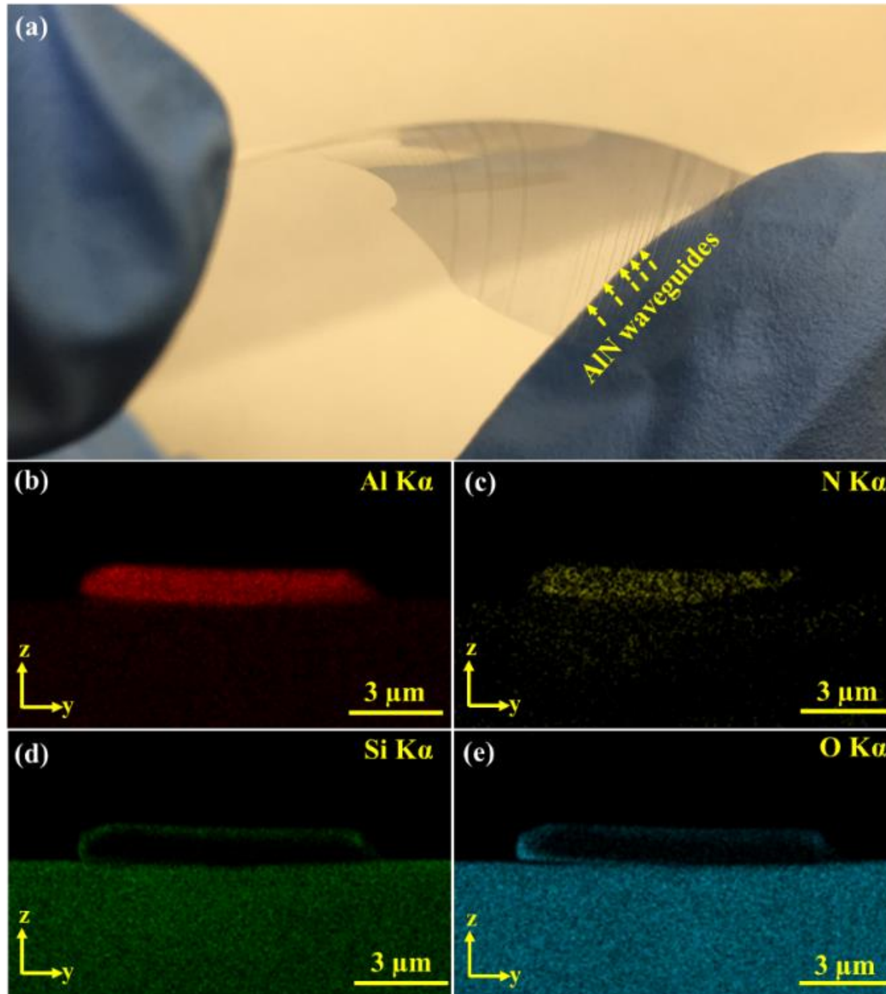

Figure 3.22 (a) The fabricated AlN-on-borosilicate flexible photonics. The array of AlN waveguides are highlighted by the yellow arrows. The cross-sectional EDX mapping analysis using (b) Al Kα and (c) N Kα lines to identify the AlN waveguide, while (d) Si Kα and (e) O Kα lines correspond to borosilicate membrane and the SiO_2 top cladding.

---

and O Kα at 0.525 keV. Figure 3.22b - e display the cross-sectional EDX mapping of a 10 μm wide and 2 μm height AlN waveguide with a 200 nm SiO_2 top cladding. The Si and O elemental distributions corresponded to the layer of the SiO_2 and the borosilicate membrane, while the Al and N distributions corresponded to the AlN waveguide. From the mapping analysis, the ridge structure and the interface between the AlN waveguide and the borosilicate template are clearly resolved. Moreover, the deposited AlN film has a homogeneous compositional distribution. The

obtained material uniformity reduced unwanted optical scattering loss caused by the variation of refractive indexes.

3.4.2 Optical Property Simulation

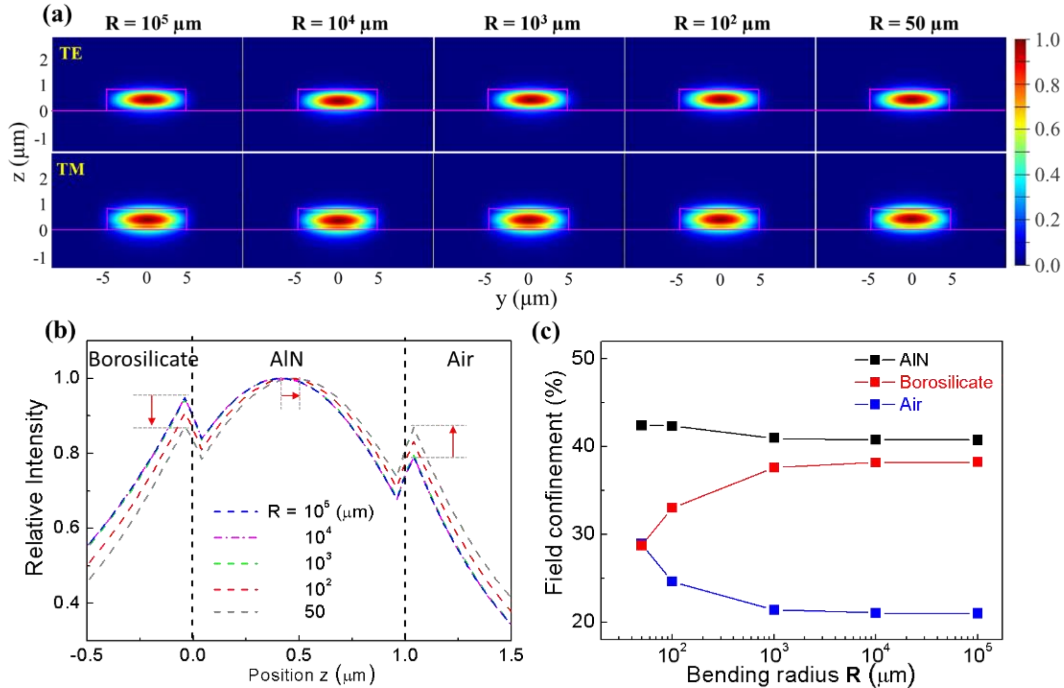

Figure 3.23 (a) The FEM calculated waveguide modes of a 1 µm tall AlN-on-borosilicate waveguide at various bending radii R. The first and second rows represent the TE and the TM polarized modes, respectively. The wavelength is at λ = 2.5 µm. TM mode shifted toward the air as the bending deformation was applied. (b) The intensity distribution along the z-axis for the TM polarized modes when the bending deformation increased from **R** = 10^5 to 50 µm. Evanescent field in the borosilicate template decreased while the other field in air region raised. (c) The TM optical field confinement inside the AlN waveguide, the upper air region, and the lower borosilicate cladding. Though the evanescent fields varied at different R, the field guided in the AlN remained almost the same.

The bending effect on the waveguide performance was evaluated by the two-dimensional finite element method (FEM) calculation. Figure 3.23a displays the modes of a 1 µm thin AlN waveguide when the flexible device was warped at different bending radius of **R** = 105, 104, 103, 102, and 50 µm, respectively. A stronger bending strain caused a physical curvature creating a smaller

bending radius. For TE polarization, the fundamental mode revealed the same ellipsoid profile when the radius R changed considerably from **R** = 105 to 50 μm. This indicates the structure deformation introduced by the mechanical bending had a negligible impact on the waveguide property since the majority of the optical field was still confined inside the high index AlN layer. On the other hand, for TM polarization, the mode slightly shifted toward the air when the bending deformation was applied. As the result, the evanescent field in the upper air region increased while the field in the lower borosilicate template decreased. Figure 3.23b illustrates the TE polarized optical fields calculated at different radius **R**, where redistribution of the mode intensity was clearly observed. The evanescent field within the bottom template dropped by 10 %, while the other field in the upper air region raised by 12 % as the mechanical bending was applied. Meanwhile, the center of the mode moved toward the lower refractive index air by 70 nm. Figure 3.23c plots the optical field confinement factors inside the AlN waveguide, the top air, and the lower borosilicate cladding layer. Though these evanescent fields varied with different bending deformation, the wave confined inside the AlN layer remained close at 41 %. This indicates our flexible AlN membrane waveguide can tolerate high structure deformation. As a result, the sensor is capable of adopting different device configurations, which is a critical feature for application of small-footprint wearables.

The waveguide sensing performance was numerically studied by the two-dimensional finite element method (FEM). The optical modes of the AlN waveguide were calculated when it is exposed to a mid-IR absorptive chemical. The structure parameters utilized in the modeling were obtained from the SEM images shown in Figure 3.21, where the ridge waveguide is 2 μm high and 10 μm wide, and the refractive index of AlN and borosilicate are 1.97 and 1.46, respectively. To excite a waveguide mode, a 12 μm × 6 μm light source was chosen because its size is comparable

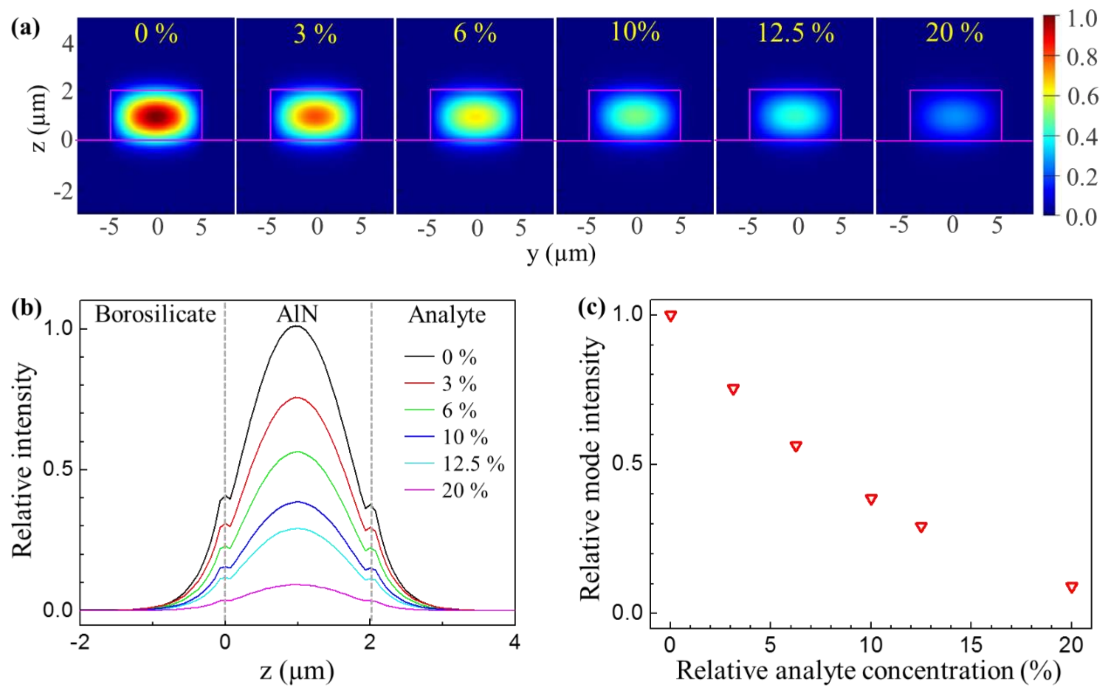

Figure 3.24 (a) The calculated mode images of an AlN-on-borosilicate waveguide when it is exposed to an analyte containing a mid-IR absorptive chemical. The concentrations of 0 %, 3 %, 6 %, 10 %, 12.5 %, and 20 %, were utilized in the modeling. The waveguide mode gradually vanishes when the concentration increases. (b) The mode intensity profiles along the z-axis at y = 0 μm. Both the guided light (0 μm < z < 2 μm) and the evanescent field decrease when the chemical concentration raises. (c) The plot of waveguide mode intensity vs. analyte concentration. The relative mode intensity drops from 1 to 0.1 as the concentration increases from 0 % to 20 %.

---

to the 9 μm core diameter of the mid-IR fiber used in the experiment. The light source wavelength was adjusted to λ = 2.65 μm to align with the characteristic O-H absorption. TM polarization was utilized because the AlN ridge waveguide has a large y:z aspect ratio of 5:1 that created a strong evanescent field along the z-direction. A strong evanescent field is essential to achieve high sensitivity because the sensitivity is determined by the interaction strength between the field and the molecules approaching the waveguide surface. Figure 3.24a displays the calculated mode images when the waveguide surrounded by analytes with different concentration of a mid-IR absorptive chemical. Here the extinction coefficient **k** of the analyte is proportional to the chemical

concentration. A fundamental mode with ellipsoid intensity distribution is found inside the AlN waveguide, and its evanescent field extends into both the surrounded chemicals ($z > 2$ μm) and the borosilicate layer ($z < 0$ μm). The waveguide mode faded quickly as the chemical concentration increases because the evanescent wave was considerably absorbed by the chemical moving close to the waveguide. To better analyze the variation of the waveguide modes when mid-IR absorption raises, Figure 3.24b display the intensity profiles of the TM polarization modes along the z-axis as the concentration changes. The intensities of the guided wave ($0 < z < 2$ μm) and the evanescent wave ($z > 2$ μm and $z < 0$ μm) both decreases drastically when the concentration of the absorptive chemical increases. Yet, the waveguide mode remains the fundamental mode regardless of the concentration. The invariance of the mode profile is critical to achieving accurate waveguide sensing, since an excitation of higher order modes will alter the mode profile and also vary the evanescent field that consequently will lead to false signals during the sensing measurements. Figure 3.24c plots the waveguide mode intensity when the analyte concentration gradually increases from 0 % to 20 %. The mode intensity decreases monotonically with the increases of the chemical concentration. The results indicate our mid-IR waveguide is capable of performing accurate concentration analysis by measuring the attenuation of the waveguide mode intensity.

3.4.3 Sensing Effect Characterization

The waveguide mode and the optical loss of the AlN flexible waveguides were experimentally characterized. As shown in Figure 3.25a, a fundamental mode was clearly observed over a spectral range from $\lambda = 2.5$ to 2.7 μm. The mode profiles remained the same at different wavelengths, while no scattering or distortion was observed. These results indicate that the waveguide has a flat sidewall, and the interface between the AlN and the under-cladding template is smooth. The high

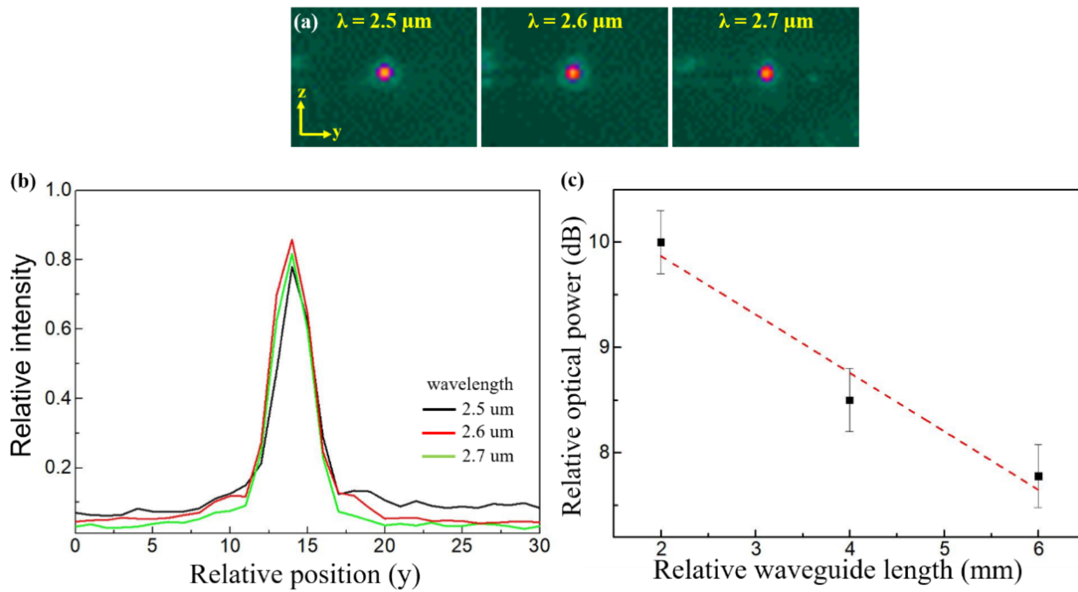

Figure 3.25 (a) The waveguide mode images captured at **λ** = 2.5, 2.6, and 2.7 µm. A fundamental mode was observed. (b) The y-direction intensity profiles extrapolated from the waveguide mode. It remains Gaussian profile as the wavelength changes. (c) Relative optical powers measured from the waveguides with different lengths. The optical loss was obtained by fitting the power attenuation at **λ** = 2.5 µm.

---

refractive index difference between the AlN and the borosilicate is also attributed to the efficient confinement of the mid-IR lightwave inside the waveguide. The intensity profiles of the waveguide modes were then extrapolated and illustrated in Figure 3.25b. A well resolved Gaussian profile corresponding to a fundamental mode was found from **λ** = 2.5 to 2.7 µm, and this result was consistent with the simulated mode profiles displayed in Figure 3.24. The invariant shape of the mode over a broad spectrum indicates that the AlN waveguide has a low optical dispersion, which is necessary to achieve wideband optical communication. Meanwhile, the preservation of the fundamental mode over such a wide spectral range is critical for accurate waveguide sensing. An excitation of higher order modes will alter the mode profiles and vary the intensities of evanescent fields, which will lead to false signals upon spectrum scanning. To determine the propagation loss, the optical powers from waveguides of different lengths were measured and displayed in Figure

3.25c. By fitting the mode intensity attenuation, an optical loss of 5.5 dB/cm was obtained at λ = 2.5 µm, which is much lower than the previous studies showing 10 dB/cm in the visible region at λ = 0.63 µm. The low optical loss of our flexible AlN waveguide contributes to its smooth waveguide surface as well as the sharp interface between the AlN and the borosilicate template. In addition, the scattering loss in the mid-IR region is significantly lower than the loss in the shorter wavelength Vis-NIR because the scattering strength is proportional to $1/\lambda^4$.

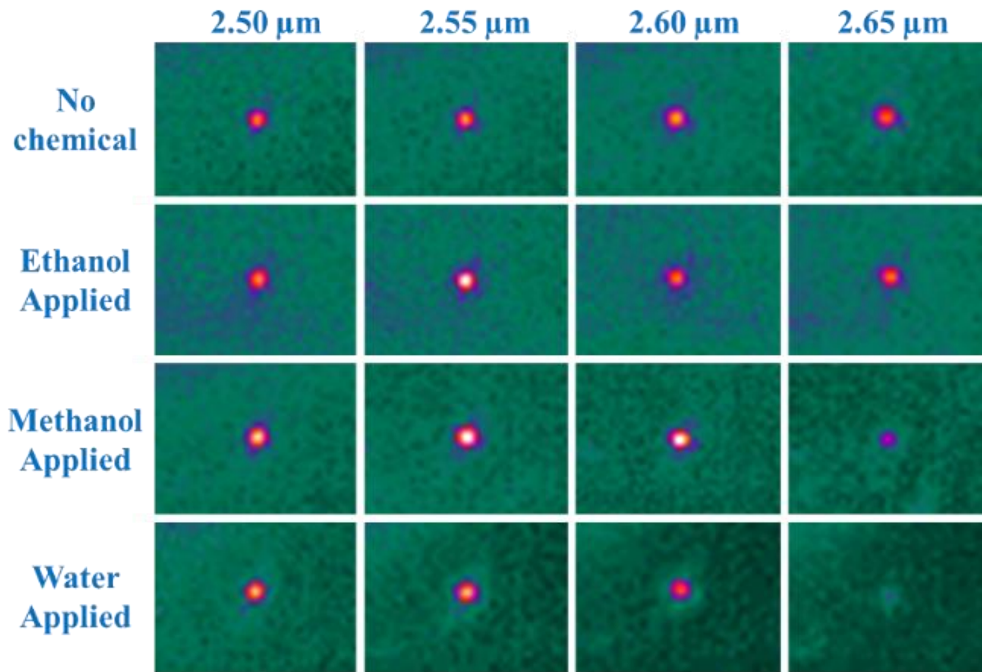

Figure 3.26 The waveguide mode images captured between λ = 2.50 and 2.65 µm when it was covered by different chemicals, including ethanol, methanol, and water. During the spectrum scan the mode showed dissimilar intensity attenuation when different chemicals applied. The absorption of water raised at λ = 2.60 µm and the mode vanished at λ = 2.65 µm. For methanol wetted waveguide the mode became dim until λ = 2.65 µm. On the other hand, the mode of ethanol wetted waveguide remains bright indicates ethanol is transparent at λ = 2.50 - 2.65 µm. The results demonstrate the mid-IR waveguide sensor can differentiate chemicals through spectrum scanning.

To experimentally evaluate the sensing performance of the AlN flexible waveguides, chemicals containing alkoxy group and water were selected as analytes because of their strong O-H characteristic absorption between λ = 2.6 and 3.3 µm. TM mode light was utilized due to its

stronger evanescent field that attributes to a higher sensitivity. The wavelength of the probe light was sequentially scanned between λ = 2.50 and 2.65 μm, where the O-H absorption rose and the AlN waveguide was transparent. The waveguide mode images were recorded before and after dropping the analytes onto the waveguide surface. As shown in Figure 3.26, without any chemicals present, a bright, sharp fundamental mode was observed from λ = 2.50 to 2.65 μm. The mode profiles remain the same at different wavelengths without scattering. No distortion found in the captured mode images indicates that the waveguides have flat sidewalls and a smooth interface between the AlN and borosilicate layer. The high refractive indexes difference of the AlN and the borosilicate also attribute to the observed efficient guiding of the mid-IR lightwave. The invariant shape of the mode over such broad spectrum indicates that the waveguide has low dispersion in this region, which also agrees well with the optical constants characteristics displayed in figure 3.20. When dropping various analytes onto the waveguide, the light modes revealed dissimilar spectral intensity variations for different chemicals. For ethanol wetted waveguide, the mode became a lighter spot at λ = 2.55 μm and its intensity remained bright up to λ = 2.65 μm. The increase of mode intensity was due to the formation of a top cladding layer made by the dropped ethanol. On the other hand, for the methanol wetted waveguide, the mode intensity decreased instantaneously at the longer wavelength λ = 2.65 μm. As for water, the mode intensity diminished as the light shifted to longer wavelengths and no waveguide mode was found beyond λ = 2.65 μm. The strong intensity attenuation observed corresponds to the characteristic O-H absorption of water. Thus, we show that our mid-IR waveguide sensor is capable of differentiating water, ethanol, and methanol since they reveal different mid-IR absorption patterns. At λ = 2.65 μm, the ethanol is transparent, methanol is partially transparent, and water was fully opaque. Our results consist

with previous FTIR measurements where the O-H absorption from water rises up at the shorter mid-IR regime comparing to that of ethanol and methanol.

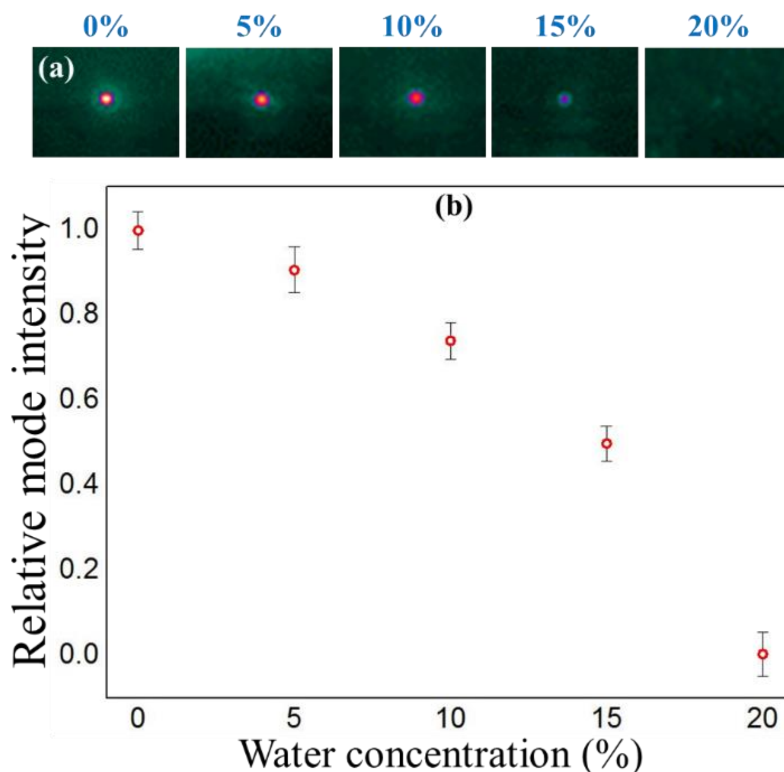

Figure 3.27 The (a) images and (b) mode intensities of the AlN waveguide modes when the waveguide exposed to ethanol/water mixtures at different concentrations. The probe light wavelength is at λ = 2.65 μm, where water is opaque and ethanol is transparent. The waveguide mode intensity decreases rapidly as the water concentration increases.

The quantitative chemical analysis was conducted by testing water/ethanol mixtures with various concentrations at 0 %, 5 %, 10 %, 15 %, and 20 %, respectively. A probe light at λ = 2.65 μm was chosen since ethanol is transparent at that wavelength, while water is highly absorptive. As shown in Figure 3.27a, the waveguide mode vanished abruptly as the water concentration increased from 0 % to 15 %, and the mode eventually disappeared at 20 % concentration. To better quantify the variation of the waveguide mode as the water concentration changes, Figure 3.27b plots the mode intensities measured at different water/ethanol concentrations. A 30 % intensity attenuation was found for a 10 % water solution. Once the concentration reached 20 %, all the

light was absorbed, which exhibited a similar trend with the simulation results. Thus, we demonstrate that our flexible waveguide can perform quantitative label-free detection utilizing the characteristic mid-IR absorption.

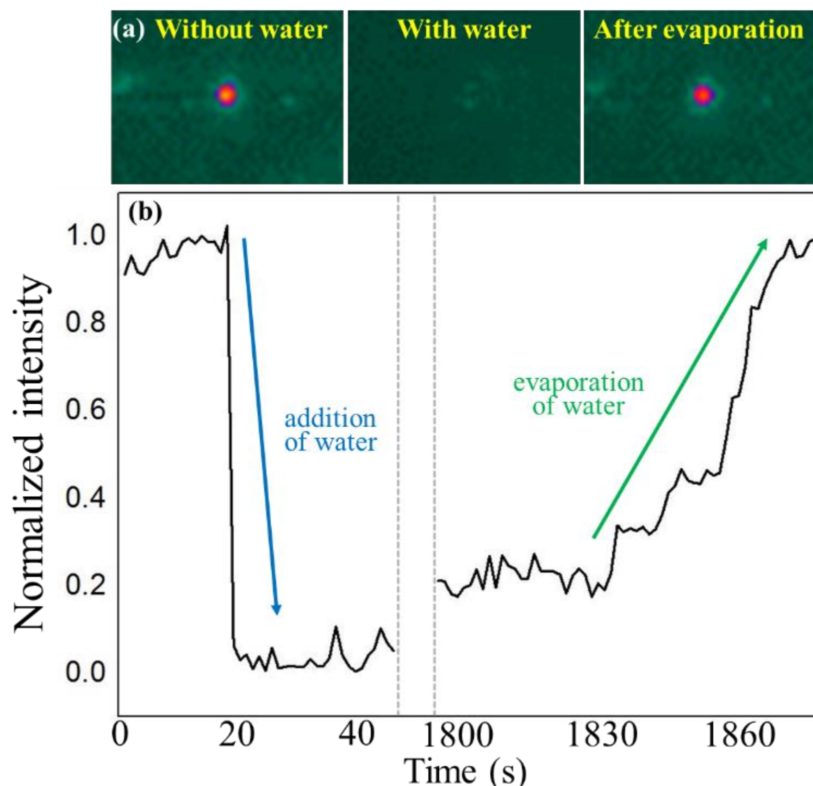

Figure 3.28 The (a) mode images and (b) transient response for real-time chemical detection using the AlN-on-borosilicate waveguide. The analyte is water and the probe light wavelength is λ = 2.65 μm to align with the water –OH absorption. The mode intensity decreased instantaneously when the water was dropped on the waveguide surface and then recovered when the water evaporated.

A real-time chemical detection was performed by monitoring the transient response of the waveguide when it was exposed to analytes. Figure 3.28a shows the waveguide mode images before and after dropping water onto the waveguide sensor, and its intensity variation is plotted in Figure 3.28b. The probe wavelength was tuned to λ = 2.65 μm to align with the water absorption band. Before t = 20 s, the mode intensity was strong since there was no presence of the analyte. When the water wetted the waveguide surface at t = 20 s, the intensity decreased instantaneously

and the mode disappeared because the waveguide light was fully absorbed by the water that covered the waveguide surface. After t = 1830 s, the light intensity gradually recovered since most of the water on the waveguide evaporated and only a thin layer of water was left. The mode intensity ultimately reached its original level once no more water molecules remained on the waveguide surface. The time-resolved characterization demonstrates that the mid-IR sensor waveguide is suitable for in-situ and label-free monitoring of various chemical species. In addition, it is not only capable of accurate sensing, but it is also reusable.

CHAPTER IV

MID-INFRARED ELECTRO-OPTICAL MODULATORS

This chapter introduces mid-IR phase polarization modulators developed on LN and BTO. Three different waveguide modulators are proposed: *i.* TiO_2-on-BTO modulator; *ii.* Top-bonded BTO modulator; *iii.* flexible AlN waveguide sensor. The detailed device design and fabrication process are introduced. Further, the device optical property and electro-optical effect are evaluated.

4.1 Measurement System Set-up

The waveguide optical property and the electro-optical reconfigurability of the fabricated devices were characterized by a testing station shown in Figure 4.1. The light source was a pulsed laser with a wavelength tunable from $\lambda = 2.4$ to 3.8 μm and a linewidth of 3 cm^{-1}. It had a 150 kHz pulse repetition rate, 10 nanoseconds pulse duration, and 150 mW average power. The probe laser

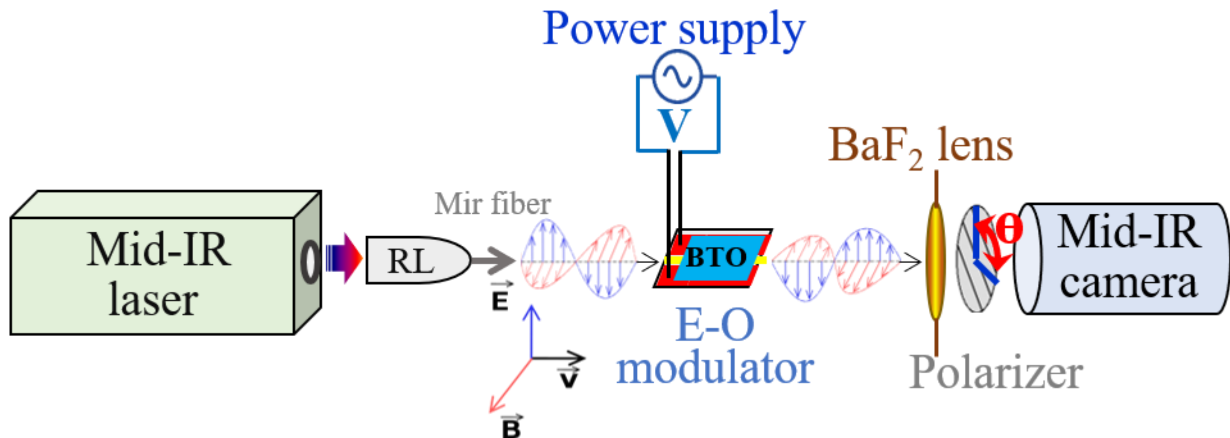

Figure 4.1 The experimental set-up to test the electro-optical modulation of the ToL waveguide. Light from mid-IR laser was coupled into a fiber through the reflective lens (RL) and then into the ToL waveguide through butt-coupling technique. The electrodes were connected to a DC power supply and created the electric field E across the waveguide. The waveguide mode and intensity were recorded by a mid-IR camera. A polarizer with polarization angle θ was placed between the BaF_2 lens and the camera.

light was first focused into a 9 μm core fluoride fiber using a reflective lens, and then butt-coupled into the waveguide. The fine alignment between the optical fiber and the waveguide was monitored by an upper microscope equipped with a long working distance 10x objective lens. The light emitted from the waveguide back facet was focused by a BaF_2 biconvex lens with 25 mm focal length and then captured by a liquid nitrogen cooled 640 x 512 pixel InSb camera. A polarizer was placed before the camera, selecting the polarization of the recorded light signal. Meanwhile, an electric field E was applied across the ToL waveguide using the pair of Ti electrodes that were loaded on the two sides of the TiO_2 ridge. The electrodes were connected with a DC power supply through two micro-manipulators. E was determined by the applied voltage, V, of the power supply and the gap width, g, between the pair of electrodes. The waveguide mode intensity was then recorded when the V was swept between 0 and 100 V.

4.2 Titanium Dioxide on Lithium Niobate Polarization Modulator

LN is a widely used material to achieve reconfigurable mid-IR photonics, which is a ferroelectric and high nonlinear optical crystal.[94, 95] First, LN is transparent up to $\lambda > 5$ μm with a moderate refractive index, $n = 2.18$,[96] which grants it versatile roles either as a waveguide cladding or a waveguide core in the mid-IR regime.[97, 98] Second, LN has a high electro-optical coefficient and a large second-order optical nonlinearity (χ^2) so it enables efficient nonlinear light generation and electro-optical light modulation. [99, 100] Previous studies have shown an LN switch in Near-Infrared (NIR) with a modulation speed exceeding 100 GHz [101] and a low $V_\pi \cdot L$ of ~10 Vcm, [102] where $V_\pi \cdot L$ is the product of the voltage and the device length to create a π phase difference. In addition, both phase and intensity LN modulators can achieve a high extinction ratio > 15 dB,

which is significantly better than present Si-based photonic devices.[103] Therefore, LN is an ideal platform for tunable mid-IR photonic circuits.

4.2.1 Device Fabrication and Materials Characterization

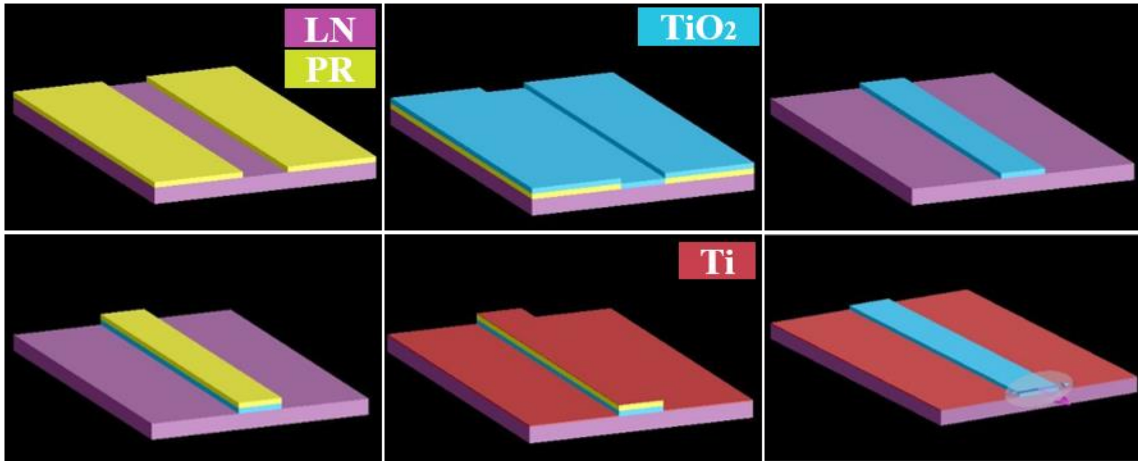

Figure 4.2 Schematic of the TiO_2-on-LN waveguide fabrication process. The waveguide structure was defined by photoresist (PR) on the LN substrate through photolithography, following TiO_2 thin film deposition by reactive RF sputtering. The TiO_2 ridge waveguide structure was developed on the LN substrate after lift-off. Ti electrodes were loaded on both sides of the waveguide through the same fabrication process.

The detailed device fabrication process is shown in Figure 4.2. First, a negative tone photoresist was patterned on an LN wafer, which defined the waveguide structure. After development, the photoresist had undercut sidewall that will facilitate the lift-off process. Next, a 0.8 μm thick TiO_2 film was deposited on the patterned substrate by room temperature RF sputtering. The target was Ti (99.999%) and the gases introduced into the deposition chamber were 36 sccm argon and 4 sccm oxygen. After TiO_2 deposition, the photoresist and the TiO_2 above were removed by acetone and only the TiO_2 ridge waveguide was left on the LN substrate. Applying the same lithography and lift-off steps, 100 nm thick Ti electrodes were deposited on

both sides of the TiO_2 waveguide. The ToL fabrication avoided delicate and costly processes including ion slicing and wafer bonding utilized in prior LN thin film devices. [104,105]

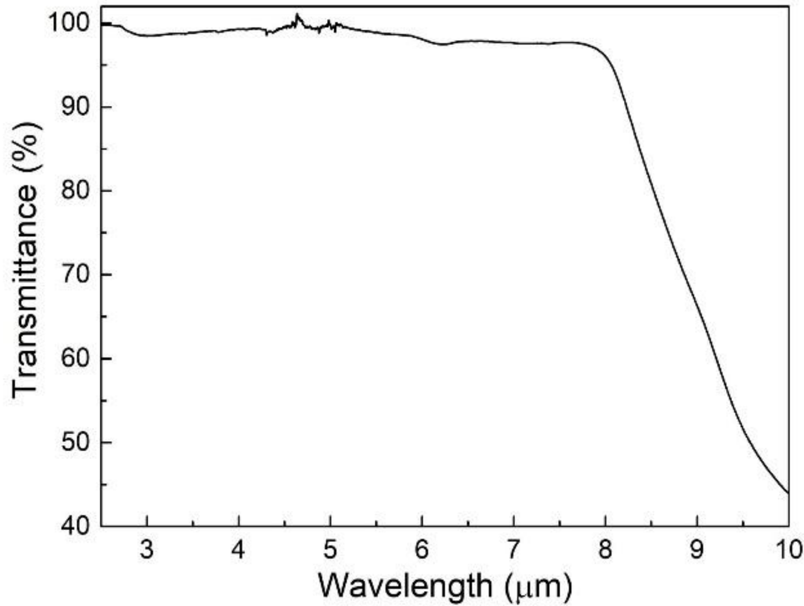

Figure 4.3 The transmission spectrum of deposited TiO_2 from ATR-FTIR measurement, showing a broad transmittance up to $\lambda = 8$ μm.

The optical property of deposited TiO_2 thin film was characterized by attenuated total reflection - Fourier transform infrared spectroscopy (ATR-FTIR) and the result is displayed in Figure 4.3. High transmittance was found over a broad mid-IR spectrum between $\lambda = 2.5$ to 8.0 μm. The strong absorption after $\lambda = 8.0$ μm is due to the combinations of fundamental vibration modes existing at longer wavelengths, such as the Ti-O stretching and bending vibrations. [106,107] The results showed that the sputtered TiO_2 thin film is a suitable material for mid-IR photonic circuits.

The structure of TiO_2-on-LN device was inspected by an SEM equipped with EDS. Figure 4.4 shows the cross-sectional SEM image of a 10 μm wide and 0.8 μm height TiO_2 ridge waveguide sitting on an LN substrate. Two Ti electrodes were loaded on each side of the waveguide. The device has a well-defined ridge structure without cracks or indents on the surface. The sharp

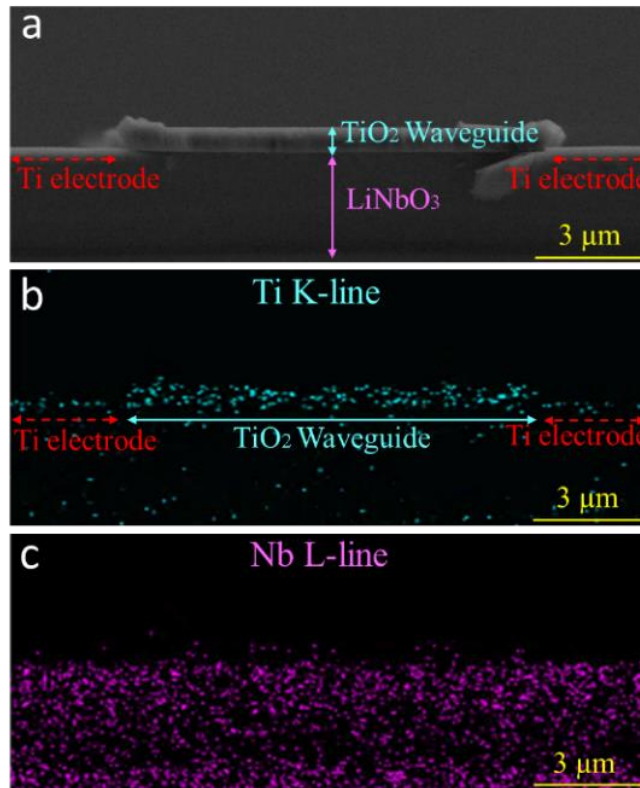

Figure 4.4. The cross-sectional view of the ToL waveguide from (a) SEM and EDX from (b) Ti K and (c) Nb L emission lines, indicating the TiO_2 ridge, Ti electrodes, and the LN substrate, respectively. The TiO_2 ridge is 0.8 µm thick and 10 µm wide. The waveguide surface and the interface between the TiO_2 and LN was smooth. Ti electrodes were found next to the waveguide.

---

waveguide edges reduced the waveguide propagation loss caused by light scattering. In addition, the interface between the TiO_2 waveguide and the LN layer was well-resolved. No depletion damage was found on the device surfaces or the interface because the waveguide was prepared by a lift-off process instead of an aggressive etching process. EDS with element mapping function was utilized to characterize the device layout and the material composition. As shown in Figure 4.4b, the Ti profile identified the TiO_2 ridge waveguide in the TiO_2-on-LN center and two thin Ti electrodes loaded next to the waveguide. In Figure 4.4c, the Nb distribution corresponded to the LN substrate that was underneath the TiO_2 waveguide and Ti electrodes. The well-defined

waveguide configuration and the high material uniformity avoided the optical loss caused by the variation of refractive indexes.

4.2.2 Optical Property Simulation

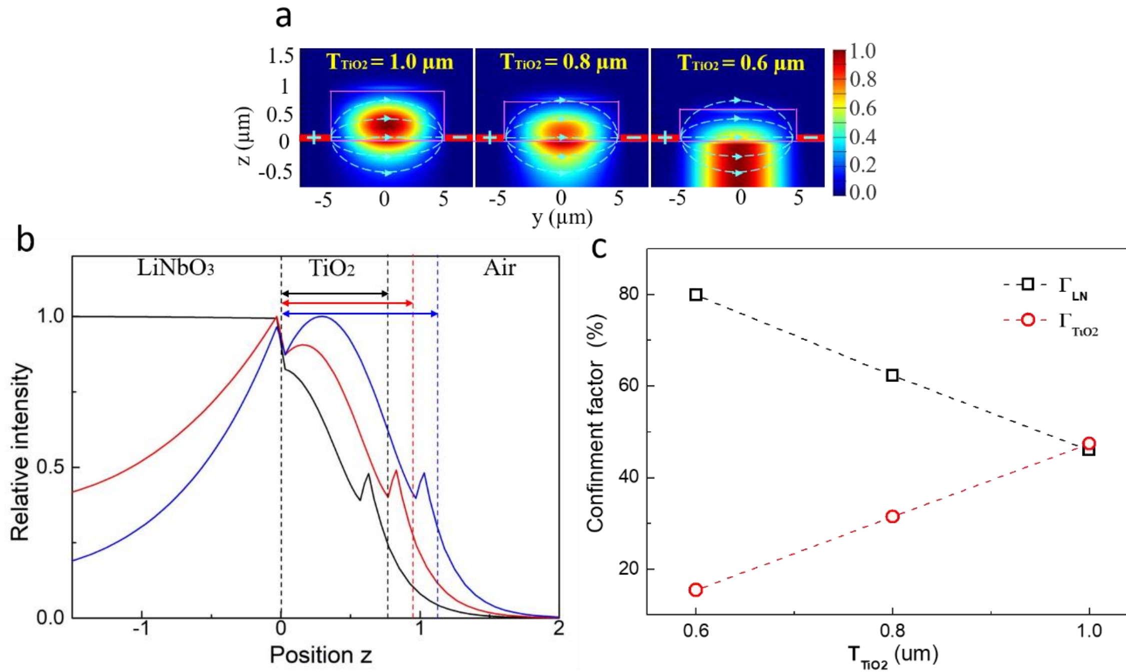

Figure 4.5 (a) The calculated optical field when the thickness of the TiO_2 layer decreases from 1.0 μm to 0.6 μm. The center of the waveguide mode was shifted from the TiO_2 layer to the LN layer. At $\mathbf{T_{TiO2}}$ = 0.8 μm, a hybrid waveguide mode was formed where the light was evenly confined in the TiO_2 and the LN layers. (b) The calculated 1-D intensity profiles along the z direction at y = 0 μm, where the blue, red, and black curves indicate $\mathbf{T_{TiO2}}$ = 1.0, 0.8, and 0.6 μm, respectively. (c) The calculated optical field confinement factors, Γ_{LN} and Γ_{TiO2}, at different T_{TiO2}. Γ_{LN} increased and Γ_{TiO2} dropped as the TiO_2 thickness increased.

The waveguide mode was numerically simulated by the two-dimensional FDM. In the modeling, a 12 μm × 6 μm TM light source was chosen to excite a mode at λ = 2.5 μm since its dimension is close to the 9 μm core mid-IR fiber used in the experiment. The refractive indexes, **n**, of TiO_2 and LN are 2.39 and 2.18, respectively. [108,109] The mode profile and field intensity confined in the TiO_2 and LN layers were modified by adjusting the TiO_2 thickness, $\mathbf{T_{TiO2}}$. As

shown in Figure 4.5a at $\mathbf{T_{TiO2}}$ = 1 μm, a fundamental mode was clearly observed within the TiO_2 ridge while a strong evanescent field appeared in the LN cladding layer, which was a characteristic profile belonging to the TM polarization mode. [110] As $\mathbf{T_{TiO2}}$ decreased to 0.8 μm, the mode center shifted toward the LN layer. A hybrid mode with a strong field existing in both LN and TiO_2 layers was revealed. A TiO_2-on-LN waveguide with this configuration is capable of efficient electro-optical modulation since the optical field was confined in the ferroelectric LN layer and its overlapping with the electric field significantly increased. At $\mathbf{T_{TiO2}}$ = 0.6 μm, most light was localized in the LN layer because the TiO_2 ridge was too thin to support a waveguide mode alone. To better visualize the variation of the optical field when $\mathbf{T_{TiO2}}$ changed, Figure 4.5b shows the calculated 1-D intensity profiles parallel to the z-direction at y = 0 μm. At $\mathbf{T_{TiO2}}$ = 1 μm, the intensity peak appeared in the center of the TiO_2 layer. Meanwhile, the evanescent field in the lower LN cladding was much stronger than in upper air cladding since the LN has a higher refractive index than air. At $\mathbf{T_{TiO2}}$ = 0.80 μm, a hybrid mode was formed and the optical field in the ferroelectric LN layer became stronger, which was critical to achieving low $\mathbf{V_{\pi} \cdot L}$ electro-optical modulation. When $\mathbf{T_{TiO2}}$ = 0.60 μm, light was mostly localized in the LN layer indicating that a large modulation depth and a high signal to noise ratio can be obtained in this device configuration. The confinement factors, $\mathbf{\Gamma_{LN}}$ and $\mathbf{\Gamma_{TiO2}}$, were defined as the percentages of optical fields localized within the LN and the TiO_2 layers, respectively. As shown in Table 4.1 and Figure 4.5c, $\mathbf{\Gamma_{LN}}$ increased rapidly from 46.0 % to 80.0 % while $\mathbf{\Gamma_{TiO2}}$ decreased from 47.4 % to 15.5 %, as $\mathbf{T_{TiO2}}$ decreased from 1.0 to 0.60 μm. Therefore, optimization of $\mathbf{T_{TiO2}}$ reshaped the intensity distribution of the waveguide mode, leading to a stronger optical field confined within the LN layer. Consequently, this enhanced the interaction between the mid-IR light wave and the electrical field that created high electro-optical reconfigurability and reduced optical propagation loss.

Table 4.1 The TiO_2-on-LN waveguide confinement factors, $\mathbf{\Gamma_{LN}}$, $\mathbf{\Gamma_{TiO2}}$, and $\mathbf{\Gamma_{Air}}$, at different thickness $\mathbf{T_{TiO2}}$. $\mathbf{\Gamma_{LN}}$ increased from 46.0 to 80.0 as $\mathbf{T_{TiO2}}$ decreased from 1.0 to 0.6 µm indicating an improvement of electro-optical modulation efficient.

$\mathbf{T_{TiO2}}$ (µm)	$\mathbf{\Gamma_{LN}}$ (%)	$\mathbf{\Gamma_{TiO2}}$ (%)	$\mathbf{\Gamma_{Air}}$ (%)
0.6	80.0	15.5	4.5
0.8	62.3	31.5	6.2
1.0	46.0	47.4	6.6

4.2.3 Electro-Optical Effect Characterization

For electro-optical analysis, let's consider the LN crystal orientation first. Since LN is an optically anisotropic material, its ordinary ($\mathbf{n_o}$) and extraordinary index ($\mathbf{n_e}$) with respect to the crystal axes can be described through the index ellipsoid (without E-field) as

$$\frac{x^2}{n_o^2}+\frac{y^2}{n_o^2}+\frac{z^2}{n_e^2}=1 \qquad (4.1)$$

With its Pockels tensor:

$$\begin{pmatrix} 0 & -\gamma_{22} & \gamma_{13} \\ 0 & \gamma_{22} & \gamma_{13} \\ 0 & 0 & \gamma_{33} \\ 0 & \gamma_{51} & 0 \\ \gamma_{51} & 0 & 0 \\ -\gamma_{22} & 0 & 0 \end{pmatrix} \qquad (4.2)$$

, the effect of applying an electric field is described by the associated deformation of the index ellipsoid derived as:

$$\left(\frac{1}{n_o^2}+\gamma_{13}E_z-\gamma_{22}E_y\right)x^2+\left(\frac{1}{n_o^2}+\gamma_{22}E_y+\gamma_{13}E_z\right)y^2+\left(\frac{1}{n_e^2}+\gamma_{33}E_z\right)z^2-2\gamma_{22}E_xxy+2\gamma_{51}E_xxz+2\gamma_{51}E_yyz=1 \qquad (4.3)$$

The reported electro-optical coefficient $\boldsymbol{\gamma_{13}}$, $\boldsymbol{\gamma_{33}}$, $\boldsymbol{\gamma_{22}}$ and $\boldsymbol{\gamma_{51}}$ can be as large as 9.6 pm/V, 30.9 pm/V, 6.8 pm/V and 32.6 pm/V for lithium niobate crystal, respectively. The electric field along z direction can get involved with large $\boldsymbol{\gamma_{33}}$ with the light propagation along y direction. Therefore,

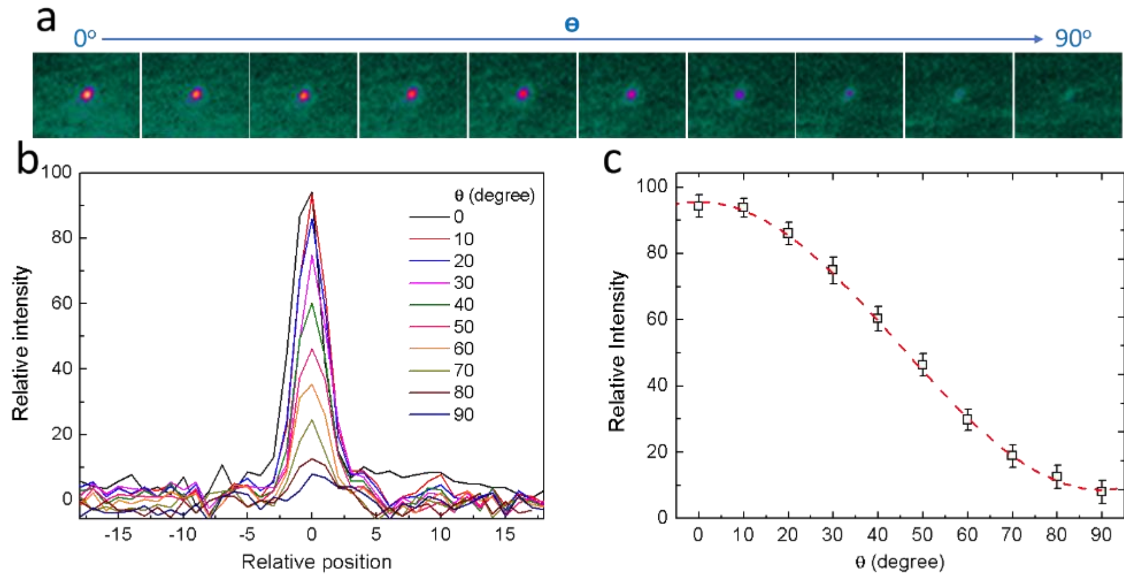

Figure 4.6 (a) The optical waveguide mode captured by a MIR camera when the polarizer rotated at different angle **θ**. The wavelength was set at λ = 2.5 μm. The mode decreased as **θ** changed from 0° to 90°. (b) The 1D intensity distribution of the waveguide mode recorded at various **θ**. A Gaussian mode profile was found. (c) The plot of the mode relative intensity vs the polarization angle **θ**. The red dash line is the fitting result using a cosine square function.

a x-cut LN was selected as the substrate, and an external voltage **V** was applied on the pair electrodes. The polarizer was fixed at **θ** = 45° so the initial intensity was half of its maximum found at **θ** = 0°. The electric field **E** across the waveguide was adjusted between 0 to 7.5 V/μm by tuning the voltage **V** of the power supply. The transient mode intensity **I** was recorded and drawn in Figure 5a. The intensity raised sharply whenever an electrical field was applied. Figure 4.6b displayed the **I** - **V** curve extrapolated from Figure 4.7a and the fitting curve derived from the Pockels effect. The experimentally observed linear electro-optical response can be described by an equation as

$$I(V) = I_0[1 - \cos\left(\varphi_0 - \pi\frac{V}{V_\pi}\right)] \quad (4.4)$$

The parameter $\mathbf{V_\pi \cdot L}$ = 50 V·cm was found for the ToL waveguide. Through the equation

$$V_\pi = \frac{g \cdot \lambda}{2 \cdot \gamma_{eff} \cdot n_e^3 \cdot L \cdot \Gamma_{LN}} \quad (4.5)$$

the γ_{eff} was derived as 5.9 pm/V. The resolved γ_{eff} was slightly lower than the γ_{31} of 8.6 pm/V because the waveguide and the electrical field were not strictly parallel to the optical axis of the LN substrate. An even lower $\mathbf{V_\pi \cdot L}$ of 7 V·cm can be achieved if the electrode gap **g** is narrowed to 3 μm and the waveguide is aligned to the LN y-axis.

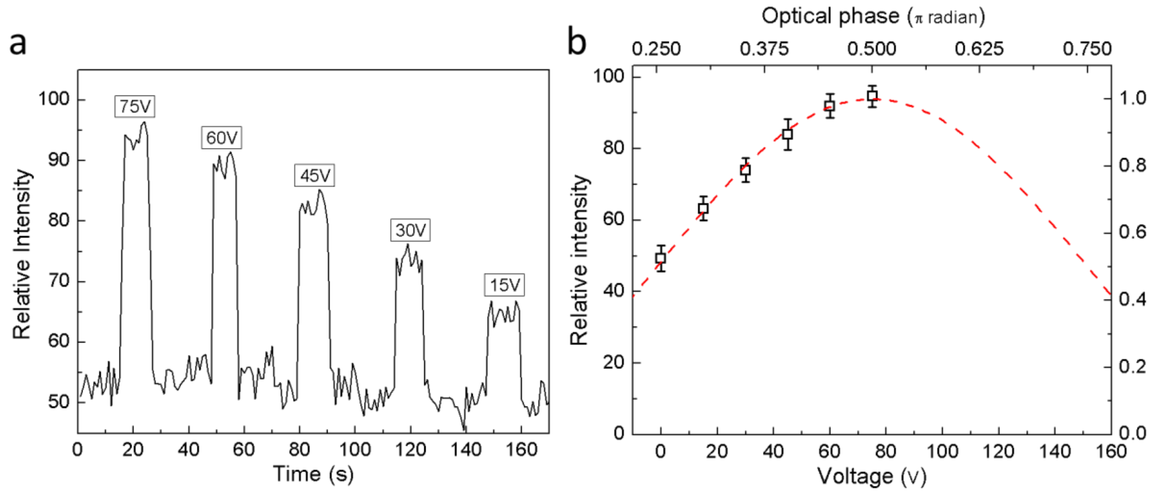

Figure 4.7 (a) The transient mode intensity when pulses of the electrical field were applied to the electrodes using a power supply at various voltage **V**. (b) The **I - V** plot extrapolated from transient response. The fitting result shows a cosine square function.

4.3 Top-bonded Barium Titanate Polarization Modulator

A new device platform consisting of TiO_2 waveguides that were bonded with an electro-optical tunable BTO crystal. Both TiO_2 and BTO have a broad mid-IR transparency up to λ = 6 μm. According to the device geometry, the light can be effectively guided by the TiO_2 waveguide since it has a relatively high refractive index of $\mathbf{n_{TiO2}}$ = 2.41 compared to that of the BTO crystal, ~~of~~ $\mathbf{n_{BTO}}$ =2.32. In parallel, efficient modulation can be carried out because the evanescent field extended into the BTO layer. Our approach not only avoided the difficulties in utilizing the LN thin films that required complex preparation but also solve the BTO crystal phase transition issue

caused by high-temperature process (>120 ^{0}C) during the fabrication. Moreover, BTO has a much stronger Pockels effect and broader mid-IR transparent window than LN, rendering BTO capable of reaching high modulation speeds beyond 40 GHz in the long wavelength region. The hybrid TiO_2 - BTO device provided a platform possessing a high electro-optical reconfigurability that operates over a wide spectrum range.

4.3.1 Device Fabrication and Materials Characterization

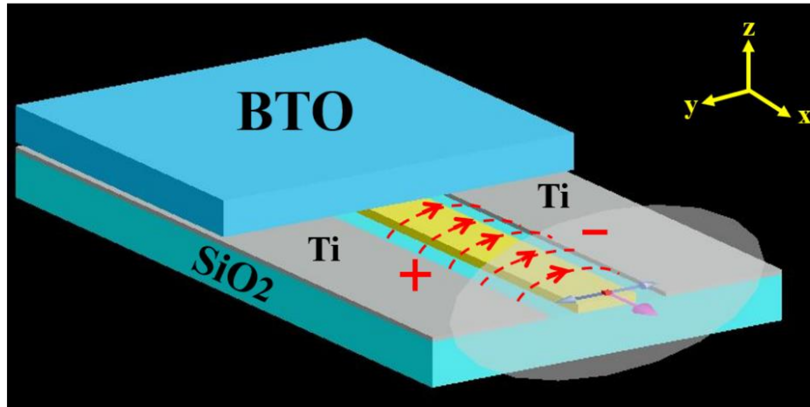

Figure 4.8 (a) Schematic structure of the TiO_2-on-SiO_2 waveguide bonded with BTO crystal. TiO_2 waveguide is sitting on SiO2 substrate with Ti pair electrodes on two sides.

The schematic of the device structure is illustrated in Figure 4.8. The whole device is fabricated on a 4- inch Si wafer with a 5 μm layer of thermal oxide. First, a 600 nm TiO_2 film was grown on the wafer by reactive RF sputtering. During the deposition process, a 99.999% pure Ti target was utilized, and a combination of Ar and O_2 was introduced into the sputtering chamber. The working pressure and RF power were 3 mTorr and 500 W, respectively, which resulted in a deposition rate of 200 nm/hr. After the TiO_2 film was grown, a Cr etching mask was sequentially fabricated by lithography and lift-off process and defines the ridge waveguide area. Then, reactive ion etching was employed to structure the TiO_2 waveguide. In this work, an SF_6 and Ar mixture (6:1) was

utilized for etching, and all of the TiO_2 films without Cr protection was removed completely. After being cleaned by the Cr etchant and O_2 ashing, the TiO_2 ridge waveguides were obtained. Following the waveguide fabrication, a 350 nm Ti pair of electrodes were aligned on both sides of the waveguides ~~also~~ by lithography and lift-off process. A piece of the <100> BTO crystal was placed on top of the waveguide to perform electro-optical modulation. A pressing force was then applied to the BTO crystal by a manipulator to ensure it is attached to the waveguide surface.

The morphology of the fabricated device was inspected by microscope and scanning electron microscopy (SEM). As shown in Figure 4.9a, the TiO_2 waveguide with the pair of Ti electrodes was fabricated on top of the Si/SiO_2 wafer. The device was defined by two areas: the coupling area and the modulation area. In the coupling area displayed in the Figure 4.9a inset, the waveguide width was 25 μm to increase the butt-coupling efficiency at long wavelengths. The pair of electrodes were spaced 200 μm apart. However, in the modulation area, the waveguide width was only 8 μm, and the gap between the electrodes decreased to approximately 25 μm (shown in Figure 4.9b). The BTO crystal was placed onto the modulation area, and the waveguides were aligned with the <001> direction of BTO to approach the maximum electro-optical coefficient. Through the top view of the device, the fabricated waveguide had a well-defined ridge structure without any distortion, and there were no cracks or indents on both the TiO_2 and under-cladding surfaces. Thus, no depletion damage was introduced to the device during the fabrication process, which is essential to minimize the scattering loss of the propagation mode. Figure 4.9c displays the cross-sectional view of the waveguide. The facet is smooth without cracking and damaging, which improves the butt-coupling efficiency. In addition, the interface between the top TiO_2 guiding layer and the under-cladding layer is clear and well-defined. The inset on Figure 4.9b displays the material composition of the waveguide structure, which is characterized by energy-dispersive X-

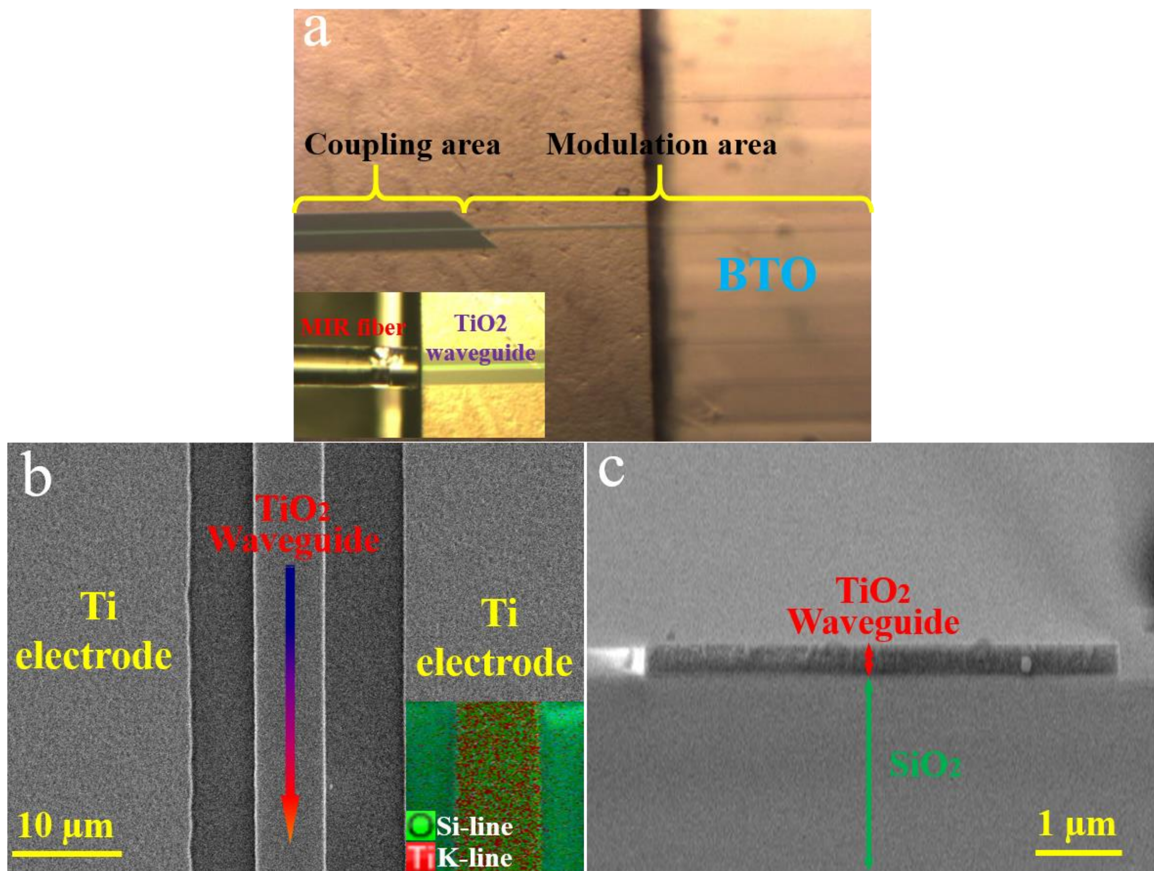

Figure 4.9 (a) The top view of the fabricated device captured by an optical microscope. The coupling area consists of a 25 μm wide waveguide, which increases the efficiency of butt-coupling, as shown in the inset. The SEM images were captured from the (b) top and (c) cross-section of the waveguide. The inset in (b) illustrates the material composition of the waveguide. The Si and Ti profiles revealed the areas belonging to the SiO_2 under-cladding and the TiO_2 waveguide.

---

ray spectroscopy (EDX) at the Si Kα (1.74 keV) and Ti Kα (4.47 keV) emission lines. The elemental spatial distributions of Si and Ti demonstrate that the device profiles belong~~ing~~ to the SiO_2 under-cladding area and the TiO_2 wave-guiding area. From the mapping results, it's confirmed that the deposited TiO_2 thin films have homogeneous compositions across the film surfaces. The high uniformity of the material distribution obtained is able to prevent the optical scattering loss caused by variations in ~~of~~ refractive indexes.

4.3.2 Optical Property Simulation

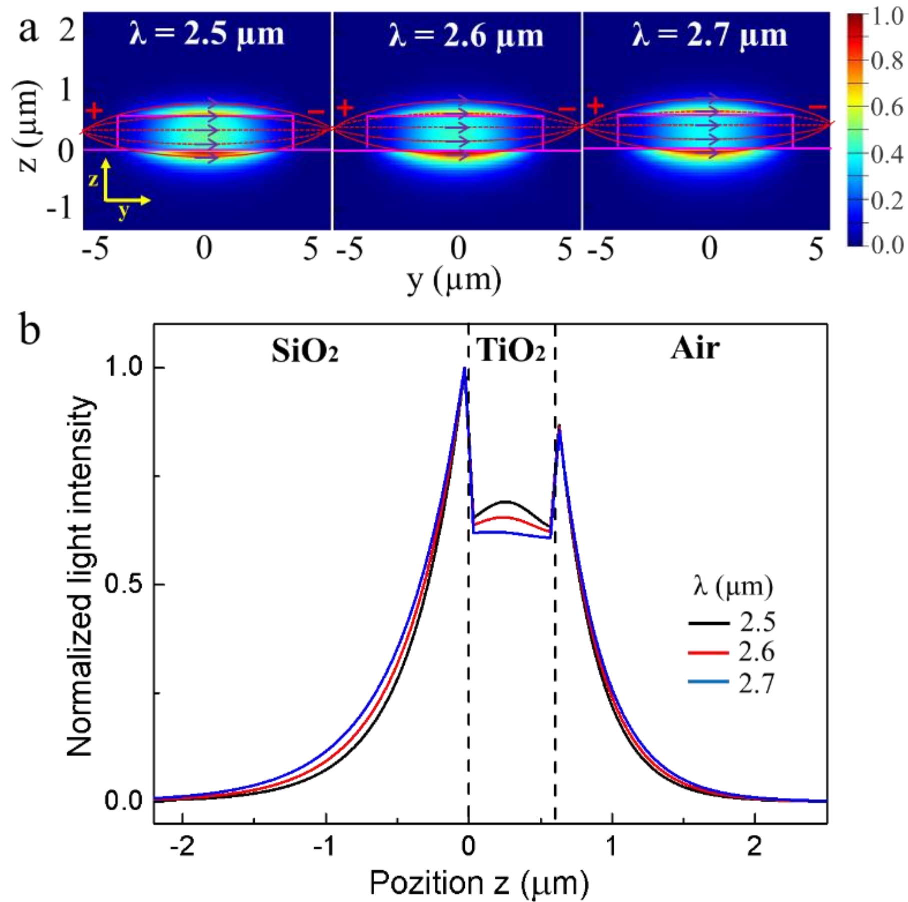

Figure 4.10 (a) The optical fields of the TiO_2-on-SiO_2 waveguides calculated at λ = 2.5, 2.6, and 2.7 μm. The fundamental modes with similar ellipsoid intensity distributions were resolved in the Si layer in all three wavelengths. (b) The corresponding 1D intensity profiles along the z-axis at y = 0. A strong evanescent field exists on the top and bottom surface of TiO_2.

Firstly, the optical property of the fabricated waveguide was theoretically calculated by the finite difference method (FDM). In the simulation, a 10 μm × 10 μm light source was chosen to excite the waveguide mode since its size is comparable to the mid-IR fiber used in the experiment. The light wave was irradiated from the coupling end of a TiO_2 waveguide. The waveguide structure was set up based on the SEM inspection viewed in Figure 4.9, which was a 0.6 μm high and an 8 μm wide TiO_2 waveguide sitting on top of a SiO_2 substrate. The refractive indices $\mathbf{n_{TiO2}}$ and $\mathbf{n_{SiO2}}$

are 2.39 and 1.45, respectively. The calculated intensity profiles corresponding to the TM waveguide modes at λ = 2.5 μm, 2.6 μm, and 2.7 μm are illustrated in Figure 4.10a. Fundamental modes with similar ellipsoid intensity distributions are clearly resolved in the TiO_2 layer over λ = 2.5 to 2.7 μm. In parallel, strong evanescent fields are found on both the top ($z > 0.6$ μm) and bottom surfaces of the TiO_2 layer ($z < 0$ μm), which were caused by the intrinsic propagation property of the TM mode. As the mode was tuned to longer wavelengths, the light intensity confined to the TiO_2 layer gradually faded. To better analyze this effect, the light intensity profiles along the z-axis ($y = 0$ μm) are calculated and plotted in Figure 4.10b. Most of the light field was confined near the TiO_2 area (0 μm < z < 0.6 μm), which demonstrates that the waveguide was able to effectively guide the light mode through the optical path. Along the z-direction, the optical field expanded extensively outside the TiO_2 layer, and the evanescent fields had notable increases as the wavelength increased from λ = 2.5 to 2.7 μm. The thin TiO_2 layer contributed to the strong evanescent field intensity that existed on both the top and bottom edges of the waveguide. The strong evanescent field beyond the waveguide surface enables various applications, including electro-optical modulation. When the evanescent field was overlapped with a ferroelectric material with a high electro-optical response, such as BTO, the optical signals were efficiently modulated by the external electric field. The fraction of optical power within the penetration depth for the TM mode is calculated to be around $\boldsymbol{\Gamma_{TM}}$ = 24.7%, which will partly overlap with bonded BTO crystal. It should be noticed that the bonded BTO crystal can be hardly attached well with the TiO_2 surface for the real bonding case. The touching issue is essentially caused by *i.* The contaminating particles dropped on the fabricated device; *ii.* The tiny top surface of the fabricated ridge waveguide; *iii.* The minimal variation of the guiding layer thickness. It's inevitable that the touching issue will lead the actual confinement factor $\boldsymbol{\Gamma_{TM}}$ much smaller than the calculated value 24.7%.

4.3.3 Electro-Optical Effect Characterization

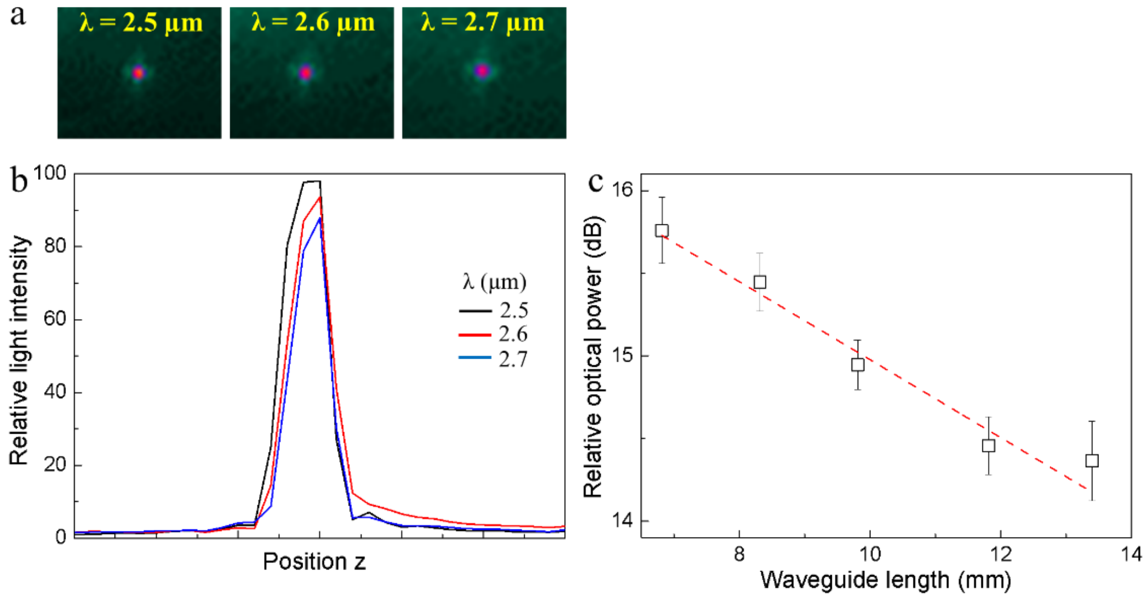

Figure 4.11 The waveguide mode images captured from λ = 2.5 to λ = 3.7 µm, where the fundamental mode is clearly observed. (b) A Gaussian profile corresponding to a fundamental mode was found over λ = 2.5 µm to 2.7 µm. (c) The relative optical powers measured from the waveguides with different lengths. An optical loss of 2.3 dB/cm was obtained by fitting the mode intensity attenuation at λ = 2.6 µm.

The optical performance of the device was evaluated, and the results of the mode images and optical loss characterizations are shown in Figure 4.11. As shown in Figure 4.11a, a fundamental mode is clearly observed over a broad spectral range from λ = 2.5 µm to λ = 2.7 µm. The mode profiles remain similar at different wavelengths, while minor scattering was observed at longer wavelengths. No distortion was found in the captured mode images, which indicate that the waveguides had smooth surfaces and a smooth interface between the TiO_2 and SiO_2 layers. The high refractive indices of the TiO_2 layer also attributed to the efficient guiding of the mid-IR light. The intensity profiles of the waveguide modes were then extrapolated and illustrated in Figure 4.11b. A well-resolved Gaussian profile corresponding to a fundamental mode was found over the spectrum, and the result is consistent with the simulated mode profiles displayed in Figure 4.10b.

The optical loss was derived by fitting the mode intensity attenuation from waveguides with different lengths. As shown in Figure 4.11c, an optical loss of 2.33 dB/cm was obtained at $\lambda = 2.6$ µm, which is better than those reported in the visible and near-infrared ranges. The low optical loss of the TiO_2-on-SiO_2 waveguide can be explained by the high mid-IR transparency of the deposited TiO_2 thin film, as well as by the smooth interface between the TiO_2 and SiO_2 layers. In addition, the scattering loss caused by surface roughness was significantly reduced at longer wavelengths since the Rayleigh scattering coefficient is proportional to $1/\lambda^4$.

For electro-optical analysis, let's consider the single-domain c-oriented BTO crystal, with its domain orientation (optical axis) along the z-axis. Since BTO is an optically anisotropic material, its ordinary ($\mathbf{n_o}$) and extraordinary index ($\mathbf{n_e}$) with respect to the crystal axes can be described through the index ellipsoid (without E-field) as

$$\frac{x^2}{n_o^2} + \frac{y^2}{n_o^2} + \frac{z^2}{n_e^2} = 1 \qquad (4.6)$$

With its Pockels tensor:

$$\begin{pmatrix} 0 & 0 & \gamma_{13} \\ 0 & 0 & \gamma_{23} \\ 0 & 0 & \gamma_{33} \\ 0 & \gamma_{51} & 0 \\ \gamma_{51} & 0 & 0 \\ 0 & 0 & 0 \end{pmatrix} \qquad (4.7)$$

, the effect of applying an electric field is described by the associated deformation of the index ellipsoid derived as:

$$\left(\frac{1}{n_o^2} + \gamma_{13}E_z\right)x^2 + \left(\frac{1}{n_o^2} + \gamma_{13}E_z\right)y^2 + \left(\frac{1}{n_e^2} + \gamma_{33}E_z\right)z^2 + 2\gamma_{51}E_x xz + 2\gamma_{51}E_y yz = 1 \qquad (4,8)$$

In this work, utilizing the <001> BTO crystal means the z-axis is perpendicular to the horizontal plane. When applying electric field along x axis, the index ellipsoid will rotate along y axis. The induced ellipsoid rotation angle is a function of the applied electric field E, and the optical axes

rotation will affect the propagation mode polarization. Such polarization change was monitored by the mid-IR camera with a polarizer.

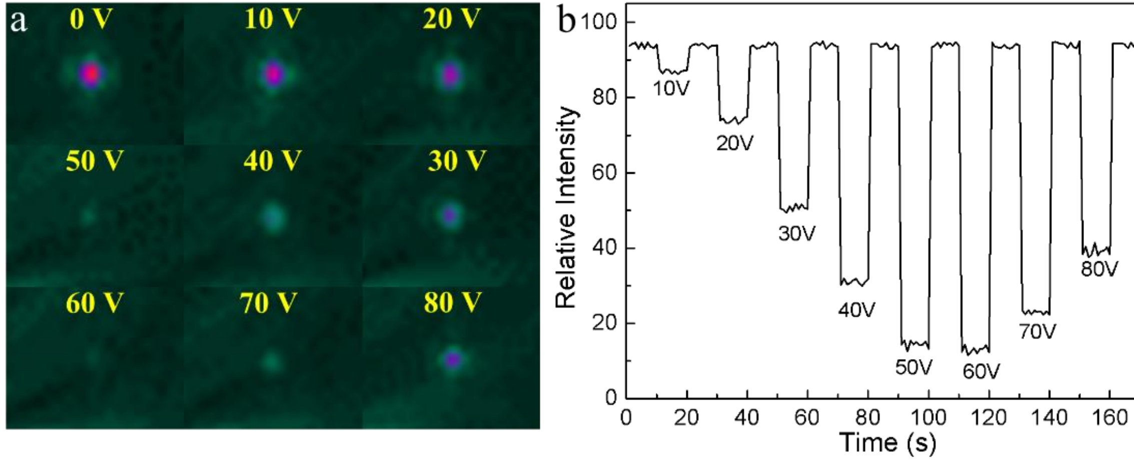

Figure 4.12 (a) The optical waveguide modes captured by a mid-IR camera when various drive voltages were applied. The wavelength was at $\lambda = 2.6$ µm. (b) The mode intensity when several pulses of the electric field were applied to the electrodes using a power supply at voltage **V**.

The light mode variation was then monitored by a mid-IR camera. The polarizer axis was initially rotated to $\theta = 0^{o}$, where θ is the angle between the axis of the polarizer and the polarization of the light come out of waveguide end, so that the maximum intensity was collected. A train of drive pulses were applied to the electrodes. In parallel, the waveguide mode images corresponding to various **V** were recorded and are shown in Figure 4.12a. Additionally, the corresponding transient intensity response is plotted in Figure 4.12b. When no **V** was applied, the mode was bright and sharp since the mode polarization was parallel to the polarizer axis. When the drive voltage applied, there is phase retardation generated between two wave components perpendicular to the propagation direction, which change the polarization of the propagating wave. As the drive voltage increased, the phase retardation becomes larger, and changes the wave polarization from linear parallel to the polarizer axis to ellipsoid polarized. Thus, the waveguide mode kept fading

until the entire mode almost disappeared at **V**≈50 V, indicating that the generated phase retardation is increased to π/2 and the polarization became perpendicular to the polarizer axis. As the **V** continued to increase, the phase retardation kept increasing and the light intensity started to recover. To better visualize this electro-optical effect, Figure 4.13a plots the 1-D mode intensity profile **I** under different drive voltages **V**. The intensity profiles exhibit similar Gaussian distributions at various **V**, and a large modulation depth of 9.7 dB was derived by comparing the highest and

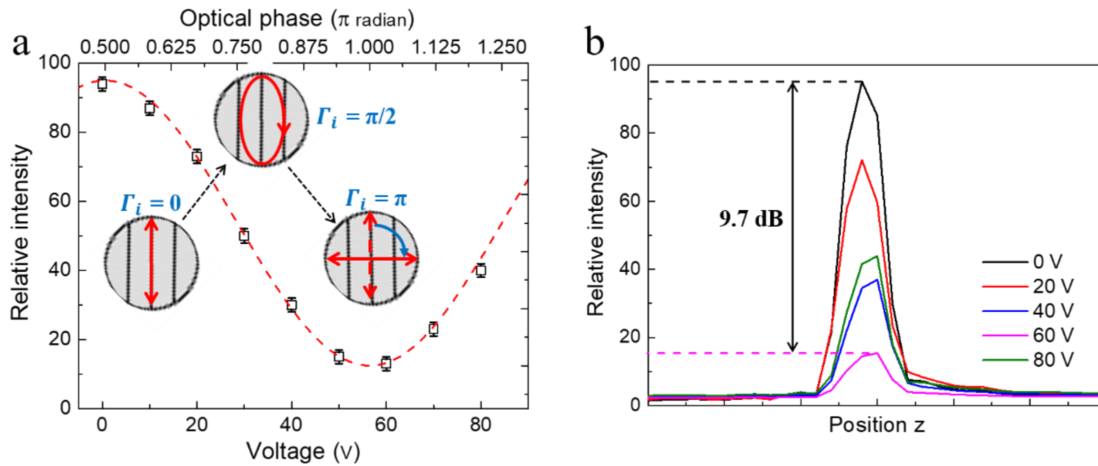

Figure 4.13 (a) The 1D intensity distribution of the waveguide mode recorded at various voltage. A modulation depth of 9.7 dB was found. (b) The plot of the mode intensity vs the applied voltage. The red dash line is the fitting result using a cosine square function.

---

lowest intensity levels. Figure 4.13b displays the **I - V** plot extrapolated from Figure 4.12b and the fitting curve derived from the Pockels effect. The experimentally observed linear electro-optical response can be described by

$$\mathrm{I}(V) = I_0 cos^2(\pi \frac{V}{2V_\pi} + \varphi_0) \qquad (4.9)$$

where $\boldsymbol{\varphi_0}$ is the initial phase, which was determined by the initial angle of the polarizer axis, and $\mathbf{V_\pi}$ is the half-wave voltage that introduced a phase shift of π. The measured electro-optical response implied a small voltage-length product $\mathbf{V_\pi \cdot L}$ = 11 V·cm through the following equation:

$$\gamma_{eff} = \frac{g \cdot \lambda}{V_\pi \cdot n_e^3 \cdot L \cdot \Gamma_{TM}} \qquad (4.10)$$

The effective electro-optical coefficient γ_{eff} of 154 pm/V was obtained.

4.4 Silicon Nitride on Barium Titanate Polarization Modulator

In this work, epitaxial BTO thin film is monolithically integrated with a ultra-thin silicon nitride (SiN) waveguide to perform phase modulation in the mid-IR region for the first time. Comparing to conventional amorphous Si waveguides, SiN has a much smaller refractive index as $n_{SiN} = 1.96$, which is even smaller than the index of BTO $n_{BTO} = 2.35$. Thus, the majority of the propagation mode is trapped into BTO layer enabling a large modulation depth. The propagation mode was observed through 2.5 - 2.7 μm, and the propagation loss was experimentally measured as 3.4 dB at 2.6 μm. The electro-optical modulation effect was characterized by recording the propagation mode intensity when applying drive voltage. A small voltage-length product, $V_\pi \cdot L$, of 6.6 V·cm was obtained at $\lambda = 2.6$ μm, and the modulation depth can be reached at 10 dB. The developed SiN-on-BTO platform enables reconfigurable mid-IR photonic circuits desired for high-performance photonic and active mid-IR applications.

4.4.1 Device Fabrication and Materials Characterization

The detailed fabrication process is shown in Figure 4.14. First, 0.5 μm BTO thin film was grown on MgO substrate by pulse laser deposition. Then, a layer of 0.1 μm SiN was deposited on the BTO film by plasma enhanced CVD. After photography, a photoresist mask was patterned on the SiN layer, and the waveguide ridge structure was defined by reactive ion etching. Au electrodes that are 300 nm high were fabricated on both sides of the waveguide by lithography and lift-off process. The pair of electrodes were spaced 12 μm apart.

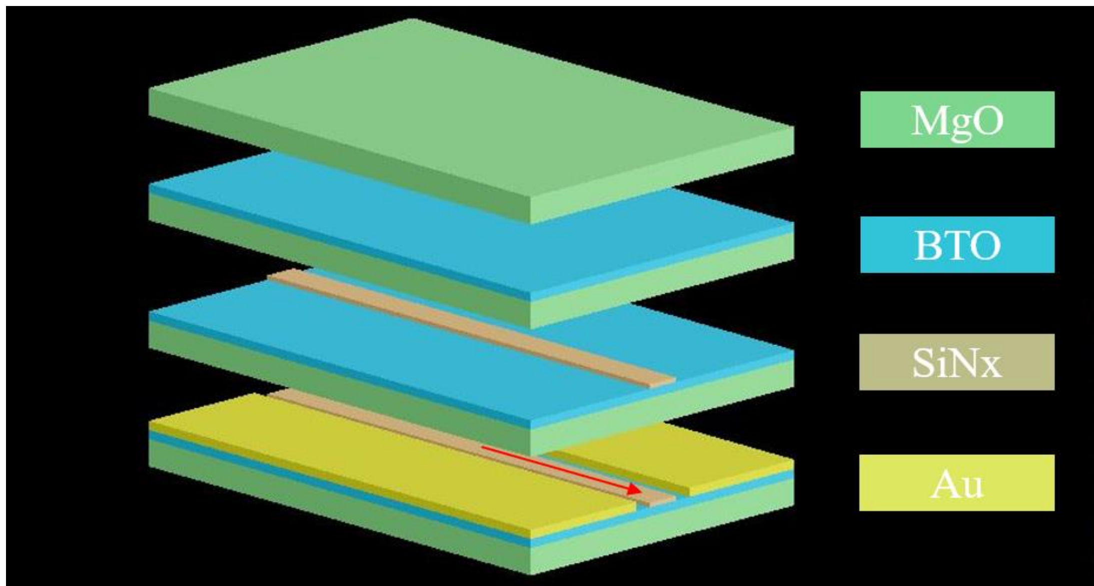

Figure 4.14 Schematic of the SiN-on-BTO waveguide fabrication process. The BTO film was deposited on the MgO substrate first. Then the SiN waveguide was defined on it by photolithography PECVD, lithography, and RIE. At last, Au electrodes were fabricated on both sides of SiN waveguide.

The morphology of the fabricated device is inspected by microscope and scanning electron microscopy (SEM). Figure 4.15a shows the top view of the fabricated device. SiN waveguides with and without the pair of electrodes localized on both sides are placed on BTO/MgO substrate. The waveguide with no electrodes is for optical measurement, and the one with electrodes is for electro-optical property measurement. The waveguides are aligned with <100> of BTO to approach the maximum electro-optical coefficient. The electrodes have the same length as the waveguides, and their width is ~ 100 μm. Figure 4.15b shows the magnified SEM image of the critical area. A 4 μm wide SiN waveguide sits on the BTO layer. Two Au electrodes were placed on both sides of the waveguide, and the spacing between the pair of electrodes was around 12 μm. The image contrast of Au is much higher than SiN area since the Au is 3 times thicker than the SiN layer. The fabricated waveguide has a well-defined ridge structure without any distortion, and there is no cracks or indents on both SiN and BTO surface. Thus, no depletion damage was

introduced during the fabrication process, which is essential to minimize the optical loss of the device.

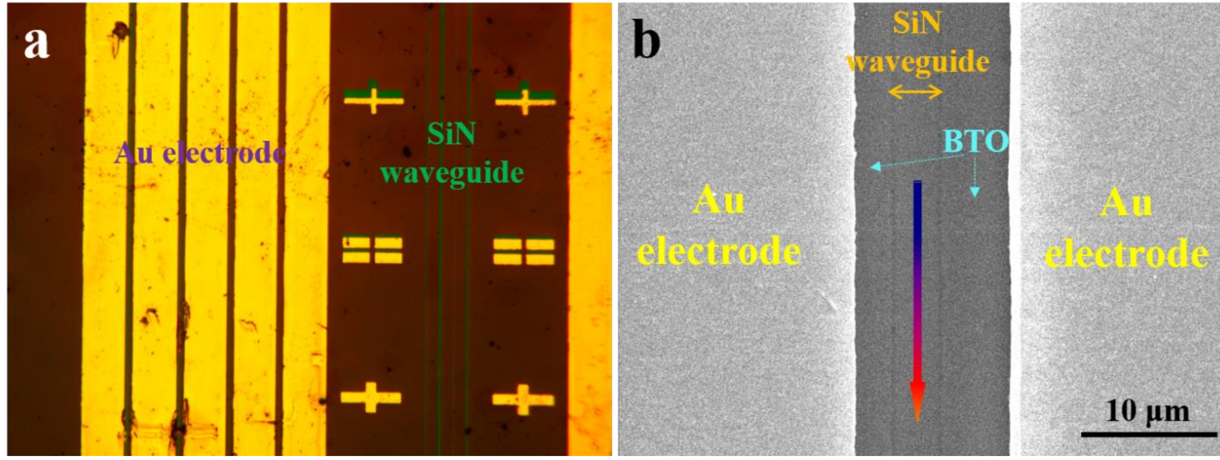

Figure 4.15 Top view of the fabricated device captured by (a) microscope and (b) SEM. The SiN waveguide is 4 µm and the spacing between pair electrodes is 12 µm.

4.4.2 Optical Property Simulation

The optical property of the fabricated waveguide was theoretically calculated by the finite difference method (FEM) at first. Figure 4.16a illustrates the device configuration and refractive index profile applied in the modeling, which is built based on the dimension viewed in Figure 4.15. The SiN waveguide is 0.1 µm high and 4 µm wide, sitting on 1 µm BTO film and MgO substrate. The refractive index $\mathbf{n_{SiN}}$, $\mathbf{n_{BTO}}$, and $\mathbf{n_{MgO}}$, are 1.96, 2.35, and 1.70, respectively. A 12 µm × 8 µm light source is chosen to excite the waveguide mode since its size is comparable to the mid-IR fiber in the measurements, which has a core diameter of 9 µm. The calculated intensity profiles corresponding to the TM waveguide modes at $\lambda = 2.5$ µm, 2.6 µm, and 2.7 µm are depicted in Fig. 3b. Fundamental modes with similar ellipsoid intensity distribution are clearly resolved in the BTO layer over $\lambda = 2.5$ µm to $\lambda = 2.7$ µm, where the light wave can be easily manipulated by overlapped electric field. Strong evanescent fields exist on both top ($z > -0.5$) and the bottom surface of the

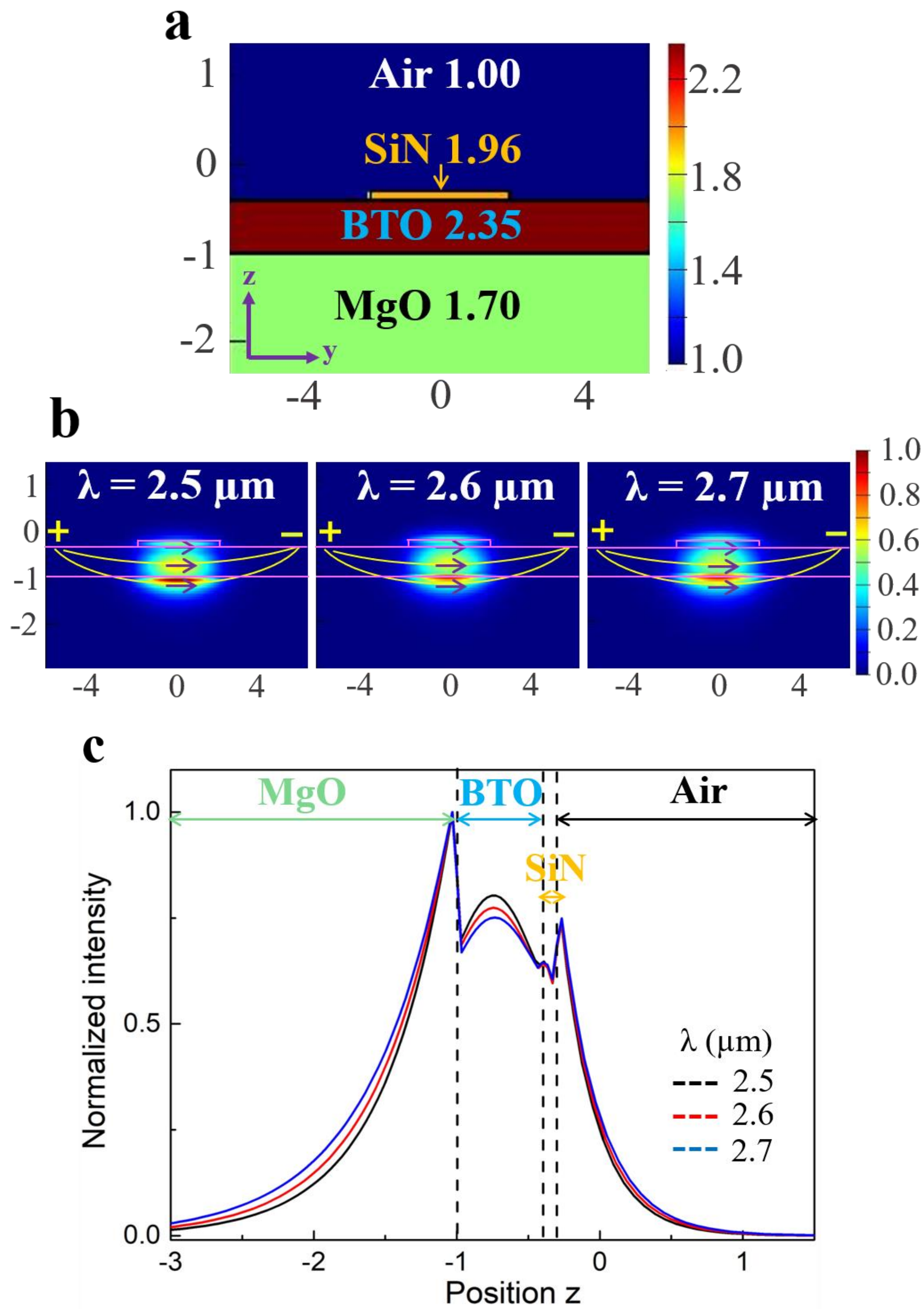

Figure 4.16 (a) The device configuration and the refractive index profile applied in the FEM modeling. The refractive indexes, $\mathbf{n_{SiN}}$, $\mathbf{n_{BTO}}$, and $\mathbf{n_{MgO}}$, are 1.96, 2.35, and 1.70, respectively. (b) The optical fields of the SiN-on-BTO waveguides calculated at λ = 2.5 μm, 2.6 μm, and 2.7 μm. Fundamental modes with similar ellipsoid intensity distributions are resolved in the Si layer in all three wavelengths. (c) 1D intensity profiles along the z axis at y=0.

BTO layer (z < -1), which results from intrinsic propagation property of TM modes. It should be

noticed that the evanescent field on top partly expands outside SiN area, since the SiN layer is too thin (0.1 μm) to hold all light field confined inside it. On one hand, such ultra-thin guiding structure is able to guide the light mode through the optical path effectively. On the other hand, the strong evanescent field extended in the air enables the fabricated device capable of applications as mid-IR sensing. To better visualization the intensity distribution, Figure 4.16c depicts one dimensional TM polarized intensity profiles along the z-axis at y=0. Most light intensity is confined inside the BTO area ($-1<z<1$) because BTO has the highest index $\mathbf{n_{BTO}} = 2.35$ in this structure. Thus, the modulation effect due to the BTO electro-optical property becomes clear because of the overlap between the light and the electric field. The evanescent field in the MgO layer is more intensive than on the SiN/air side, due to the effective refractive index of MgO being larger. As the probe light shifts to a longer wavelength, the light intensity slightly expands from the center of the BTO area into the MgO and SiN/air layers. However, the mode profiles generally remain stable across the scanning spectrum. The fraction optical power overlap with BTO layer for TM mode is calculated as around $\boldsymbol{\Gamma_{TM}} = 26.6\%$.

4.4.3 Electro-Optical Effect Characterization

The optical performance of the SiN-on-BTO waveguide is evaluated by the structured testing station, and the captured mode images are shown in Figure 4.17. From Figure 4.17a, a fundamental mode is clearly observed over the range from $\lambda = 2.5$ μm to $\lambda = 2.7$ μm as expected, and the mode profiles remain the same at different wavelengths. No scattering and distortion is found in the captured mode images, indicating the fabricated waveguides have flat facet and smooth interfaces between different layers. The intensity profiles of the waveguide modes are then extrapolated and illustrated in Figure 4.17b. A well resolved Gaussian profile corresponding to a fundamental mode

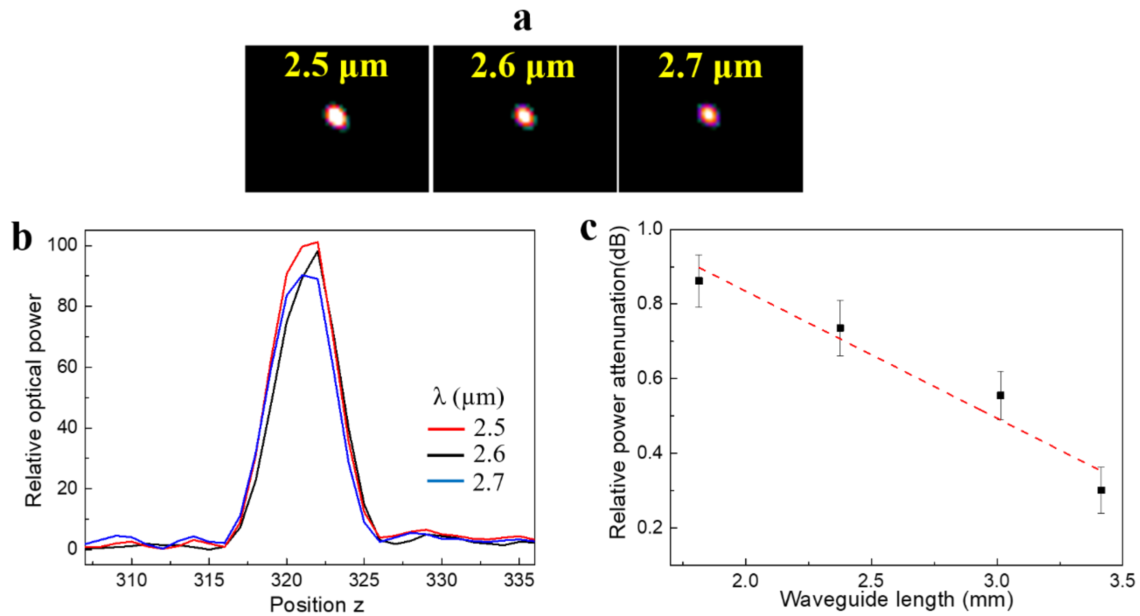

Figure 4.17 (a) The waveguide mode images captured at λ = 2.5 µm to λ = 2.7 µm, where fundamental mode is clearly observed. (b) A Gaussian profile corresponding to a fundamental mode is found over λ = 2.5 µm to 2.7 µm. (c) Relative optical powers measured from the waveguides with different lengths. An optical loss of 3.4 dB/cm is obtained by fitting the mode intensity attenuation at λ = 2.6 µm

---

is found over λ = 2.5 µm to 2.7 µm, which is consistent with the simulation results displayed in Figure 4.16. In addition, the unchanged shape of the mode over such spectrum demonstrates low-frequency dispersion of the device. Such preservation of a sharp fundamental mode in the mid-IR region is essential to achieve high accuracy electro-optical modulation tests. An excitation of higher order modes with strong scattering will alter the mode profile and lead to false intensity variation when modulated by the electric field. The optical loss of the waveguide was obtained by measuring optical powers from waveguides of different lengths. By fitting the mode intensity attenuation in Figure 4.17c, an optical loss of 3.4 dB/cm is obtained at λ = 2.6 µm, which attributes to the high mid-IR transparency of the deposited epitaxial BTO thin film, as well as to the smooth surfaces of the device.

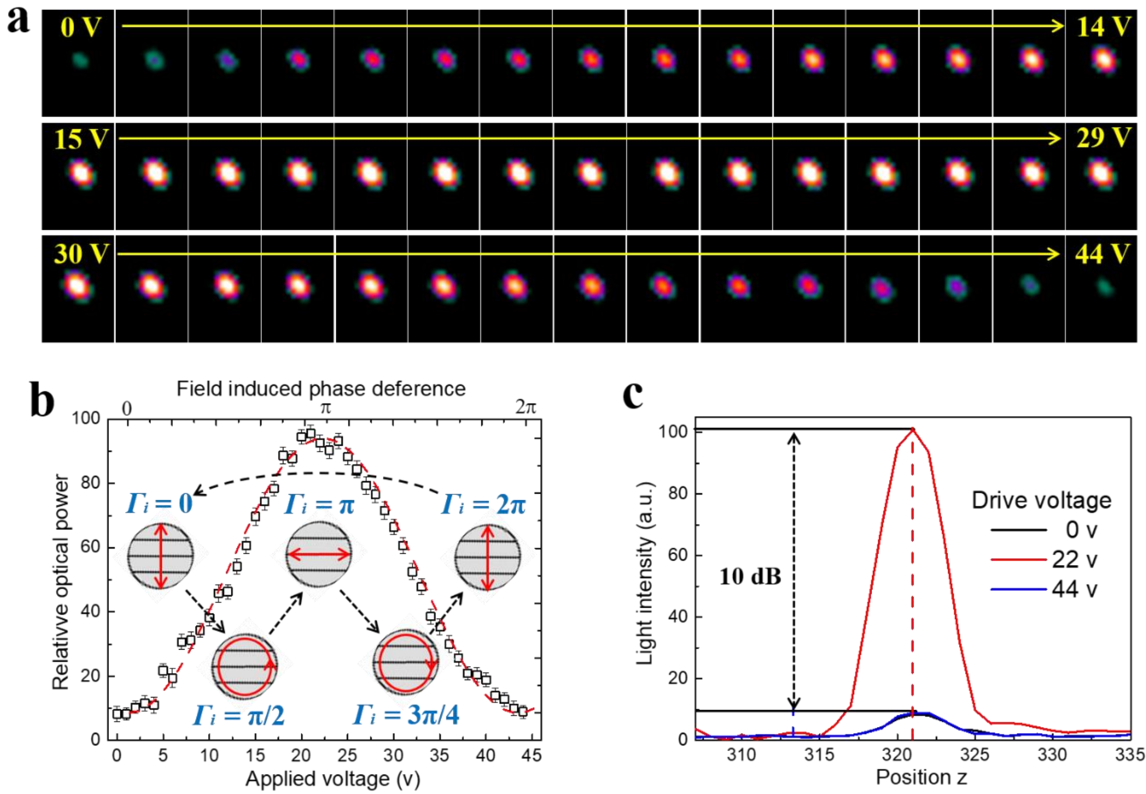

Figure 4.18 (a) The optical waveguide mode captured by a mid-IR camera when drive voltage was applied. The wavelength was set at λ = 2.6 μm. (b) The plot of the mode intensity vs the applied voltage. The red dash line is the fitting result using a cosine square function. (c) The 1D intensity distribution of the waveguide mode recorded at various voltage. A modulation depth of 8.3dB was found.

The electro-optical analysis was performed by measuring the mode intensity variation of a 1.5 mm long device. The light modes were directly captured by the mid-IR camera when external drive voltage was applied to the device. As shown in Figure 4.18a, the polarizer axis was firstly set perpendicular to the polarization of propagation mode with no voltage applied, so that the captured mode intensity is at its lowest level. As the drive voltage increased, the light mode becomes sharper and brighter without any distortion or scattering. When the drive voltage is between 20 ~ 25 v, the mode brightness reaches its peak value indicating the mode polarization is now aligned with the polarizer axis. Thus, a π/2 phase shift of propagation mode occurred as the

drive voltage increase to ~22V. When the drive voltage continues increasing to 44 V, the mode polarization is flipped over by π. As a result, the mode light faded back to its lowest level again. To better visualize such electro-optical effect, Figure 4.18b plots the mode intensity **I** versus the drive voltage **V**. By fitting the curve, the experimental electro-optical response can be described as

$$\mathrm{I}(V) = I_0 sin^2(\pi \frac{V}{2V_\pi} + \varphi_0) \qquad (4.11)$$

, where $\boldsymbol{\varphi_0}$ is initial phase determined by the angle of the polarizer axis. $\mathbf{V_\pi}$ = 22 V is the half-wave voltage that introduces a π phase shift. The measured modulation response also translates to a small voltage-length product, $\mathbf{V_\pi \cdot L}$ = 3.3 V·cm. Through the equation

$$V_\pi = \frac{g \cdot \lambda}{\gamma_{eff} \cdot n_e^3 \cdot L \cdot \Gamma_{TM}} \qquad (4.12)$$

, where the effective electro-optical coefficient $\boldsymbol{\gamma_{eff}}$ can be derived as 278 pm/V. To better analyze the change in mode intensity, Figure 4.18c plots one-dimensional mode intensity profiles under different drive voltages. All the mode profiles have similar Gaussian distribution. At 0V and 44V,

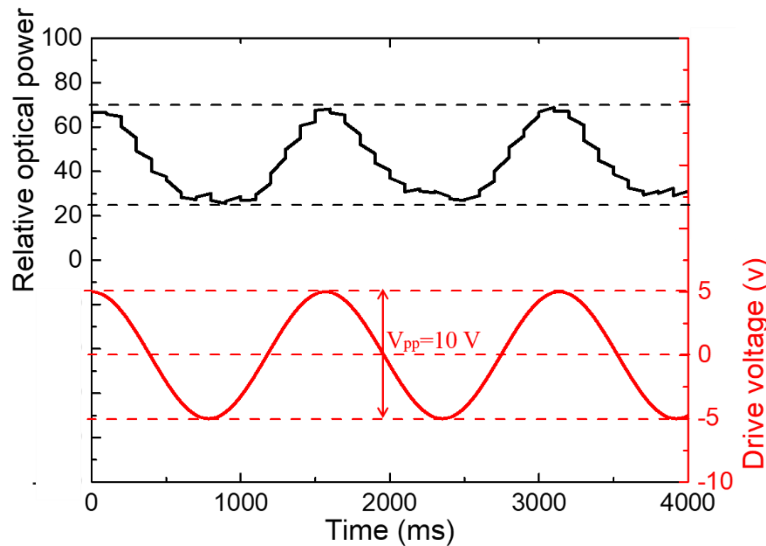

Figure 4.19 Real-time electro-optic modulation of SiN-on-BTO device. Lower curve shows voltage applied to the side electrodes, and upper curve shows detected light intensity.

the mode polarization is perpendicular to the polarizer axis, and the mode intensity is gloom and negligible. On the contrary, when the mode polarization is parallel to the polarizer axis, the intensity becomes distinct and strong. By comparing the change in intensities, a measured modulation depth of 10 dB is obtained. The real-time modulation effect is measured by applying a sinusoidal electrical drive signal with a peak-to-peak amplitude V_{pp} of 10 V at a frequency of f = 1 Hz. Then the output mode intensity was recorded by the mid-IR camera. The polarizer axis was fixed at $\theta = 45^{o}$ to the light mode polarization to obtain the maximum intensity changing slope. As shown in Figure 4.19, the AC drive voltage introduces an AC phase retardation of the light mode intensity in real-time, which firmly reflects the ferroelectric behavior of the deposited BTO thin film localized in the fabricated waveguide.

CHAPTER V

CONCLUSIONS

The central task of this thesis is to explore nonlinear materials, including AlN, LN, and BTO, applications in the mid-IR region. Several passive and active integrated optical components, including mid-IR sensors and polarization modulators, are designed, simulated, fabricated, and characterized. Specifically, AlN thin films were grown by reactive DC sputtering, and BTO thin film was grown by pulse laser deposition. Both of them exhibit wide mid-IR transparent window > 5μm through the FTIR characterization results. Devices were fabricated based on those deposited thin films and bulk crystals by CMOS process. Six integrated components are introduced including three passive mid-IR sensors: *i*) Si-on-BTO sensor, *ii*) Si-on-AlN sensor, *iii*) flexible AlN sensor, and three active polarization modulators: *i*) TiO_2-on-LN modulator, *ii*) Top-bonded BTO modulator, *iii*) SiN-on-BTO modulator.

Within the work of Si-on-BTO sensor, it consists of a 1.5 μm tall a-Si ridge structure on a 0.5 μm thick BTO film under-cladding layer which was grown on MgO substrate. The waveguides have an optical loss of 4.2 dB/cm and a fundamental mode clearly observed between λ = 2.5 μm and 3.5 μm. The low optical loss is attributed to the highly transparent BTO film, the smooth interface between a-Si and BTO layers, flat waveguide surfaces, and sharp side walls. Based on the FDTD modeling, the waveguide mode can be positioned in the ferroelectric BTO layer for efficient electro-optical modulation, or sited in the Si layer for label-free optical sensing by adjusting the a-Si thickness, which demonstrates the integrated Si-on-BTO platform provides a new platform for tunable mid-IR photonics and chip-scale chemical detection. To characterize its sensing performance, heptane and methanol were then utilized as analytes to exam the mid-IR

waveguide sensor. Upon spectral scanning the waveguide modes showed strong intensity attenuation at λ = 3.0 μm - 3.2 μm for heptane detection and λ = 2.8 μm - 2.9 μm for methanol detection. These correspond to the characteristic C-H and O-H absorption bands. In the real-time measurements, the Si-on-BTO waveguide sensor can achieve in-situ chemical detection within milliseconds. Thus, the Si-on-BTO mid-IR waveguide provides a unique COMS compatible platform for label-free and high-throughput chemical screening.

Within the work of Si-on-AlN sensor, the under-cladding layer was replaced by deposited AlN thin film, which was prepared by DC sputter at room temperature, and it exhibited high homogeneity and uniformity enabling the Si-on-AlN platform to avoid highly propagation loss in the mid-IR region. The waveguide structure was created by selective Si etching using RIE with SF_6 gas so it prevented the underneath AlN layer from ion damage. The fabricated mid-IR waveguides have an optical loss of 2.21 dB/cm and a fundamental mode clearly observed between λ = 2.5 μm and 3.0 μm. Heptane and methanol were also utilized to exam its sensing performance, and the Si-on-AlN sensor exhibited same sensing effect as Si-on-BTO sensor for both spectral scan test and real-time tests. In addition, this monolithic Si-on-AlN platform is also able to engineer the propagation mode distribution between Si and AlN layer for efficient electro-optical modulation and label-free optical sensing by adjusting the a-Si thickness. Therefore, the Si-on-AlN device provides another versatile COMS compatible platform for multiple mid-IR applications.

Within the work of flexible AlN sensor, AlN waveguide was integrated with an ultrathin borosilicate membrane to structure a mid-IR flexible platform. From IR-VASE characterization the room temperature deposited AlN film has broad infrared transparency and low optical dispersion up to λ = 9 μm. The bendable mid-IR waveguides consist of a 2 μm tall AlN ridge

structure and it firmly adheres to the flexible borosilicate template through the SEM and EDS inspection. A fundamental waveguide mode and low optical loss were observed between $\lambda = 2.5$ and 2.7 μm. The low optical loss is attributed to the highly transparent AlN, the smooth interface between AlN and borosilicate template, and the homogeneous AlN composition. Label-free chemical sensing and concentration analysis were achieved by scanning the waveguide mode over the characteristic infrared absorption regime. The AlN waveguide sensor was able to distinguish between methanol, ethanol, and water because of their distinct O-H absorption between $\lambda = 2.50$ and 2.65 μm. In addition, real-time chemical monitoring with sub-second response time was illustrated. Thus, the flexible AlN waveguides provide not only a platform suitable for flexible mid-IR micro-photonics, but also a mid-IR sensing platform that realizes chip-scale, label-free, and in-situ chemical monitoring.

Within the work of TiO_2-on-LN modulator, TiO_2 waveguide was fabricated on LN crystal wafer to structure a monolithically integrated TiO_2-on-LN platform. The device showed smooth waveguide sidewalls and a sharp TiO_2 - LN interface because the waveguide was formed through the lift-off process instead of aggressive etching. After adjusting the thickness of the TiO_2 layer, a hybrid waveguide mode with a large field confinement $\Gamma_{LN} = 80.0$ % can be achieved due to an optimized refractive index difference Δn of 0.21 between TiO_2 and LN. The electro-optical tunability of the TiO_2-on-LN waveguide was then realized by applying the Pockels effect from the LN substrate, where an effective electro-optical γ_{eff} of 5.9 pm/V, which is close to $\gamma_{31} = 8.9$ pm/V, was obtained at $\lambda = 2.5$ μm.

Within the work of top-bonded BTO modulator, integrated TiO_2-on-SiO_2 waveguide platform was studied including its design, fabrication, and optical properties, and the electro-optical modulation was exploited by a <001> BTO crystal bonded on it. Such top-bonded structure solves

the phase transition issue of BTO crystal caused by high temperature during the fabrication process. The fabricated TiO_2-on-SiO_2 waveguide showed strong transparency between 2.5 - 2.7 μm. A small optical loss of 2.33 dB/cm was measured at $\lambda = 2.6$ μm. The electro-optical tunability of the platform was realized by bonding a BTO crystal on top of the TiO_2 waveguide. The strong evanescent field on top surface was overlapped by the ferroelectric material of high electro-optical coefficient. A γ_{eff} of 154 pm/V was derived under drive voltage applied. The modulation depth was obtained as large as 9.7 dB.

Within the work of SiN-on-BTO modulator, a reconfigurable mid-IR photonic circuit was created using a monolithically integrated SiN-on-BTO platform. The epitaxial c-axis BTO thin film was prepared by pulse laser deposition, and the fabricated waveguide shows a small optical loss of 3.4 dB/cm at 2.6 μm. The electro-optical tunability of the SiN-on-BTO waveguide was realized by applying the Pockels effect to the BTO thin film, where an effective coefficient $\boldsymbol{\gamma_{eff}}$ of 278 pm/V was derived. The modulation depth can be reached as 10 dB, and a small $V_{\pi} \cdot L$ of 3.3V·cm was obtained at 2.6 μm. The promising results demonstrate the developed SiN-on-BTO platform enables reconfigurable mid-IR photonic circuits desired for high-performance photonic chips to be created for mid-IR applications.

The proposed devices reveal the possibility of chip-scale photonic circuits integrated with passive and active components to realize multiple mid-IR applications such as high-performance photonic modulation and high-throughput biochemical monitoring.

REFERENCES

[1] X. Fan and I. M. White. Optofluidic microsystems for chemical and biological analysis. *Nat. Photonics*, **2011**, 5, 591.

[2] A. Chandrasekaran and M. Packirisamy, Biomed. Integrated microfluidic biophotonic chip for laser induced fluorescence detection. *Microdevices*, **2010**, 12, 923.

[3] K. Reddy, Y. Guo, J. Liu, W. Lee, M. K. Khaing and X. Fan. Rapid, sensitive, and multiplexed on-chip optical sensors for micro-gas Chromatography. *Lab Chip*, **2012**, 12, 901.

[4] P. T. Lin, S. W. Kwok, H. G. Lin, V. Singh, L. C. Kimerling, G. M. Whitesides, and A. Agarwal. Mid-Infrared Spectrometer Using Opto-Nanofluidic Slot-Waveguide for Label-Free On-Chip Chemical Sensing. *Nano Lett*, **2014**, 14, 231–238.

[5] P. T. Lin, J. Giammarco, N. Borodinov, M. Savchak, V. Singh, L. C. Kimerling, D. T. H. Tan, K. A. Richardson, I. Luzinov, and A. Agarwal. Label-Free Water Sensors Using Hybrid Polymer–Dielectric Mid-Infrared Optical Waveguides. *ACS Appl. Mater. Interfaces*, **2015**, 7, 11189–11194.

[6] T. Hu, B. Dong, X. Luo, Liow, Song, T. -Y. J. C. Lee, G. -Q. Lo. Silicon photonic platforms for mid-infrared applications. *Photonics Res.* **2017**, 5, 417-430.

[7] S. Wartewig, R. H. H. Neubert. Pharmaceutical applications of Mid-IR and Raman spectroscopy. *Adv. Drug Deliv. Rev.* **2005**, 57, 1144-1170.

[8] Shepherd, K. D.; Walsh, M. G. Infrared Spectroscopy—Enabling an Evidence-Based Diagnostic Surveillance Approach to Agricultural and Environmental Management in Developing Countries. *J. Near Infrared Spectrosc*. **2007**, 15, 1-9.

[9] R. Matini, R. Paiella, C. Gumachl, F. Capasso, E. A. Whittaker, H. C. Liu, H. Y. Hwang, D.L. Sivco, J. N. Baillargeon and A. Y. Cho. High-speed digital data transmission using mid-infrared quantum cascade lasers. *Electron. Lett*, **2001**, 37, 1290-1292.

[10] R. Shankar, M. Lončar. Silicon photonic devices for mid-infrared applications. *J Nanophotonics*, **2014**, 3, 329-341.

[11] P. T. Lin, V. Singh, Y. Cai, L. C. Kimerling, and A. Agarwal. Air-clad silicon pedestal structures for broadband mid-infrared microphotonics. *Opt. Lett*. **2013**, 38, 1031-1033.

[12] P. T. Lin, V. Singh, J. Hu, K. Richardson, J. D. Musgraves, I. Luzinov, J. Hensley, L. C. Kimerling and A. Agarwal. Chip-scale Mid-Infrared chemical sensors using air-clad pedestal

silicon waveguides. *Lab Chip*, **2013**,13, 2161-2166.

[13] T. Baehr-Jones, A. Spott, R. Ilic, A. Spott, B. Penkov, W.Asher, and M. Hochberg. Silicon-on-sapphire integrated waveguides for the mid-infrared. *Opt. Express*. **2010**, 18, 12127.

[14] F. Li, S. D. Jackson, C. Grillet, E. Magi, D. Hudson, S. J.Madden, Y. Moghe, C. O'Brien, A. Read, S. G. Duvall,P. Atanackovic, B. J. Eggleton, and D. J. Moss. Demonstration of electrooptic modulation at 2165 nm using a silicon Mach-Zehnder interferometer. *Opt. Express*. **2011**, 19, 15212.

[15] R. Soref, Mid-infrared photonics in silicon and germanium. *Nat. Photonics.* **2010**, 4, 495–497.

[16] J. S. Penadés, A. Z. Khokhar, M. Nedeljkovic and G. Z. Mashanovich, Low-Loss Mid-Infrared SOI Slot Waveguides. *IEEE Photonics Technol. Lett.* **2015**, 27, 1197-1199.

[17] P. T. Lin, H. G. Lin, Z. Han, T. Jin, R. Millender, L. C. Kimerling, A. Agarwal. Label-Free Glucose Sensing Using Chip-Scale Mid-Infrared Integrated Photonics. *Adv. Opt. Mater*. **2016**. 4, 1755-1759.

[18] P. T. Lin, V. Singh, L. Kimerling and A. M. Agarwal. Planar silicon nitride mid-infrared devices. *Appl. Phys. Lett*. **2013**, 102, 251121.

[19] P. T. Lin, Vivek Singh, Jianfei Wang, Hongtao Lin, Juejun Hu, Kathleen Richardson, J. David Musgraves, Igor Luzinov, Joel Hensley, Lionel C. Kimerling, and Anu Agarwal. Si-CMOS compatible materials and devices for mid-IR microphotonics. *Opt. Mate. Express*. **2013**, 3, 1474-1487.

[20] T. Jin, L. Li, B. Zhang, H.-Y. G. Lin, H. Wang and P. T. Lin, Monolithic Mid-Infrared Integrated Photonics Using Silicon-on-Epitaxial Barium Titanate Thin Films *ACS Appl. Mater. Interfaces*, **2017**, 9, 21848-21855.

[21] T. Jin, L. Li, B. Zhang, H.-Y. G. Lin, H. Wang, P. T. Lin, "Real-Time and Label-Free Chemical Sensor-on-a-chip using Monolithic Si-on-BaTiO3 Mid-Infrared waveguides," Sci. Rep. **2017**, 7, 5836.

[22] P. T. Lin, V. Singh, Y. Cai, L. C. Kimerling and A. Agarwal, Air-clad silicon pedestal structures for broadband mid-infrared microphotonics. *Opt. Lett.* **2013,** 38, 1031-1033.

[23] T. Kawanishi, T. Sakamoto and M. Izutsu, High-Speed Control of Lightwave Amplitude, Phase, and Frequency by Use of Electrooptic Effect. *IEEE J. Sel. Top. Quantum Electron*, **2007**, 13, 79-91.

[24] Xia, X.; Chen, Q.; Tsay, C.; Arnold, C. B.; Madsen, C. K. Low-loss chalcogenide waveguides on lithium niobate for the mid-infrared. *Opt. Lett* **2010**, 35, 3228-3230.

[25] Chiles, J.; Fathpour, S. Mid-infrared integrated waveguide modulators based on silicon-on-lithium-niobate photonics. *Optica* **2014**, 1, 350-355.

[26] Noguchi, K.; Mitomi, O.; Miyazawa, H. Millimeter-wave Ti: $LiNbO_3$ optical modulators. *J. Lightwave Technol.* **1998**, 16, 615–619.

[27] Chen, L.; Xu, Q.; Wood, M. G.; Reano, R. M. Hybrid silicon and lithium niobate electro-optical ring modulator. *Optica* **2014**, 1, 112-118.

[28] P. O. Weigel, M. Savanier, C. T. DeRose, A. T. Pomerene, A. L. Starbuck, A. L. Lentine, V. Stenger & S. Mookherjea, Lightwave circuits in lithium niobate through hybrid waveguides with silicon photonics, *Scientific Reports* **2016**, 6, 22301.

[29] P. Rabiei, J. Ma, S. Khan, J. Chiles, and S. Fathpour, Heterogeneous lithium niobate photonics on silicon substrates, *Opt Express* **2013**, 21, 25573-81.

[30] L. Chen, M. G. Wood MG, R. M. Reano, 12.5 pm/V hybrid silicon and lithium niobate optical microring resonator with integrated electrodes. *Opt Express*. **2013**, 21, 27003-10

[31] X. Hu, S. Cueff, P. R. Romeo, and R. Orobtchouk. Modeling the anisotropic electro-optic interaction in hybrid silicon-ferroelectric optical modulator. *Opt. Express*. **2015**, 23, 1699-1714

[32] C. Xiong, W. H. P. Pernice, J. H. Ngai, J. W. Reiner, D Kumah, F. J. Walker, C. H. Ahn, and H. X. Tang. Active Silicon Integrated Nanophotonics: Ferroelectric $BaTiO_3$ Devices. *Nano Lett.*, **2014**, 14, 1419–1425.

[33] Z. Liu, P.-T. Lin, B. W Wessels, F. Yi, S.-T. Ho, Nonlinear photonic crystal waveguide structures based on barium titanate thin films and their optical properties, *Appl. Phys. Lett.* **2007**, 90, 201104.

[34] J. Li, P. T. Lin, B. W. Wessels, Polarization reversal and backswitching dynamics in epitaxial BaTiO3 thin films, *J. Appl. Phys*, **2009**, 106, 054113.

[35] P. T. Lin, W. A. Russin, A. Joshi-Imre, L. E. Ocola, B. W. Wessels. Investigation of the optical response of photonic crystal nanocavities in ferroelectric oxide thin film. *J. Opt,* **2015**, 17, 105402.

[36] P. T. Lin, F. Yi, S. T. Ho, B. W. Wessels. Two-dimensional ferroelectric photonic crystal waveguides: simulation, fabrication, and optical characterization. *J. Lightw*, **2009**, 27, 4330.

[37] J. Li, P. T. Lin, B. W. Wessels. Polarization reversal and backswitching dynamics in epitaxial BaTiO3 thin films. *J. Appl. Phys*, **2009**, 106, 054113.

[38] P. T. Lin, B.W. Wessels, J.I. Jang, J. B. Ketterson. Highly efficient broadband second harmonic generation using polydomain epitaxial barium titanate thin film waveguides. *Appl. Phys. Lett*, **2008**, 92, 221103.

[39] Z. Liu, P. T. Lin, B. W. Wessels, F. Yi, S. T. Ho. Nonlinear photonic crystal waveguide structures based on barium titanate thin films and their optical properties. *Appl. Phys. Lett*, **2007**, 90, 201104.

[40] Lin, P. T.; Jung, H.; Limerling, L. C.; Agarwal, A.; Tang, H. X. Low-loss aluminium nitride thin film for mid-infrared microphotonics. *Laser & Photonics Reviews*, **2014**, 8, 23-28.

[41] Xiong, C.; Pernice, W. H. P.; Tang, H. X. Low-loss, silicon integrated, aluminium nitride photonics circuits and their use for electro-optic signal processing. *Nano letter*, **2012**, 12, 3562-3568.

[42] Larciprete, M. C.; Bosco, A.; Belardini, A.; Li Voti, R.; Leahu, G.; Sibilia, C.; Fazio, E.; Ostuni, R.; Bertolotti, M.; Passaseo, A.; Pot`ý, B.; Del Prete, Z. Blue second harmonic generation from aluminum nitride films deposited onto silicon by sputtering technique. *J. Appl. Phys*. **2006**, 100, 023507.

[43] H. Jung, H. X. Tang, Aluminum nitride as nonlinear optical material for on-chip frequency comb generation and frequency conversion, *Nanophotonics* **2016**, 5 (2):263–271

[44] Akiyama, M.; Morofuji, Y.; Kamohara, T.; Nishikubo, K.; Tsubai, M.; Fukuda, O.; Ueno, N. Flexible piezoelectric pressure sensors using oriented aluminum nitride thin films prepared on polyethylene terephthalate films. *J. Appl. Phys*. **2006**, 100, 114318.

[45] Microstructure and Thermal Stability of Aluminum Nitride Thin Films Deposited at Low Temperature on Silicon, K. K. Harris, B. P. Gila, J. Deroaches, K. N. Lee, J. D. MacKenzie, C. R. Abernathy, F. Ren, and S. J. Pearton, *J. Electrochem. Soc*. **2002**,149, G128-G130.

[46] Duquenne, C.; Djouadi, M. A.; Tessier, P. Y.; Jouan, P. Y.; Besland, M. P.; Brylinski, C.; Aubry, R.; Delage, S. Epitaxial growth of aluminum nitride on AlGaN by reactive sputtering at low temperature. *Appl. Phys. Lett*. **2008**, 93, 052905.

[47] Boger, R.; Fiederle, M.; Kirste, L.; Maier, M.; Wagner, J. Molecular beam epitaxy and doping of AlN at high growth temperatures. *J. Phys. D: Appl. Phys*. **2006**, 39, 4616.

[48] Benaissa, M.; Vennéguès, P.; Tottereau, O.; Nguyen, L.; Semond, F. Investigation of AlN films grown by molecular beam epitaxy on vicinal Si (111) as templates for GaN quantum dots. *Appl. Phys. Lett.* **2006**, 89, 231903.

[49] Belkerk, B. E.; Soussou, A.; Carette, M.; Djouadi, M. A.; Scudeller, Y. Structural-dependent thermal conductivity of aluminium nitride produced by reactive direct current magnetron sputtering. *Appl. Phys. Lett.* **2012**, 101, 151908.

[50] F. Khatkhatay, A. Chen, J. H. Lee, W. Zhang, H. Abdel-Raziq, and H. Wang, Ferroelectric properties of vertically aligned nanostructured $BaTiO_3$–CeO_2 thin films and their integration on silicon, *ACS Appl. Mater. Interfaces*, **2013**, 5, 12541–12547.

[51] L. Li, L. Sun, J. S. Gomez-Diaz, N. L. Hogan, P. Lu, F. Khatkhatay, W. Zhang, J. Jian, J. Huang, Q. Su, M. Fan, C. Jacob, J. Li, X. Zhang, Q. Jia, M. Sheldon, A. Alù, X. Li, and H. Wang, Self-assembled epitaxial au–oxide vertically aligned nanocomposites for nanoscale metamaterials, *Nano Lett*., **2016**, 16, 3936–3943

[52] C. Hilsum. Infrared Transmission of Barium Titanate, J. Opt. Soc. Am. **1955**, 45, 771-772

[53] J. T. Last. Infrared-Absorption Studies on Barium Titanate and Related Materials, *Phys. Rev.*, **1957**, 105, 1740

[54] R. Ruppin, Infrared Absorption and Ferroelectricity of Small $BaTiO_3$ Crystals, *phys. stat. sol. (b)*, **1974**, 64, 701

[55] D. K. Sparacin, R. Sun, A. M. Agarwal, M. A. Beals, J. Michel, and L. C. Kimerling, T. J. Conway, A. T. Pomerene, D. N. Carothers, and M. J. Grove, D.M. Gill, M. S. Rasras, S. S. Patel, and A. E. White. Low-Loss Amorphous Silicon Channel Waveguides for Integrated Photonics. 3rd IEEE International Conference on Group IV Photonics, **2006**, FD2, 255-257

[56] Y. Chen, H. Lin, J. Hu, and M. Li., Heterogeneously integrated silicon photonics for the mid-infrared and spectroscopic sensing. *ACS Nano*, **2014**, 8, 6955–6961

[57] F. Eltes, D. Caimi, F. Fallegger, M. Sousa, E. O'Connor, M. D. Rossell, B. Offrein, J. Fompeyrine, and S. Abel. Low-Loss BaTiO3–Si Waveguides for nonlinear integrated photonics. *ACS Photonics*, **2016**, 3, 1698–1703

[58] P. Castera, D. Tulli, A. M. Gutierrez, and P. Sanchis. Influence of BaTiO3 ferroelectric orientation for electro-optic modulation on silicon. Opt. Express. **2015**, 23, 15332-15342

[59] Lin, P. T.; Jung, H.; Limerling, L. C.; Agarwal, A.; Tang, H. X. Low-loss aluminium nitride thin film for mid-infrared microphotonics. *Laser Photon. Rev*, **2014**, 8, 23-28.

[60] Xiong, C.; Pernice, W. H. P.; Tang, H. X. Low-loss, silicon integrated, aluminium nitride photonics circuits and their use for electro-optic signal processing. *Nano lett*, **2012**, 12, 3562-3568.

[61] Jung, H.; Tang, H. X. Aluminum nitride as nonlinear optical material for on-chip frequency comb generation and frequency conversion, *Nanophotonics* **2016**; 5, 263-271

[62] Larciprete, M. C.; Bosco, A.; Belardini, A.; Li Voti, R.; Leahu, G.; Sibilia, C.; Fazio, E.; Ostuni, R.; Bertolotti, M.; Passaseo, A.; Pot`ý, B.; Del Prete, Z. Blue second harmonic generation from aluminum nitride films deposited onto silicon by sputtering technique. *J. Appl. Phys*. **2006**, 100, 023507.

[63] Akiyama, M.; Morofuji, Y.; Kamohara, T.; Nishikubo, K.; Tsubai, M.; Fukuda, O.; Ueno, N. Flexible piezoelectric pressure sensors using oriented aluminum nitride thin films prepared on polyethylene terephthalate films. *J. Appl. Phys*, **2006**, 100, 114318.

[64] Harris, K. K.; Gila, B. P.; Deroaches, J.; Lee, K. N.; MacKenzie, J. D.; Abernathy, C. R.; Ren, F.; Pearton, S. J. Microstructure and Thermal Stability of Aluminum Nitride Thin Films Deposited at Low Temperature on Silicon. *J. Electrochem. Soc*, **2002** 149, G128-G130.

[65] Duquenne, C.; Djouadi, M. A.; Tessier, P. Y.; Jouan, P. Y.; Besland, M. P.; Brylinski, C.; Aubry, R.; Delage, S. Epitaxial growth of aluminum nitride on AlGaN by reactive sputtering at low temperature. *Appl. Phys. Lett*. **2008**, 93, 052905.

[66] Boger, R.; Fiederle, M.; Kirste, L.; Maier, M.; Wagner, J. Molecular beam epitaxy and doping of AlN at high growth temperatures. *J. Phys. D: Appl. Phys*. **2006**, 39, 4616.

[67] Benaissa, M.; Vennéguès, P.; Tottereau, O.; Nguyen, L.; Semond, F. Investigation of AlN films grown by molecular beam epitaxy on vicinal Si(111) as templates for GaN quantum dots. *Appl. Phys. Lett.* **2006**, 89, 231903.

[68] Belkerk, B. E.; Soussou, A.; Carette, M.; Djouadi, M. A.; Scudeller, Y. Structural-dependent thermal conductivity of aluminium nitride produced by reactive direct current magnetron sputtering. *Appl. Phys. Lett.* **2012**, 101, 151908.

[69] T. Jin, H.-Y. G. Lin, P. T. Lin, "Monolithically Integrated Si-on-AlN Mid-infrared Photonic Chips for Real-Time and Label-Free Chemical Sensing," ACS Appl. Mater. Interfaces. **2017**, 9, 49, 42905-429112017, 9, 49, 42905-42911

[70] Jose, F.; Ramaseshan, R.; Dash, S.; Bera, S.; Tyagi, A. K.; Raj, B. Response of magnetron sputtered AlN films to controlled atmosphere annealing. *J. Phys. D: Appl. Phys.* **2010**, 43, 075304.

[71] Motamedi, P.; Cadien, K. XPS analysis of AlN thin films deposited by plasma enhanced atomiclayer deposition. *Applied Surface Science*, **2014**, 315, 104–109

[72] Nedeljkovic, M.; Khokhar, A. Z.; Hu, Y.; Chen, X.; Soler Penades, J.; Stankovic, S.; Chong, H. M. H.; Thomson, D. J.; Gardes, F. Y.; Reed, G. T.; Mashanovich, G. Z. Silicon photonic devices and platforms for the mid-infrared. *Opt Mater Express*. **2013**, 3, 1205-1214.

[73] Yu, Z.; Niu, X.; Liu, Z.; Pei, Q. Intrinsically stretchable poly-mer light-emitting devices using carbon nanotube-polymer composite electrodes. *Adv. Mater*, **2011**, 23, 3989-3994.

[74] Cherenack, K.; Koen, V. O.; Pieterson, L. V. Smart photonic textiles begin to weave their magic. *LFW*. **2012**, 48, 63-66.

[75] Swatowski, B.; Amb, C.; Breed, S.; Deshazer, D.; Weidner, W. K.; Dangel, R.; Meier, N.; Offrein, B. Flexible, stable, and easily pro-cessable optical silicones for low loss polymer waveguides. *Proc. SPIE*. **2013**, 8622, 8622-8624.

[76] Hu, J.; Li, L.; Lin, H.; Zhang, P.; Zhou, W.; Ma, Z. Flexible integrated photonics: where materials, mechanics and optics meet. *Opt Mater Express*. **2013**, 3, 1313-1331.

[77] Yoon, J.; Li, L.; Semichaevsky, A. V.; Ryu, J. H.; Johnson, H. T.; Nuzzo, R. G.; Rogers, J. A. Flexible concentrator photovoltaics based on microscale silicon solar cells embedded in luminescent waveguides. *Nat Commun*. **2011**, 2, 343.

[78] Chen, Y.; Li, H.; Li, M. Flexible and tunable silicon photonic circuits on plastic substrates. *Sci Rep*. **2012**, 2, 622.

[79] Yu, C. L.; Kim, H.; Leon, N.; Frank, I. W.; Robinson, J. T.; McCutcheon, M.; Liu, M.; Lukin, M. D.; Loncar, M.; Park, H. Stretcha-ble photonic crystal cavity with wide frequency tenability. *Nano Lett*. **2013**, 13, 248-252.

[80] Fan, L.; Varghese, L. T.; Xuan, Y.; Wang, J.; Niu, B.; Qi, M. Direct fabrication of silicon photonic devices on a flexible platform and its application for strain sensing. *Opt. Express*. **2012**, 20, 20564-20575.

[81] Ge, L.; Wang, X.; Chen, H.; Qiu, K.; Fu, S. Flexible subwave-length gratings fabricated by reversal soft UV nanoimprint. *Chin. Opt. Lett*. **2012**, 10, 090502-090505.

[82] Kim, D. H.; Lu, N.; Ma, R.; Kim, Y. S.; Kim, R. H.; Wang, S.; Wu, J.; Won, S. M.; Tao, H.; Islam, A.; Yu, K. J.; Kim, T. I.; Chowdhury, R.; Ying, M.; Xu, L.; Li, M.; Chung, H. J.; Keum, H.; McCormick, M.; Liu, P.; Zhang, Y. W.; Omenetto, F. G.; Huang, Y.; Coleman, T.; Rogers, J. A. Epidermal electronics. *Science*. **2011**, 333, 838-843.

[83] Ma. Z. Materials science: An electronic second skin. Science. **2011**, 333, 830-831.

[84] K. Müllen, U. Scherf. *John Wiley & Sons*, **2006**.

[85] A. Sugimoto, H. Ochi, S. Fujimura, A. Yoshida, T. Miyadera, M. Tsuchida. *IEEE Journal of Selected Topics in Quantum Electronics*, **2004**, 10, 107.

[86] G. Li, R. Zhu, Y. Yang. *Nat Photon*. **2012**, 6, 153.

[87] M. A. Meitl, Z. -T. Zhu, V. Kumar, K. J. Lee, X. Feng, Y. Y. Huang, I. Adesid, R. G. Nuzzo, J. A. Rogers. *Nat. Mater.* **2005**, 5, 33.

[88] V. Sukumaran, G. Kumar, K. Ramachandran, Y. Suzuki, K. Demir, Y. Sato, T. Seki, V. Sundaram, R. R. Tummala. *IEEE Trans. Compon. Packag. Manuf. Technol*. **2014**, 4, 786.

[89] M. K. Mazumder, J. W. Stark, C. Heiling, M. Liu, A. Bernard, M. N. Horenstein, S. Garner, H. Y. Lin. *MRS Adv.* **2016**, 1, 1003.

[90] V. Mortet, A. Vasin, P. -Y. Jouan, O. Elmazria, M. -A. Djouadi. *Surface and coatings technology.* **2003***,* 176, 88.

[91] J. H. Edgard. *Properties of Group III Nitrides. INSREC, London,* **1994**.

[92] J. G. Molleja, B. J. A. Gomez, E. Gautron, P. -Y. Jouan. *Eur. Phys. J. Appl. Phys*. **2013**, 64, 20302.

[93] A. Thedsakhulwong, K. Locharoenrat, W. Thowladda. *Adv Mat Res.***2013***,* 631, 186.

[94] E. L. Wooten, K. M. Kissa, A. Yi-Yan, E. J. Murphy, D. A. Lafaw, P. F. Hallemeier, D. Maack, D. V. Attanasio, D. J. Fritz, G. J. McBrien and D. E. Bossi, A Review of Lithium Niobate Modulators for Fiber-Optic Communications Systems. *IEEE J. Sel. Top. Quantum Electron,* **2000**, 6, 69-82.

[95] Y. Y. Lin, S. T. Lin, G. W. Chang, A. C. Chiang, Y. C. Huang and Y. H. Chen, Electro-optic periodically poled lithium niobate Bragg modulator as a laser Q-switch. *Opt. Lett* **2007**, 32, 545-547.

[96] D. S. Smith, H. D. Riccius and R. P. Edwin, Refractive indices of lithium niobite. *Opt. Commun*, **1976**, 17, 332-335.

[97] X. Xia, Q. Chen, C. Tsay, C. B. Arnold and C. K. Madsen, Low-loss chalcogenide waveguides on lithium niobate for the mid-infrared. *Opt. Lett* **2010**, 35, 3228-3230.

[98] J. Chiles and S. Fathpour, Mid-infrared integrated waveguide modulators based on silicon-on-lithium-niobate photonics. *Optica* **2014**, 1, 350-355.

[99] R. S. Weis and T. K. Gaylord, Lithium niobate: Summary of physical properties and crystal structure. *Appl. Phys. A*, **1985**, 37, 191-203.

[100] P. V. Lenzo, E. G. Spencer and K. Nassau, Electro-Optic Coefficients in Single-Domain Ferroelectric Lithium Niobate. *J. Opt. Soc. Am,* **1966**, 56, 633-635.

[101] K. Noguchi, O. Mitomi and H. Miyazawa, Millimeter-wave Ti: $LiNbO_3$ optical modulators. *J. Lightwave Technol.* **1998**, 16, 615–619.

[102] L. Chen, Q. Xu, M. G. Wood and R. M. Reano, Hybrid silicon and lithium niobate electro-optical ring modulator. *Optica* **2014**, 1, 112-118.

[103] A. Tronev, M. Parfenov, P. Agruzov, I. Ilichev, and A. Shamray, A. Performance Improvement of Lithium Niobate High Extinction Ratio Modulators by Means of Photorefractive Trimming. *ACPC*, Guangzhou, Guangdong China, Nov. **2017.**

[104] C. Wang, M. Zhang, B. Stern, M. Lipson and M. Lončar, Nanophotonic lithium niobate electro-optic modulators. *Opt. Express* **2018**, 26, 1547-1555.

[105] W. -H. Huang, C. -W. Lin and W. -S. Wang, Electrooptical Modulator Fabricated by Gallium Diffusion in Lithium Niobate. *IEEE Photonics Technol. Lett.* **2008**, 20, 1172 – 1174.

[106] J. T. Last, Infrared-Absorption Studies on Barium Titanate and Related Materials. *Phys. Rev.* **1957**, 105, 1740-1750.

[107] R. Ruppin, Infrared Absorption and Ferroelectricity of Small $BaTiO_3$ Crystals. *Phys. stat. solidi. (b)* **1974**, 64, 701-707.

[108] J. R. Devore, Refractive Indices of Rutile and Sphalerite. *J. Opt. Soc. Am.* **1951**, 41, 416-419.

[109] D. E. Zelmon, D. L. Small, and D. Jundt, Infrared corrected Sellmeier coefficients for congruently grown lithium niobate and 5 mol. % magnesium oxide–doped lithium niobite. *J. Opt. Soc. Am. B*, **1997**, 14, 3319-3322.

[110] O. Parriaux and G. J. Veldhuis, Normalized Analysis for the Sensitivity Optimization of Integrated Optical Evanescent-Wave Sensors *J. Light. Technol,* **1998**, 16, 573-582.